A fundamental approach to phase noise reduction in hybrid Si/III-V lasers
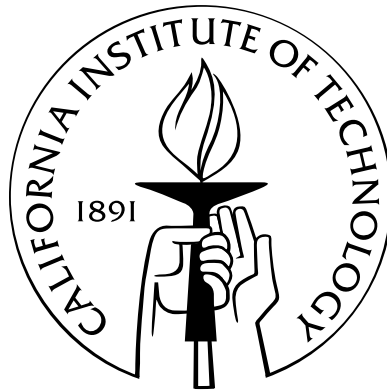
Thesis by

Scott Tiedeman Steger

In Partial Fulfillment of the Requirements

for the Degree of

Doctor of Philosophy

California Institute of Technology

Pasadena, California

2014

(Defended May 14, 2014)

Contents

Acknowledgements

Many people have helped me along the road to this thesis. I can't possibly name them all, but I am deeply grateful to all of them.

Prof. Yariv has been instrumental to my development as a scientist/engineer. I joined the group because of their exciting hybrid Si/III-V work, and his guidance has helped me to make my own small contribution to the field. I now hope to take what I've learned and apply it to different problems in optics and photonics.

My project was very complicated and never could have been completed without the integral help of several of my fellow students and postdocs. Christos Santis's early ideas for the high-Q hybrid laser and spacer implementation of modal engineering were, obviously, invaluable. I wish Christos the best of luck in the future, with high-coherence lasers and any other future endeavors. I must thank Yasha Vilenchik for tolerating my constant questions and for developing some of the fabrication processes I used. Our discussions were very important for working out the theory behind modal engineering. Xiankai Sun introduced me to semiconductor fabrication, teaching me many of the practical techniques that I used every day. Arseny Vasilyev made many of the low-noise circuits used to measure the lasers described here. Without his knowledge, the measurements wouldn't have been possible.

The other members of the Yariv Group have been equally important to my development over the years. I have learned a lot about related fields thanks to conversations with Naresh Satyan, Hsi-Chun Liu, Jacob Sendowski, Mark Harfouche, Dongwan Kim, Sinan Zhao, Marilena Dimotsantou, Paula Popescu, Reg Lee, and George Rakuljic. Connie Rodriguez also helped me navigate Caltech. Thank you all.

My friends outside the group and outside Caltech have kept me sane over the

years. I suppose I'm a little bit more normal today than I would have been without them. Thank you, John, Mark, Trevor, Mark, Judy, Idrees, Andrew, and Steve. Thank you to the champion Alberta Sunrise team and all of the chemistry students. All of you distracted me from my work just enough.

Last, I must of course thank my family. Their support for my interests from a very young age through today has been unwavering and I never would have gotten this far without them. A huge "thank you" to them.

Abstract

Spontaneous emission into the lasing mode fundamentally limits laser linewidths. Reducing cavity losses provides two benefits to linewidth: (1) fewer excited carriers are needed to reach threshold, resulting in less phase-corrupting spontaneous emission into the laser mode, and (2) more photons are stored in the laser cavity, such that each individual spontaneous emission event disturbs the phase of the field less. Strong optical absorption in III-V materials causes high losses, preventing currently-available semiconductor lasers from achieving ultra-narrow linewidths. This absorption is a natural consequence of the compromise between efficient electrical and efficient optical performance in a semiconductor laser. Some of the III-V layers must be heavily doped in order to funnel excited carriers into the active region, which has the side effect of making the material strongly absorbing.

This thesis presents a new technique, called modal engineering, to remove modal energy from the lossy region and store it in an adjacent low-loss material, thereby reducing overall optical absorption. A quantum mechanical analysis of modal engineering shows that modal gain and spontaneous emission rate into the laser mode are both proportional to the normalized intensity of that mode at the active region. If optical absorption near the active region dominates the total losses of the laser cavity, shifting modal energy from the lossy region to the low-loss region will reduce modal gain, total loss, and the spontaneous emission rate into the mode by the same factor, so that linewidth decreases while the threshold inversion remains constant. The total spontaneous emission rate into all other modes is unchanged.

Modal engineering is demonstrated using the Si/III-V platform, in which light is generated in the III-V material and stored in the low-loss silicon material. The silicon

is patterned as a high-Q resonator to minimize all sources of loss. Fabricated lasers employing modal engineering to concentrate light in silicon demonstrate linewidths at least 5 times smaller than lasers without modal engineering at the same pump level above threshold, while maintaining the same thresholds.

Chapter 1

Introduction

Narrow-linewidth laser sources are useful for many diverse applications, including coherent communication, stable frequency standards, nonlinear optics, and precision sensing. A narrow-linewidth semiconductor laser would have many advantages over the fiber lasers which currently dominate the narrow-linewidth market for many of the same reasons that integrated electronics dominate their field.

Semiconductor lasers drive modern fiber communications networks primarily because of their low cost, the ease of pumping them electrically, and the wide, somewhat tunable gain bandwidth of the underlying semiconductor gain material. Semiconductor lasers are also small and lightweight. Semiconductor lasers are versatile: they can be made to emit a single mode by introducing a periodic index or gain modulation, they can have output powers greater than $1\,\mathrm{W}$. Despite their advantages, semiconductor lasers suffer from poor phase noise performance compared to other types of lasers.

1.1 Narrow-linewidth laser sources in coherent communication

As demand for data continues to grow, fiber communication networks are transitioning to coherent communication formats in which the phase of the optical field is used to transmit information [1]. Coherent communication is more efficient spectrally compared to existing on-off keying because more bits can be sent per symbol (i.e.,

Amplitude-shift keying
(ASK)

Binary phase-shift keying
(BPSK)

Quadrature phase-shift keying
(QPSK)

8-Phase shift keying
(8-PSK)

16-Phase shift keying
(16-PSK)

16-Quadrature amplitude moduation
(16-QAM)
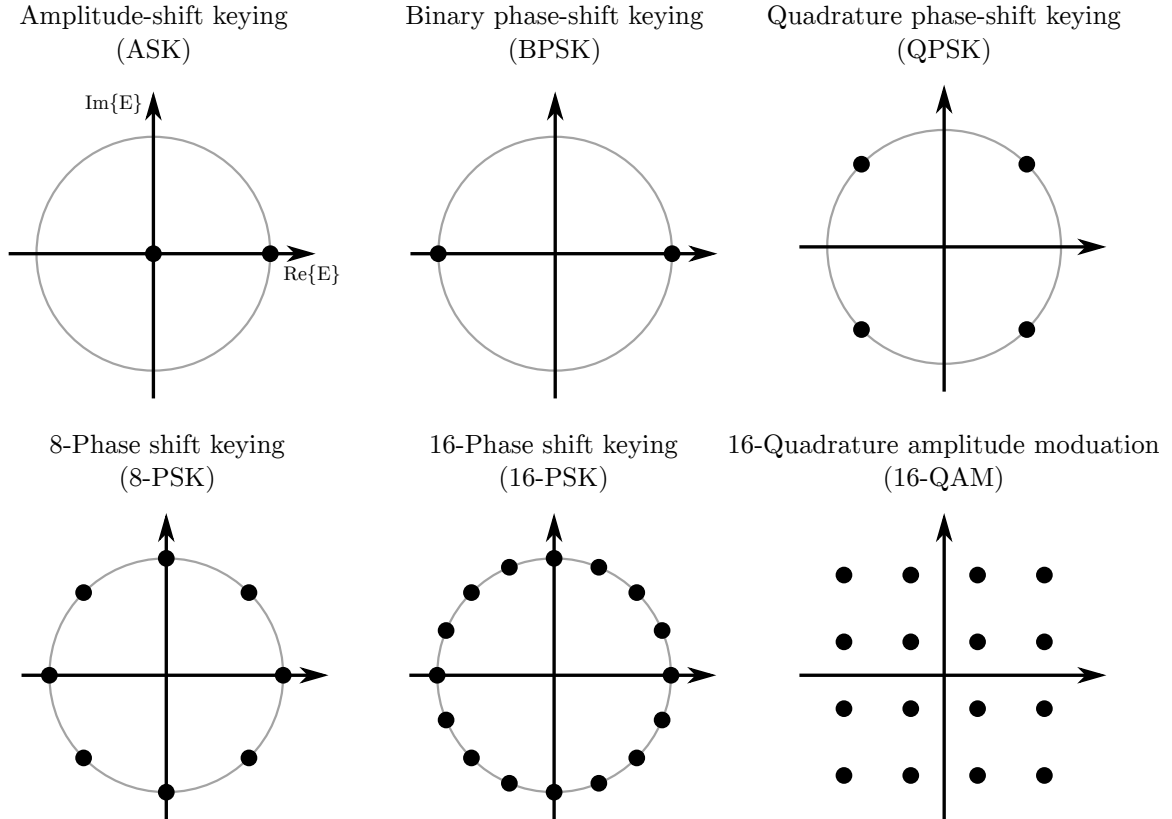
Figure 1.1: Constellation diagrams of some basic communication formats. The number of bits transmitted per symbol increases from the left to the right of the figure, increasing the symbol density.

coherent formats can support higher data rates per unit bandwidth). The drawback of using this format is that it is more sensitive to the phase noise (or, equivalently, linewidth) of the laser source. Figure 1.1 shows the constellation diagrams for some basic coherent communication formats. Each dot in the constellation diagram represents a symbol which is transmitted by setting the phasor of the electric field of the optical source at the transmitter to point at the symbol. The phasor is inevitably corrupted by noise from spontaneous emission, imperfections in the transmitter's laser source and modulator, from the channel over which the signal is sent, and from the receiver's own detection optics and electronics. Figure 1.2 shows an example of the probability distribution of the tip of the received phasor.

Shown at the top left of the figure is amplitude shift keying (ASK), or basic on-off modulation of the source. Phase noise is not important in ASK because information is
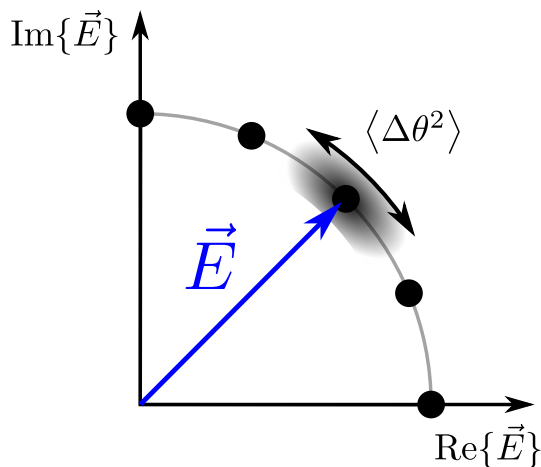
Figure 1.2: Example probability distribution cloud for the received electric field phasor, represented by the blue vector in the ideal case. The gray-shaded cloud represents where the noise-corrupted phasor may point. Phase noise spreads the cloud in the $\hat{\theta}$ direction while amplitude noise spreads the cloud in the $\hat{r}$ direction.

only transmitted by varying the amplitude of the signal and can be detected without measuring phase. The two symbols used in binary phase-shift keying (BPSK), the second constellation, are farther apart than those in ASK, so it should be easier for the receiver to decide which symbol was transmitted. However, BPSK is sensitive to phase noise because information is transmitted only by varying the phase of the signal. The symbols are 180° apart, so if the accumulated phase deviation during one symbol duration is greater than 90° in either direction, the wrong symbol will be decoded.

Additional bits per symbol can be transmitted by increasing the number of meaningful phases in the constellation. Continuing through the figure, the constellations for 4-, 8-, and 16-symbol phase shift keying can be seen. Clearly, these advanced formats are more susceptible to phase noise than the simple BPSK case.

Inexpensive, low phase noise sources are important in more areas than just communication. The high-Q optical resonators that are the focus of significant research today must be interrogated by laser sources with low phase and frequency noise. Coherent optical interactions, like parametric amplification, four-wave mixing, and stimulated Brillouin scattering require stable laser sources to operate.

1.2 Low phase noise Si/III-V lasers

Spontaneous emission is fundamentally a quantum mechanical process through which photons are emitted into the laser mode with random phases, perturbing the phase of the existing field in the laser cavity. Spontaneous emission is unavoidable, but its effects can be mitigated. Chapter 2 of this thesis calculates the spontaneous emission rate into a given mode using Fermi's Golden Rule, showing that the spontaneous transition rate into the laser mode can be reduced by decreasing the intensity of the mode at the active region. Absorption losses in the material straddling the active region will also decrease. Unfortunately, decreasing the intensity of the mode at the active region will also reduce the modal gain available to the laser mode.

Reducing the losses of a laser cavity provides two benefits to noise performance: (1) fewer excited carriers will be needed to reach threshold, resulting in less phase-corrupting spontaneous emission into the laser mode, and (2) more photons will be stored in the laser cavity, such that each individual spontaneous emission event will have a smaller effect on the phase of the field. Chapter 2 also describes this double-benefit of reducing losses.

Heterogeneous integration of silicon with III-V combines an efficient photon generator (III-V) with a low-loss material for efficient photon storage (silicon). Storing most of a Si/III-V laser's modal energy in low-loss silicon reduces the overall losses of the laser cavity compared to a III-V-only laser, producing a corresponding decrease in the linewidth of the laser. The straightforward way to reduce optical absorption using hybrid Si/III-V is to *replace* excess lossy III-V with low-loss silicon, which is equivalent to reducing losses while keeping gain constant. However, the need to pump the active material to transparency sets a minimum number of excited carriers needed to reach threshold, eventually leading to diminishing returns to linewidth as the only improvement comes from storing more photons. Hybrid Si/III-V lasers taken to the extreme of this replacement transformation will only receive a single benefit to linewidth at the margin.

This thesis presents *modal engineering* as a better alternative to replacing lossy

silicon with III-V. Modal engineering changes the shape of the laser mode, shifting modal energy away from the III-V and storing it in silicon. Modal engineering, properly executed, reduces modal gain, absorption loss in III-V, and spontaneous emission into the mode by the same factor. If absorption losses in III-V dominate the total cavity losses, the pumping threshold will remain constant while the spontaneous emission rate decreases. Chapter 3 details these two transformations, leading to the counterintuitive result that the smallest linewidths are achieved by reducing gain and loss by the same amount because there are no diminishing returns from transparency.

Experimental demonstrations of modal engineering in hybrid Si/III-V lasers are presented in chapters 4 and 5. As expected, linewidths become smaller as more of the mode is shifted away from the lossy III-V. Threshold currents are shown to remain constant.

Chapter 2

Phase noise in laser fields

Stimulated emission, which provides the gain in lasers, is inevitably accompanied by spontaneous emission, which introduces phase noise by combining incoherently with the laser field. This chapter will derive the effect of spontaneous emission on a laser field, producing some insightful results which can be exploited to reduce the linewidth of a semiconductor laser by using the hybrid Si/III-V platform.

Important results derived in this chapter are:

1. The single-carrier spontaneous transition rate into the laser mode is proportional to the intensity of the laser field at the active region (equation 2.35). The spontaneous transition rate into all other modes is independent of the lasing mode (equation 2.42).

2. The linewidth of a laser decreases with a decreased spontaneous emission rate into the lasing mode and with increasing number of photons stored in the cavity (equation 2.71).

3. The total spontaneous emission rate into the laser mode (carriers/second) decreases with decreased cavity losses, primarily because fewer excited carriers are needed to reach threshold (equation 2.61).

4. The number of photon stored in the cavity increases linearly with decreased cavity losses, with all other factors remaining costant (equation 2.65).

5. The net effect is that laser linewidth scales with μ/Q^2, where μ is the population inversion factor and Q is the quality factor of the cavity (equation 2.79).

2.1 Optical cavities

An optical resonator consists of a cavity that guides or reflects an optical wave back upon itself so that at resonance it matches up exactly with the original wave after each round trip. The electric field distribution of the wave is known as a "mode" of the cavity.

2.1.1 Loss

An optical wave may lose or gain energy as it travels through a cavity. The most common sources of optical loss are material absorption and scattering from imperfections in the material. Losses can be quantified as a fractional decrease in the number of photons in the optical mode (N_p) which is proportional to the intensity (I) of the wave [2, p.217]

$$-\alpha_\mathrm{mode} \equiv \frac{1}{I}\frac{\mathrm{d}I}{\mathrm{d}z} = \frac{1}{N_\mathrm{p}}\frac{\mathrm{d}N_\mathrm{p}}{\mathrm{d}z}, \tag{2.1}$$

where the modal loss coefficient per unit length is defined here as α_mode. The solution to this differential equation is an exponentially decaying intensity of the optical wave;

$$I(z) = I(0)\exp(-\alpha_\mathrm{mode}z). \tag{2.2}$$

The loss coefficient could also be defined as a decrease in amplitude, in which case it would be half of the value defined here. The intensity value will be used in this thesis.

The total loss experienced by a wave can be broken down into its various con-

stituent components as each affects the wave independently;

$$I(z) = I(0) \exp(-\alpha_1 z) \exp(-\alpha_2 z) \ldots \exp(-\alpha_n z)$$

$$= I(0) \exp[-(\alpha_1 + \alpha_2 + \ldots + \alpha_n)z]. \tag{2.3}$$

Therefore, the loss coefficient due to multiple sources $(i = 1, 2, \ldots)$ can be expressed as

$$\alpha_{\text{mode}} = \alpha_1 + \alpha_2 + \ldots + \alpha_n. \tag{2.4}$$

A cavity composed of different materials with different absorption coefficients is considered in this thesis. The total absorption due to the different materials can be found by using the confinement factor (Γ_i) which measures the fraction of the mode residing in each material i $(i = 1, 2, \ldots)$;

$$\Gamma_i = \frac{\int_i |E|^2 \, \mathrm{d}V}{\int_\infty |E|^2 \, \mathrm{d}V}. \tag{2.5}$$

Individual absorption coefficients from different materials $(\alpha_1, \alpha_2, \ldots)$ can then be weighted by the modal confinement factor in each material $(\Gamma_1, \Gamma_2, \ldots)$ to calculate the total absorption experienced by the mode.

$$\alpha_{\text{mode}} = \Gamma_1 \alpha_1 + \Gamma_2 \alpha_2 + \ldots \tag{2.6}$$

2.1.2   Gain

An active material can amplify an optical mode. The gain provided to the optical wave is quantified in the same way as the loss, as a fractional increase in the number of photons in the optical mode (N_{p}), which is proportional to the intensity (I) of the wave

$$g_{\text{mode}} \equiv \Gamma_{\text{act}} g \equiv \frac{1}{I} \frac{\mathrm{d}I}{\mathrm{d}z} = \frac{1}{N_{\text{p}}} \frac{\mathrm{d}N_{\text{p}}}{\mathrm{d}z}, \tag{2.7}$$

where g is the material gain, which would be the gain of a wave completely confined to the active region [2, p.722; 3, p.271; 4, p.568]. Commonly-used quantum well active

material is only a few nanometers thick, which is much smaller than the dimension of a typical cavity mode. Weighting the material gain by the modal confinement factor in the active region (Γ_{act}) then gives the modal gain (g_{mode}) experienced by the actual cavity mode. Modal gain provides a useful way to compare the effect of gain on two different modes with different confinements in the quantum wells, by keeping the "material gain" (g) constant.

The exponential material gain coefficient (g) is proportional to the stimulated emission rate. The rate equation for the total number of photons in the presence of stimulated emission (only) is

$$\frac{\mathrm{d}N_{\mathrm{p}}}{\mathrm{d}t} = R_{\text{st}}, \tag{2.8}$$

where the left-hand side of the equation is the rate of change in the total number of photons in the mode and the right-hand side is the net stimulated emission rate from all carriers in the active region. This equation is a statement that each (net) stimulated emission event adds one photon to the mode. Convert the definition of gain (equation 2.7) from a rate in space to a rate in time using the group velocity (v_{g})

$$\Gamma_{\text{act}}g \equiv \frac{1}{N_{\mathrm{p}}}\frac{\mathrm{d}N_{\mathrm{p}}}{\mathrm{d}z} = \frac{1}{N_{\mathrm{p}}v_{\mathrm{g}}}\frac{\mathrm{d}N_{\mathrm{p}}}{\mathrm{d}t} = \frac{R_{\text{st}}}{N_{\mathrm{p}}v_{\mathrm{g}}}. \tag{2.9}$$

2.1.3   Quality factor

The quality factor of a cavity (Q) is defined to be a ratio of the energy stored by a cavity to the power lost [2, p.155]

$$Q = \frac{\omega E_{\text{stored}}}{P_{\text{lost}}}. \tag{2.10}$$

The stored energy is scaled by the angular frequency of the light (ω) to give the unitless quality factor. A cavity that can store a lot of energy has a high quality factor. The quality factor can be written in terms of the photon lifetime inside the cavity (τ_{p}) to be [2, p.193]

$$Q = \omega\tau_{\mathrm{p}}. \tag{2.11}$$

The quality factor can be related to an average loss coefficient in space over the length of a cavity (α) using the group velocity of the wave

$$Q = \frac{\omega}{v_g \alpha}. \tag{2.12}$$

The total Q_{total} of a cavity can be broken down into its constituent parts by combining equations 2.4 for adding loss coefficients and 2.12 for converting loss coefficients to Q values

$$Q_{\text{total}}^{-1} = Q_1^{-1} + Q_2^{-1} + \ldots + Q_n^{-1}. \tag{2.13}$$

2.1.4 Threshold condition

As the modal gain is increased from zero, it will eventually balance out the losses the mode experiences. At this point, the optical wave will return to the same amplitude and phase after each round trip of the cavity and steady-state oscillation will result. The material gain required to achieve oscillation is the threshold gain (g_{th}), which can be expressed in terms of Q by equation 2.12

$$\Gamma_{\text{act}} g_{\text{th}} = \alpha_{\text{total}}$$
$$= \frac{\omega}{v_g Q_{\text{total}}}. \tag{2.14}$$

2.2 Interaction of carriers with cavity modes

Electrical carriers interact with optical waves in three ways: stimulated emission, stimulated absorption, and spontaneous emission, each depicted in figure 2.1. Electron-hole pairs in a semiconductor are similar to "atoms" with an excited state (electron in the conduction band) and a ground state (electron in the valence band). Quantum states for the atom-cavity mode system can be written as $|i, N_p\rangle$, where i is the electron state ($i = 2$ is excited, 1 is ground) and N_p is the number of photons in the cavity mode. Downward atomic transitions, whether stimulated or spontaneous, take a quantum of energy from the electron and generate a new photon with the same

Spontaneous emission   Stimulated emission   Absorption

"atom"   cavity mode
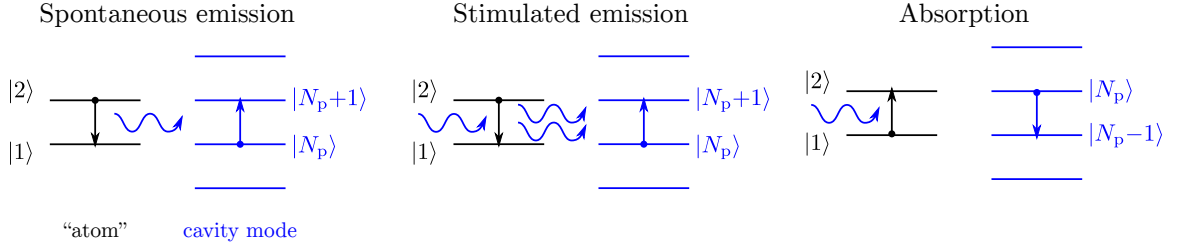
Figure 2.1: The three basic ways in which electrical carriers in a semiconductor interact with optical waves. The black lines represent electronic states and the blue lines represent photon states. The blue sine waves represent photons either approaching or leaving the atom.

quantum of energy ($|2, N_\mathrm{p}\rangle \to |1, N_\mathrm{p}+1\rangle$). Absorption does the reverse.

Transition rates for a single carrier to undergo each type of transition from a given initial state $|i, N_{\mathrm{p}i}\rangle$ to a final state $|f, N_{\mathrm{p}f}\rangle$ can be found using Fermi's Golden Rule. Two situations will be considered in this section: the interaction of the atom with a single optical mode and the interaction of the atom with all modes existing in the optical cavity.

2.2.1   Spontaneous transitions into the lasing mode

Fermi's Golden Rule can be used to calculate the transition rate ($W^l_{i \to f}$, number/sec) of one atom interacting with a single optical mode, denoted l [3, p.54]

$$W^l_{i \to f}(f_l) = \frac{2\pi}{\hbar}\ |\langle f, N_{\mathrm{p}f}|\, \mathcal{H}' \,|i, N_{\mathrm{p}i}\rangle|^2 \, \frac{\delta(f_l = f_i - f_f)}{2\pi\hbar} \tag{2.15}$$

$$\equiv \frac{1}{\hbar^2}\ |\mathcal{H}'_{fi}|^2 \ \delta(f_l = f_i - f_f), \tag{2.16}$$

where f_l is the frequency of optical mode l, $\mathcal{H}'$ is the interaction Hamiltonian for the atom-mode system, $\mathcal{H}'_{fi}$ is the Hamiltonian matrix element coupling electronic state $|i\rangle$ to state $|f\rangle$, and $f_i - f_f$ is the transition frequency calculated from the energy separation of the two electronic states. The interaction Hamiltonian for this system is the linear dipole Hamiltonian, given by [3, p.663]

$$\mathcal{H}' = -q\vec{E} \cdot \vec{r}, \tag{2.17}$$

where q is the electron charge, $\vec{E}$ is the electric field amplitude vector of the optical mode, and $\vec{r}$ is the electron-hole dipole separation.

The electric field can be quantized as an expansion over the normal modes of a cavity [3, p.94]. The electric field of optical mode l can be written [3, p.98]

$$\vec{E}(\vec{r}, t) = -i\hat{e} \sqrt{\frac{\hbar\omega}{2\epsilon}} \left[a_l^\dagger(t) - a_l(t) \right] E_0^l(\vec{r}), \tag{2.18}$$

where $a_l^\dagger$ is the photon creation operator, a_l is the photon annihilation operator (both acting on mode l), and E_0^l is the normalized electric field distribution of mode l (units of volume$^{-1/2}$). It is normalized as

$$\int_{V_c} E_0^l(\vec{r}) \; E_0^m(\vec{r}) \; dV = \delta_{lm}. \tag{2.19}$$

With this normalization, the confinement factor for mode l in region i is (equation 2.5)

$$\Gamma_i = \int_i \left| E_0^l(\vec{r}) \right|^2 \; dV. \tag{2.20}$$

This electric field and the associated magnetic field satisfy Maxwell's equations with the cavity boundary conditions in order to be a cavity mode.

The quantized electric field can be used to calculate the interaction Hamiltonian matrix element $(\mathcal{H}'_{fi})$;

$$|\mathcal{H}'_{fi}|^2 \equiv |\langle f, N_{pf}| \, \mathcal{H}' \, |i, N_{pi}\rangle|^2 \tag{2.21}$$

$$= |\langle f, N_{pf}| \, i\,q \, \sqrt{\frac{\hbar\omega}{2\epsilon}} \, (a_l^\dagger - a_l) \, \hat{e} \cdot \vec{r} \, E_0^l(\vec{r}) \, |i, N_{pi}\rangle|^2. \tag{2.22}$$

Assume the normalized electric field varies slowly on the scale of the atom. Then, the dipole term acts like a delta function, pulling the normalized electric field at the position of the atom $(\vec{r_a})$ out of the integral;

$$|\mathcal{H}'_{fi}|^2 = \frac{q^2 \hbar\omega}{2\epsilon} \, |E_0^l(\vec{r_a})|^2 \, |\langle f, N_{pf}| \, (a_l^\dagger - a_l)\hat{e} \cdot \vec{r} \, |i, N_{pi}\rangle|^2. \tag{2.23}$$

Evaluating the integral depends on the specific initial and final states because the creation and annihilation operators will only couple certain states.

Downward atomic transitions from state $|2, N_{\mathrm{p}}\rangle$ to state $|1, N_{\mathrm{p}}+1\rangle$: the photon creation operator couples these two states, giving the new term $\sqrt{N_{\mathrm{p}}+1}$. The matrix element is

$$
\begin{aligned}
|\mathcal{H}'_{12}|^2 &= \frac{q^2 \hbar \omega}{2\epsilon} \, |E_0^l(\vec{r_{\mathrm{a}}})|^2 \, (N_{\mathrm{p}} + 1) \, |\langle 1| \, \hat{e} \cdot \vec{r} \, |2\rangle|^2 \\
&\equiv \frac{q^2 \hbar \omega}{2\epsilon} \, |E_0^l(\vec{r_{\mathrm{a}}})|^2 \, (N_{\mathrm{p}} + 1) \, r_{12}^2,
\end{aligned}
\tag{2.24}
$$

where $r_{12} \equiv |\langle 1| \vec{r} |2\rangle|$ and perfect alignment between the electric field polarization and the dipole separation has been assumed. The magnitude of the dipole matrix element is a property of the atom.

Upward atomic transitions from state $|1, N_{\mathrm{p}}+1\rangle$ to state $|2, N_{\mathrm{p}}\rangle$: the photon annihilation operator couples these two states, giving the new term N_{p}. The matrix element is

$$
|\mathcal{H}'_{21}|^2 = \frac{q^2 \hbar \omega}{2\epsilon} \, |E_0^l(\vec{r_{\mathrm{a}}})|^2 \, N_{\mathrm{p}} \, r_{21}^2.
\tag{2.25}
$$

The dipole operator is Hermitian, so the magnitudes of the two dipole matrix elements are equal ($r_{21}^2 = r_{12}^2$).

Inserting the interaction Hamiltonian matrix elements into Fermi's Golden Rule (equation 2.16) gives the upward and downward transition rates for a single atom interacting with mode l. The downward atomic transition rate is

$$
W_{12}^l(f_l) = \frac{q^2 \pi f}{\hbar \epsilon} \, |E_0^l(\vec{r_{\mathrm{a}}})|^2 \, (N_{\mathrm{p}} + 1) \, r_{12}^2 \, \delta(f_l = f_i - f_f)
\tag{2.26}
$$

$$
\equiv W_{\mathrm{st,down}}^l + W_{\mathrm{sp}}^l.
\tag{2.27}
$$

The term $(N_{\mathrm{p}} + 1)$ is conventionally interpreted as the sum of stimulated and spontaneous emissions, in which the N_{p} component represents the stimulated transitions and the $+1$ term represents spontaneous transitions. This means that the spontaneous emission rate is the same as the stimulated downward rate if only one photon

were in the mode. This result indicates that the vacuum field (i.e., the mode with no photons in it, $N_p = 0$) can induce transitions spontaneously. Thus, spontaneous emission is unavoidable even with zero photons in the mode (in fact spontaneous emission is needed to create the first photon in the mode, "starting" the laser).

The upward atomic transition rate (W_{21}^l) can also be calculated using Fermi's Golden Rule

$$W_{21}^l(f_l) = \frac{q^2 \pi f}{\hbar \epsilon} \; |E_0^l(\vec{r_a})|^2 \; N_p \; r_{12}^2 \; \delta(f_l = f_i - f_f) \tag{2.28}$$

$$\equiv W_{\text{st,up}}^l. \tag{2.29}$$

The upward transition rate does not contain the spontaneous ($+1$) term. Physically, this is because energy can not be taken from the vacuum field.

By comparing equations 2.26 and 2.28, it is clear that the upward and downward stimulated transition rates are equal;

$$W_{\text{st,down}}^l = W_{\text{st,up}}^l \equiv W_{\text{st}}^l. \tag{2.30}$$

The spontaneous transition rate into a mode therefore is related to the stimulated rate by the number of photons in the mode;

$$W_{\text{sp}}^l = \frac{W_{\text{st}}^l}{N_p}. \tag{2.31}$$

Lineshape broadening

The delta function in the equations for the transition rates ensures that transitions only occur at the transition frequency ($E_i - E_f/h$). In reality, the transition frequency and cavity resonance frequency are broadened by lineshape functions $g(f)$. All lineshape functions are normalized such that

$$\int_{-\infty}^{\infty} g(f) \; df = 1. \tag{2.32}$$

The spontaneous transition rate into mode l including the effects of broadening can be calculated by integrating W^l_{sp} over the appropriate lineshape functions.

Homogeneous broadening: Each atom is affected in the same way, introducing a lineshape function $g_{\text{h}}(f_{\text{t}} - f_{\text{h}})$ centered on f_{h}. The transition frequency (f_{t}) is calculated from the energy difference between the two atomic states.

Inhomogeneous broadening: Different atoms have different transition frequencies and are distinguishable. A single atom, therefore, cannot be inhomogeneously broadened. However, this term will be included because the calculated spontaneous transition rate will eventually be used to describe a laser cavity with many excited atoms, which will be affected by inhomogeneous broadening. Inhomogeneous broadening acts on the homogeneous center frequency, introducing a lineshape function $g_{\text{i}}(f_{\text{h}} - f_{\text{i}})$ centered on f_{i}.

Cavity lineshape : The cavity mode has a finite width due to a finite photon lifetime, introducing a term $g_{\text{c}}(f - f_{\text{c}})$ centered on f_{c}.

Combining these lineshapes, integrating over them in Fermi's Golden Rule, and taking the spontaneous ($+1$) term yields the spontaneous transition rate into mode l under the effect of lineshape broadening

$$W^l_{\text{sp}} = \frac{q^2 \pi f r_{12}^2}{\hbar \epsilon} |E^l_0(\vec{r_{\text{a}}})|^2 \int_\infty \int_\infty \int_\infty g_{\text{i}}(f_{\text{h}} - f_{\text{i}}) g_{\text{c}}(f - f_{\text{c}}) g_{\text{h}}(f_{\text{t}} - f_{\text{h}}) \delta(f - f_{\text{t}}) \, \mathrm{d}f \, \mathrm{d}f_{\text{h}} \, \mathrm{d}f_{\text{t}}.$$

(2.33)

Inhomogenous broadening is the most significant source of broadening in the active materials commonly used for semiconductor lasers which have many different, distinguishable electronic states. Common gain materials have a gain bandwidth on the order of $\Delta f_{\text{i}} = 30\,\text{nm}$, much broader than the cavity resonance width or linewidth contribution from homogeneous broadening. Compared to the inhomogeneous broadening function, the other two lineshape functions are essentially delta functions. Approximating them as delta functions, the spontaneous transition rate into mode l

is

$$W_{\text{sp}}^l = \frac{q^2 \pi f r_{12}^2}{\hbar \epsilon} \, g_{\text{i}}(f_{\text{c}} - f_{\text{i}}) \, |E_0^l(\vec{r_{\text{a}}})|^2 \tag{2.34}$$

$$\approx \frac{q^2 \pi f r_{12}^2}{\hbar \epsilon} \, \frac{1}{\Delta f_{\text{i}}} \, |E_0^l(\vec{r_{\text{a}}})|^2 \tag{2.35}$$

$$\propto |E_0^l(\vec{r_{\text{a}}})|^2. $$

The inhomogeneous lineshape function has been approximated as rectangular with a width of Δf_{i}. Notably, the spontaneous transition rate into the laser mode is proportional to the squared magnitude of the normalized electric field at the atom ($|E_0^l(\vec{r_{\text{a}}})|^2$).

If a gain medium with little to no inhomogeneous broadening is used, like a single atom or quantum dot, the cavity lineshape may be the widest lineshape function and Δf_{c} will replace Δf_{i} in equation 2.35. In this case, the transition rate will depend on the cavity resonance width. This would be the Purcell effect [5], which can be observed in narrow-linewidth cavities which host single quantum emitters (that are not affected by inhomogeneous broadening).

2.2.2 Spontaneous transitions into all modes

For large laser cavities much bigger than λ^3, many modes other than the lasing mode will interact with the atom. The frequency density of these other modes (ρ_{m}, total number of modes per unit frequency) in a cavity can be calculated by modeling the large cavity as a box with perfectly conducting boundary conditions and counting the modes. The result of this calculation is [2, p.160; 4, p.194,561]

$$\rho_{\text{m}} = \frac{8\pi f^2 n^3 V_{\text{c}}}{c^3}, \tag{2.36}$$

where V_{c} is the volume of the cavity. Common semiconductor lasers have a cavity volume of around $1\,\text{mm} \times 2\,\mu\text{m} \times 1\,\mu\text{m}$ and a gain bandwidth of $30\,\text{nm}$, so the total number of modes interacting with the carriers is around 1×10^4.

Fermi's Golden Rule takes a different form when calculating the transition rate of an atom interacting with a continuum of modes [3, p.53]

$$W_{i \to f} = \frac{1}{\hbar^2} |\mathcal{H}'_{fi}|^2 \rho_{\mathrm{m}}(f = f_i - f_f). \tag{2.37}$$

The total spontaneous transition rate into all of these other modes is calculated by inserting the density of the cavity modes (equation 2.36) into this equation and taking the $+1$ term from the Hamiltonian matrix element (dropping the N_{p} term)

$$W_{\mathrm{sp}}^{\mathrm{free}} = \frac{q^2 \pi f}{\hbar \epsilon} |E_0^{\mathrm{avg}}(\vec{r_{\mathrm{a}}})|^2 |\langle 1| \hat{e} \cdot \vec{r} |2\rangle|_{\mathrm{avg}}^2 \left(\frac{8\pi f^2 n^3 V_{\mathrm{c}}}{c^3} \right). \tag{2.38}$$

Because many modes are interacting with the atom, the normalized electric field relevant to spontaneous emission will be the average normalized field at the atom for each mode. Contributions from any individual modes for which the atom resides at a maximum or null will average out. The average value of the normalized field for any mode m is

$$|E_0^{\mathrm{avg}}|^2 = \frac{1}{V_{\mathrm{c}}} \int_{V_{\mathrm{c}}} |E_0^m(\vec{r})|^2 \, dV \tag{2.39}$$

$$= \frac{1}{V_{\mathrm{c}}} \tag{2.40}$$

by the normalization condition (equation 2.19).

The dot product between the electric field polarization ($\hat{e}$) and the atom dipole ($\vec{r}$) will yield an averaging factor of one third of the maximum value (r_{12}^2) for an atom in free space. Electron-hole pairs in quantum wells, on the other hand, will interact with any electric field polarized in the plane of the well [2, p.720], so the averaging factor is increased to one half for quantum well material. The quantum well averaging factor will be used here

$$|\langle 1| \hat{e} \cdot \vec{r} |2\rangle|_{\mathrm{avg}}^2 = \frac{r_{12}^2}{2}. \tag{2.41}$$

Combining these results, the total spontaneous emission rate of a quantum well

active material into all cavity modes is

$$W_{\text{sp}}^{\text{free}} = \frac{4\pi^2 f^3 n^3 q^2 r_{12}^2}{\hbar \epsilon c^3}. \tag{2.42}$$

2.2.3 The spontaneous emission coupling factor

It is useful to define the spontaneous emission coupling factor (β_{sp}^l) to be the fraction of the total spontaneous emission that enters mode l

$$\beta_{\text{sp}}^l \equiv \frac{W_{\text{sp}}^l}{W_{\text{sp}}^{\text{free}} + W_{\text{sp}}^l} \approx \frac{W_{\text{sp}}^l}{W_{\text{sp}}^{\text{free}}}, \tag{2.43}$$

where the approximation is valid if there are many modes besides mode l interacting with the active medium. Substituting the calculated spontaneous transition rates (equations 2.35 and 2.42) into this equation yields

$$\beta_{\text{sp}}^l = \frac{1}{4\pi} \left(\frac{c}{fn}\right)^3 \frac{f}{\Delta f_i} |E_0^l(\vec{r_a})|^2 \tag{2.44}$$
$$\propto |E_0^l(\vec{r_a})|^2.$$

The fraction of spontaneous emission that couples into mode l is proportional to the normalized intensity of mode l at the atom. Engineering the shape of mode l to reduce its "intensity" $(|E_0^l(\vec{r_a})|^2)$ at the atom therefore reduces the spontaneous transition rate into mode l without affecting the overall spontaneous transition rate into all modes. Figure 2.2 illustrates this effect.

2.2.4 Stimulated transitions

Performing the same calculations but including the N_p term that was left out when considering the spontaneous transition rate will show that the stimulated net downward transition rate (i.e., modal gain, equation 2.9) is also proportional to $|E_0^l(\vec{r_a})|^2$. In a laser, reduced modal gain would mean that more excited atoms are needed to reach threshold, negating any benefits coming from reducing the single-atom transi-
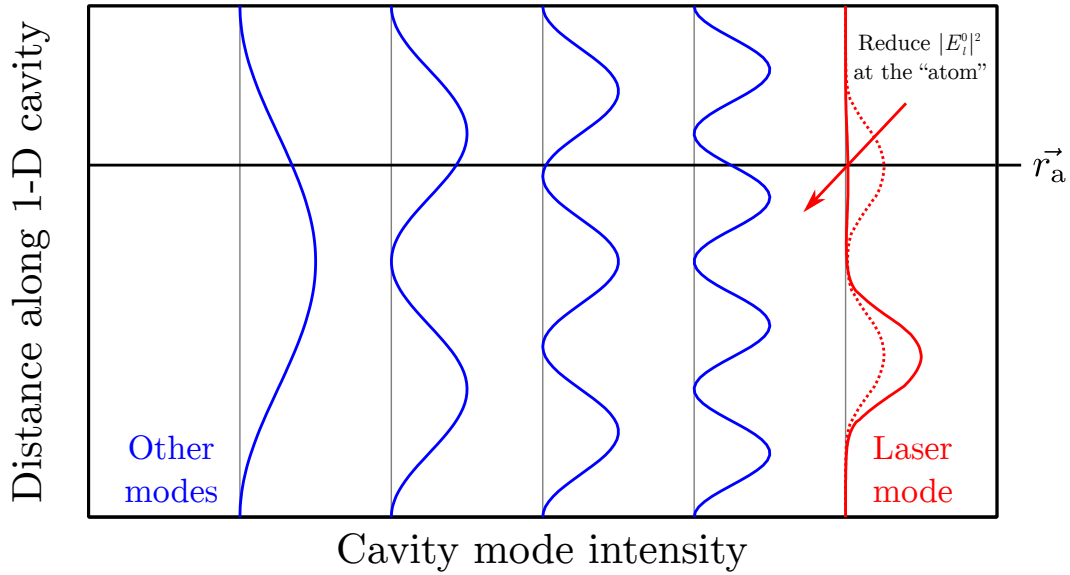
Figure 2.2: Cartoon of various one-dimensional cavity modes interacting with the atom. The labeled horizontal line represents the location of the atom in the 1-D cavity. Reducing the intensity of the laser mode at the atom will reduce the spontaneous transition rate into the laser mode. In the figure, the modes have been spaced horizontally for easier viewing.

tion rate.

Fortunately, absorption (stimulated upward transitions) in the material immediately surrounding the active region will similarly depend on the intensity of the mode near the active region. This analysis suggests that spontaneous emission, net gain, and absorption loss from regions near the active region will scale at the same rate with the normalized electric field intensity at the active region. If absorption near the active region dominates total loss, shifting the mode away from the active region will reduce modal gain and total loss by the same factor, and threshold inversion will remain constant. Therefore, spontaneous emission into the laser mode can be reduced by decreasing the normalized electric field intensity at the active region *if the total cavity losses are dominated by absorption near the active region.*

2.3 A phenomenological calculation of spontaneous emission into a lasing mode above threshold

The spontaneous transition rate for a single excited carrier (W_{sp}) that was calculated in the previous section can be extended to calculate the rate for all carriers by integrating over each carrier. This approach yields the total spontaneous emission rate into the mode while providing a phenomenological description of the process.

2.3.1 Number of carriers

The number of excited carriers in a semiconductor laser is related to the material gain. Gain in semiconductor lasers monotonically increases with carrier inversion, and therefore with carrier density [6]. Material gain as a function of carrier density can be approximated for positive gain by the empirical equation [4, p.64]

$$g \approx g_0 \ln \frac{N}{N_{tr}}. \tag{2.45}$$

where g_0 is an empirical coefficient, N is the number of excited carriers in the semiconductor, and N_{tr} is the number of carriers at which the material is transparent, at which gain is zero and above which gain is positive. Figure 2.3 shows the relationship. Typical numbers for quantum well material are $N_{tr} \approx 2 \times 10^{18}\,\mathrm{cm}^{-3}$ and $g_0 \approx 3000\,\mathrm{cm}^{-1}$ [4, p.224]. In reality, there is a maximum modal gain which occurs when the medium is completely inverted. This approximation does not have a maximum, and is therefore only useful near transparency. Noise behavior is best near transparency, so lasers designed to have narrow linewidths should operate near transparency and therefore conforms well to the approximation.

2.3.2 Total spontaneous emission rate

Let the total number of excited atoms in the active region be given as N_2. Assume they are evenly distributed throughout the active volume (V_{act}), such that their density is
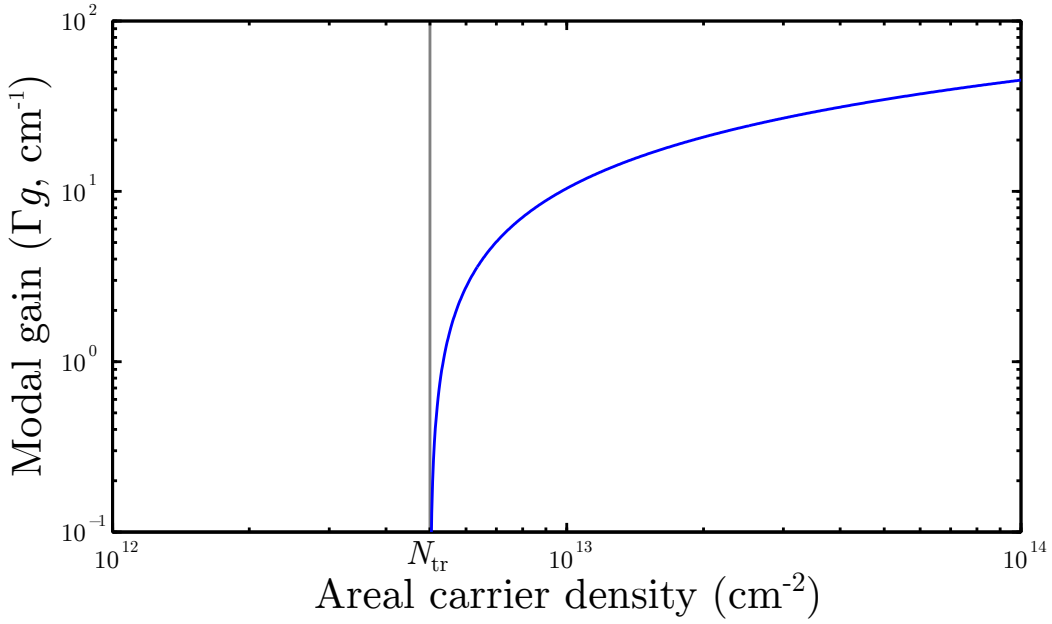
Figure 2.3: Approximation to material gain in a semiconductor, after equation 2.45. Assumptions: $g_0 = 3 \times 10^3 \, \text{cm}^{-1}$, $N_{\text{tr}} = 5 \times 10^{12} \, \text{cm}^{-2}$.

N_2/V_{act}. Then, the total spontaneous emission rate into mode l (R_{sp}^l) can be found by integrating this density over the active volume

$$R_{\text{sp}}^l = \int_{V_{\text{act}}} W_{\text{sp}}^l \left(\frac{N_2}{V_{\text{act}}} \right) \, dV \tag{2.46}$$

$$= \frac{q^2 \pi f r_{12}^2}{\hbar \epsilon (\Delta f_{\text{i}})} \left(\frac{N_2}{V_{\text{act}}} \right) \int_{V_{\text{act}}} |E_0^l(\vec{r})|^2 \, dV \tag{2.47}$$

Integrating the normalized electric field over the active region yields the confinement factor of the mode in the active region (equation 2.20), so the total spontaneous emission rate into mode l is proportional to Γ_{act}.

$$R_{\text{sp}}^l = \frac{q^2 \pi f r_{12}^2 N_2}{\hbar \epsilon (\Delta f_{\text{i}}) V_{\text{act}}} \Gamma_{\text{act}} \tag{2.48}$$

$$\propto \Gamma_{\text{act}}.$$

Take mode l to be the lasing mode. An intuitive physical description of the spontaneous emission rate into the laser lasing above threshold is given by the phe-

nomenological equation

$$R_{\text{sp}}^l = N_{\text{th}} W_{\text{sp}}^l = \frac{\beta_{\text{sp}}^l N_{\text{th}}}{\tau_{\text{sp}}},$$ (2.49)

where β_{sp}^l is the fraction of the total spontaneous emission that couples to the lasing mode (given by equation 2.44), N_{th} is the total number of excited atoms which clamps at its threshold value, and τ_{sp} is the spontaneous emission lifetime of the atoms due to emission into all modes (given by the inverse of the spontaneous transition rate, equation 2.42).

This phenomenological equation is true by the definition of β_{sp}^l, but it is hard to calculate each parameter individually. In a semiconductor, the number of excited carriers at threshold is estimated using an empirical equation found in the previous section or can be calculated by modeling band structures with many assumptions. The spontaneous emission coupling factor and spontaneous transition rate into all modes were found by considering Fermi's Golden Rule. Unfortunately, β_{sp}^l depends on the inhomogeneously-broadened lineshape (Δf_{i}), which increases as N_{th} increases because lower-energy states fill. Therefore, β_{sp}^l is not independent of N_{th}, making the calculation difficult.

2.4 Phasor description of phase noise in a laser

A laser will exhibit phase noise and a linewidth due to spontaneous emission into the laser mode which modulates the phase randomly. This basic linewidth of a laser due to phase noise will be calculated in this section following the reasoning of [2, p.484].

Consider the semiconductor gain medium to be a two-level gain medium with a population density in the excited level of N_2 and in the ground state of N_1. In the absence of other absorption, this medium will amplify an optical wave passing through it if $N_2 > N_1$, which is the condition for net positive stimulated emission. Because a laser must have positive gain to balance the optical losses of the cavity, there must be excited atoms in the laser cavity, some of which will transition to their ground state spontaneously, emitting photons with random phase into the laser mode.
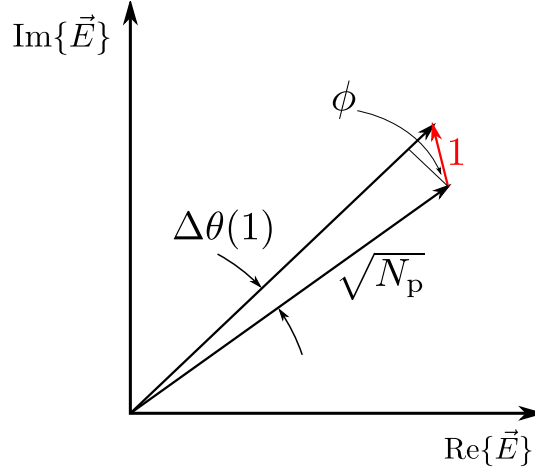
Figure 2.4: The effect of one spontaneous emission event on the electric field inside the laser cavity. The exiting field is shown as a phasor with magnitude $\sqrt{N_\mathrm{p}}$ and the phasor due to the spontaneous emission is shown in red. The combined phasor is shown on top.

This spontaneous emission has no defined phase relationship to the optical wave, unlike stimulated emission which is emitted with the same phase and direction as the stimulating wave. Figure 2.4 shows the effect of a single spontaneous emission event on the phasor of the pre-existing electric field in the laser cavity. The existing electric field is taken to contain N_p photons, and thus has a magnitude proportional to $\sqrt{N_\mathrm{p}}$. In these units, the spontaneous photon combining with the existing field has a magnitude of 1; however, it has a random phase relationship to the existing field, denoted as an angle ϕ which has uniform probability distribution on $[0°, 360°)$.

The effect of this one spontaneous emission on the phase of the existing electric field is then given by $\Delta\theta(1)$, which can be calculated using a small-angle approximation for $\Delta\theta(1)$, which is true in the case of a laser which would have $\sqrt{N_\mathrm{p}} \gg 1$;

$$\tan(\Delta\theta(1)) \approx \Delta\theta(1) = \frac{\cos\phi}{\sqrt{N_\mathrm{p}}}, \quad \sqrt{N_\mathrm{p}} \gg 1. \tag{2.50}$$

The spontaneous emission events are independent of each other, so the cumulative effect of N individual spontaneous emission events can be expressed as a variance in

the probability of the final position, like a random walk in phase space;

$$
\begin{aligned}
\left\langle \Delta\theta^2(N) \right\rangle &= \left\langle \Delta\theta^2(1) \right\rangle N \\
&= \frac{\left\langle \cos^2(\phi) \right\rangle}{N_\mathrm{p}} N \\
&= \frac{N}{2N_\mathrm{p}}.
\end{aligned}
\tag{2.51}
$$

The relevant number of spontaneous emission events (N) to consider is the number that are emitted during the duration of one transmitted symbol. Phase drift on timescales longer than the symbol duration can be compensated for by taking differential measurements between one symbol and the next or by tracking the drift with the local oscillator. Spontaneous emission into the laser mode occurs at an average rate R_sp (photons/sec), so that $N = R_\mathrm{sp}T$ spontaneous emission events happen during one symbol period T;

$$
\left\langle \Delta\theta^2(T) \right\rangle = \frac{R_\mathrm{sp}}{2N_\mathrm{p}}T.
\tag{2.52}
$$

Equation 2.52 provides a simple recipe for minimizing phase noise in a laser. Given a fixed symbol time, the two parameters which the laser design may control are R_sp, the average rate of spontaneous emission into the laser mode, and N_p, the average number of photons existing in the laser mode. Conceptually, these represent *spontaneous photon generation* and *photon storage*. A low-noise laser design will reduce spontaneous emission into the mode and increase photon storage in the cavity.

2.4.1   Spontaneous photon generation

One of the two keys to making a low-noise laser is to reduce the rate of spontaneous photon generation, so that fewer phase-perturbing events occur. The total spontaneous emission rate is related to the stimulated emission rate by quantum mechanics (equation 2.31), and the stimulated rate is known in a laser because the number of newly generated photons must exactly balance the number of photons lost.

The total stimulated and spontaneous emission rates into the lasing mode can be

found by multiplying the single-carrier transition rates (see section 2.2) by the total number of electrical states in the active region and accounting for the probability that the initial state is occupied and the final state is unoccupied.

$$R_{\text{st}}^{21} = \rho_{\text{r}}(E_{21}) \ V_{\text{act}} \ W_{\text{st}} \ f_1 \ (1 - f_2) \tag{2.53}$$

$$R_{\text{st}}^{12} = \rho_{\text{r}}(E_{21}) \ V_{\text{act}} \ W_{\text{st}} \ f_2 \ (1 - f_1) \tag{2.54}$$

$$R_{\text{sp}} = \rho_{\text{r}}(E_{21}) \ V_{\text{act}} \ W_{\text{sp}} \ f_2 \ (1 - f_1), \tag{2.55}$$

where R_{st}^{fi} is the rate of stimulated transitions from initial electronic state $|i\rangle$ into final state $|f\rangle$ (total number per second) and R_{sp} is the spontaneous transition rate from electronic state $|2\rangle$ to state $|1\rangle$ (total number per second). The density of electrical state pairs with an energy difference E_{fi} is referred to as the "reduced density of states" [4, p.581] or the "joint density of states" [7, p.606] and is given the symbol $\rho_{\text{r}}(E_{fi})$. Therefore, $\rho_{\text{r}}(E_{fi})V_{\text{act}}$ is the total number of energy states with energy difference E_{fi}, and f_i is the Fermi factor giving the probability that a state with the given energy is occupied:

$$f_1 = \frac{1}{\exp[(E_1 - E_{\text{Fv}})/kT] + 1} \tag{2.56}$$

$$f_2 = \frac{1}{\exp[(E_2 - E_{\text{Fc}})/kT] + 1},$$

where E_{Fv} is the quasi-Fermi level for the valence band, and E_{Fc} is the quasi-Fermi level for the conduction band. The semiconductor transition rates are slightly different than those for atomic systems because the probability that the final state is unoccupied by a carrier, $(1 - f_f)$, must be included. Otherwise, the atomic population N_i in state $|i\rangle$ is equivalent to the semiconductor population given by

$$N_i \leftrightarrow \rho_{\text{r}}(E_{fi})V_{\text{act}}f_i. \tag{2.57}$$

The net downward stimulated emission rate (R_{st}) has a known value in a laser

above threshold because it must exactly balance the loss rate;

$$R_{\text{st}} = R_{\text{st}}^{12} - R_{\text{st}}^{21} \tag{2.58}$$

$$= \rho_{\text{r}}(E_{21}) \, V_{\text{act}} \, W_{\text{st}} \, (f_2 - f_1). \tag{2.59}$$

Then, equations 2.53-2.55 combine with equation 2.31, relating the spontaneous and stimulated transition rates via quantum mechanics, to give the ratio of spontaneous emission to net stimulated emission:

$$\frac{R_{\text{sp}}}{R_{\text{st}}} = \frac{1}{N_{\text{p}}} \frac{f_2 \, (1 - f_1)}{f_2 - f_1} \equiv \frac{\mu}{N_{\text{p}}}, \tag{2.60}$$

where the population inversion factor μ has been defined to absorb the Fermi factors. Last, the total spontaneous emission rate into the laser mode can be found by using equation 2.9 to express R_{st} above threshold in terms of modal gain and equation 2.14 to express threshold modal gain in terms of cavity Q

$$R_{\text{sp}} = \frac{\omega\mu}{Q}. \tag{2.61}$$

Intuitively, this equation suggests that the spontaneous emission rate will decrease with increased cavity Q (i.e., reduced loss) because fewer excited carriers are needed to reach threshold. However, fewer excited carriers means an increased population inversion factor (μ), so some of the benefit is lost. Careful attention must be paid to the population inversion factor when calculating the spontaneous emission rate.

2.4.2 Photon storage

The other key to obtaining a low-noise laser output field is to increase the number of photons stored in the laser cavity, so a single spontaneous emission event constitutes a smaller perturbation on the laser field phasor. This is analogous to storing energy in a flywheel. As more energy is stored, the rotation frequency of the flywheel is less susceptible to small perturbations. The number of photons stored in the laser cavity

can be calculated by considering the rate equation for electrical carriers in the active medium,

$$\frac{dN}{dt} = \frac{\eta_i I}{q} - \frac{N}{\tau_{sp}} - v_g \Gamma_{act} g N_p, \tag{2.62}$$

where N is the total number of electrical carriers, η_i is the internal electrical injection efficiency (i.e., the fraction of injected carriers that make it to the active region), I is the pump current, q is the electron charge, and τ_{sp} is the spontaneous emission lifetime of the carriers into all modes. The terms on the right-hand side of equation 2.62 represent, in order, electrical pumping, spontaneous emission, and stimulated emission, respectively. Non-radiative recombination has been absorbed by the η_i term.

Consider the case of steady-state immediately below threshold, in which stimulated emission is negligible. Then, equation 2.62 can be rearranged to find the threshold carrier density;

$$\frac{N_{th}}{\tau_{sp}} = \eta_i \frac{I_{th}}{q}. \tag{2.63}$$

Above threshold, the modal gain, and therefore carrier density, must "clamp" at this threshold value at which it exactly balances the optical losses (equation 2.14), otherwise the optical wave would grow without limit and lead to a non-physical solution. Physically, carrier density clamping happens because excess carriers above the threshold density will cause a brief increase in the photon density by extra stimulated emission. The increased photon density will in turn reduce the number of carriers through extra stimulated emission, leading to a damped oscillation and a return to the threshold value. This is the relaxation oscillation [2, p.697].

The carrier rate equation for the specific case of above-threshold operation can be found by combining equations 2.62 and 2.63 and clamping modal gain at its threshold value

$$\frac{dN}{dt} = \eta_i \frac{(I - I_{th})}{q} - v_g \Gamma_{act} g_{th} N_p. \tag{2.64}$$

Last, the steady state photon number can be found by setting the time derivative to zero and expressing the threshold gain in terms of the cavity Q using the threshold

condition (equation 2.14)

$$N_\mathrm{p} = \eta_\mathrm{i} \frac{(I - I_\mathrm{th})}{q} \frac{Q}{\omega}. \tag{2.65}$$

Equation 2.65 indicates two "knobs" for increasing the number of photons in the cavity: increasing the pump current and increasing the cavity Q. Because phase noise variance depends on the pump current, a fair noise comparison between two different lasers should be taken at the same pump current above threshold.

2.4.3 Spectral linewidth of the optical field

The spectral linewidth of the optical field is commonly used as a metric for the degree of phase coherence of a laser. The linewidth of a laser that is only subject to phase noise caused by spontaneous emission can be expressed in terms of the phase variance ($\langle \Delta\theta^2(T) \rangle$). Let the electric field of the laser be given by

$$E(t) = E_0 \exp[\mathrm{i}(\omega t + \theta(t))], \tag{2.66}$$

where E_0 is the field amplitude and $\theta(t)$ its phase, which is a function of time because it contains the spontaneous emission noise. Assume that the field amplitude is constant (i.e., not subject to amplitude noise). The autocorrelation of the laser field at a delay time T is

$$\langle E(t)E^*(t - T) \rangle = \langle E_0^2 \, \exp(\mathrm{i}\omega T) \exp[\mathrm{i}(\theta(t) - \theta(t - T))] \rangle. \tag{2.67}$$

Let the phase difference be defined as $\Delta\theta(T) \equiv \theta(t) - \theta(t - T)$. Taking the constant terms out of the average yields

$$\langle E(t)E^*(t - T) \rangle = E_0^2 \, \exp(\mathrm{i}\omega T) \, \langle \exp(\mathrm{i}\Delta\theta(T)) \rangle. \tag{2.68}$$

The term on the right is calculated directly as an expectation for the phase difference. The accumulated phase difference $\Delta\theta(T)$ is the result of many independent spontaneous emission events, so the probability distribution for $\Delta\theta(T)$ is Gaussian

with variance $\langle \Delta\theta^2(T) \rangle$ by the central limit theorem, and the calculation evaluates to [2, p.488; 8, p.198]

$$\langle \exp(\mathrm{i}\Delta\theta(T)) \rangle = \exp(- \langle \Delta\theta^2(T) \rangle /2). \tag{2.69}$$

The phase variance is given by equation 2.52, so the autocorrelation of the laser field is then given by

$$\langle E(t)E^*(t - T) \rangle = E_0^2 \ \exp(\mathrm{i}\omega T) \ \exp\left(-\frac{R_{\mathrm{sp}}}{4N_{\mathrm{p}}}|T|\right), \tag{2.70}$$

where the delay $|T|$ has been defined to always be positive without loss of generality. This autocorrelation and the field spectrum are Fourier transform pairs by the Wiener-Khintchine theorem [2, p.470]. The Fourier transform of the decaying exponential found in equation 2.70 is well-known to be a Lorentzian with linewidth [2, p.488; 8, p.200]

$$\Delta f = \frac{R_{\mathrm{sp}}}{4\pi N_{\mathrm{p}}} = \frac{\langle \Delta\theta^2(T) \rangle}{2\pi T}. \tag{2.71}$$

This expression for the linewidth is typically referred to as the "Schawlow-Townes" linewidth, after the first derivation [9].

2.4.4   Phase noise power spectral density

Phase noise due to spontaneous emission in lasers can also be measured as a power spectral density of the phase deviation $\Delta\theta$. In practice, the power spectral density can be used to find the noise inherent to spontaneous emission by clearly separating technical $1/f$ noise from the white spontaneous emission spectrum.

The phase variance can be written in terms of the frequency noise spectral density [8, p.197; 10]

$$\langle \Delta\theta^2(T) \rangle = 2\pi T^2 \int_{-\infty}^{\infty} S_f(f) \ \frac{\sin^2(\pi f T)}{(\pi f T)^2} \ \mathrm{d}f, \tag{2.72}$$

where the frequency noise power spectral density, $S_f(f)$, is two-sided and has units

here of Hz^2/Hz. If a white spectrum (constant in f) is assumed for $S_f(f)$, the integral can be evaluated as

$$\left\langle \Delta\theta^2(T) \right\rangle = (2\pi)^2 S_f T. \tag{2.73}$$

The linewidth is then related to the frequency noise power spectral density by following the process that starts with equation 2.70 with the replacement

$$\frac{R_{\mathrm{sp}}}{2N_{\mathrm{p}}} \to (2\pi)^2 S_f. \tag{2.74}$$

Therefore, the laser's spectral linewidth is related to its white frequency noise power spectral density by

$$\Delta f = 2\pi S_f. \tag{2.75}$$

In reality, the frequency noise power spectrum of a laser exhibits both white spontaneous emission noise and strong $1/f$ noise at low frequency offsets from the carrier [11–13]. The $1/f$ noise is likely technical in origin and may be due to temperature fluctuations, electrical interference, etc. Pure $1/f$ noise has a Gaussian spectral lineshape that would be convolved with the Lorentzian lineshape of the spontaneous emission in an attempted measurement of the laser's lineshape [13]. It is therefore difficult to measure the contribution of spontaneous emission to the linewidth of a laser in situations where the $1/f$ noise dominates the measurement of the overall lineshape function. Lasers operating at high pump powers [12] or lasers with little spontaneous emission are better characterized by measuring the frequency noise power spectral density. A "spontaneous emission linewidth" for these lasers is calculated by finding a white frequency power spectral density at high frequency offsets from the carrier, where $1/f$ noise does not affect the measurement, and using equation 2.75 to provide a single number that characterizes the spontaneous emission noise in the laser.

For applications in coherent communication, the $1/f$ noise is (somewhat) irrelevant as the only noise at frequencies faster than the symbol rate is integrated by the detector. In a differential phase measurement, only the phase excursion due to noise between two adjacent symbols affects the measurement, and in absolute phase mea-

surements, a phase-locked loop can be used at the receiver to track any slow phase deviations in the transmitting laser.

2.4.5 Linewidth enhancement factor

Besides directly injecting out-of-phase noise into the laser mode, spontaneous emission also affects the phase of the field through the linewidth enhancement factor [14].

A spontaneous emission event both emits a new photon and transitions an electron from the conduction band down to the valence band, instantly reducing the gain in the semiconductor. Gain is related to the imaginary component of the index of refraction (n_i), which is coupled to the real component (n_r) through the Kramers-Kronig relation [2, p.706]. The linewidth enhancement factor (α) is

$$\alpha \equiv -\frac{\mathrm{d}n_r/\mathrm{d}N}{\mathrm{d}n_i/\mathrm{d}N} = -\frac{4\pi}{\lambda}\frac{\mathrm{d}n_r/\mathrm{d}N}{\mathrm{d}g/\mathrm{d}N}, \qquad (2.76)$$

where N is the number of electrical carriers. Changes to n_r induced by changes in n_i cause the effective length of the cavity to change ($L_{\mathrm{eff}} = n_r\ L_{\mathrm{physical}}$), thus inducing frequency/phase shifts in the mode. The eventual effect of the index modulation is to contribute a factor α^2 to the phase noise of the mode. The linewidth enhancement factor is relevant to semiconductor gain media, but not atomic media, because the gain spectrum for a semiconductor is asymmetric in frequency, so at maximum gain $\mathrm{d}n_r/\mathrm{d}N$ is non-zero.

The total laser linewidth including the linewidth enhancement is

$$\Delta f = \frac{R_{\mathrm{sp}}}{2N_{\mathrm{p}}}\left(1 + \alpha^2\right). \qquad (2.77)$$

Typical linewidth enhancement factors for quantum well lasers are in the range of 2-5 [15]; therefore, this contribution to phase noise usually dominates in semiconductor lasers. However, the linewidth enhancement factor depends on many parameters. Most importantly, the denominator of equation 2.76 is the differential gain of the laser at threshold, which can be increased by operating closer to transparency. An approx-

imation to the differential gain can be calculated using the empirical relationship between gain and carrier density (equation 2.45),

$$\left.\frac{\mathrm{d}g}{\mathrm{d}N}\right|_{N_{\mathrm{th}}} \approx \frac{g_0}{N_{\mathrm{th}}}, \tag{2.78}$$

for operating points near transparency. The worst case for the linewidth enhancement factor would be at complete inversion, where the differential gain is zero and the linewidth enhancement factor blows up. Values of α of around 60 have been experimentally demonstrated in semiconductor lasers operating near complete inversion [16].

There are many strategies to reduce the linewidth enhancement factor. Most commonly, using quantum wells instead of bulk semiconductor increases the differential gain, thereby benefiting noise performance [6; 17; 18]. Increasing the number of quantum wells is similarly thought to decrease the linewidth enhancement factor through increased differential gain [19]; however, the population inversion factor (μ) increases, and accounting for the extra carriers in the surrounding regions due to the higher transparency increases absorption in multiple quantum well lasers. This leads to an optimum number of quantum wells for noise performance [20; 21]. Several experiments have shown that lasers made with fewer quantum wells have narrower linewidths [22; 23]. Operating the laser on the blue side of the gain peak reduces the numerator of equation 2.76 to the point where it could even become zero [19; 24–26]. Thin [19; 21; 27], deep [15] quantum wells are better. Either tensile [28] or compressive [29–31] strain applied to the wells reduces the linewidth enhancement factor. Introducing extra holes by p-type modulation doping near the wells also reduces the linewidth enhancement factor [18].

The physical shape of an index-guiding laser structure is not thought to affect the linewidth enhancement factor significantly because any relevant confinement factors will affect the numerator and denominator of equation 2.76 equally [32].

Based on this discussion of the linewidth enhancement factor, narrow-linewidth lasers should be designed to minimize the effect of the linewidth enhancement factor

by

1. Reducing optical loss far beyond that in traditional semiconductor lasers in order to operate near transparency

2. Using a grating to set the operating wavelength to the blue side of the gain peak

3. Using compressively strained quantum wells

2.4.6 Total linewidth

The Schawlow-Townes linewidth (equation 2.71) can be expressed in terms of experimental parameters by substituting the values found for the spontaneous emission rate (equation 2.61) and photon number (equation 2.65). The linewidth, including the effect of the linewidth enhancement factor, is then

$$\Delta f = \frac{1}{4\pi}\frac{\omega^2}{Q^2}\frac{q}{I - I_{\text{th}}}\frac{\mu}{\eta_{\text{i}}}(1 + \alpha^2). \tag{2.79}$$

This expression shows that the laser linewidth due to spontaneous emission has a $1/Q^2$ dependence, though the effect of the population inversion factor (μ) may reduce the overall improvement in Q slightly. Increasing Q benefits the spontaneous emission rate into the laser mode by reducing the number of excited carriers needed to reach threshold and also benefits photon storage by reducing optical losses, leading to the strong dependence of linewidth on Q.

Increasing the pump current above threshold also would narrow linewidths by increasing the stimulated photon generation rate and, therefore, the number of photons stored in the cavity. To make fair comparisons, measured linewidths should be accompanied by the value of $(I - I_{\text{th}})$ at which the measurement was taken.

Chapter 3

Phase noise in hybrid Si/III-V lasers

This chapter presents a theory of noise in semiconductor lasers in which the laser cavity is composed of two different materials with very different optical absorption coefficients, like silicon and highly-doped III-V. Two important transformations are considered, which have different effects on noise in the cavity

Replacing III-V with silicon: Overall losses in a semiconductor laser can be reduced by replacing optically lossy III-V material in the laser cavity with very low-loss silicon. The confinement factor of the mode in the lossy III-V ($\Gamma_{\text{III-V}}$) becomes the metric for determining laser performance. Replacing III-V with silicon has the following effects:

1. The total quality factor (Q) of the hybrid laser cavity increases, scaling as $\Gamma_{\text{III-V}}^{-1}$ (equation 3.4).

2. The threshold modal gain of the hybrid laser decreases, scaling as $\Gamma_{\text{III-V}}$ (equation 3.5).

3. The linewidth of the hybrid laser decreases, scaling as $\mu\Gamma_{\text{III-V}}^2$. This scaling factor is between $\Gamma_{\text{III-V}}$ and $\Gamma_{\text{III-V}}^2$, depending on the threshold carrier density of the original III-V only laser (equation 3.15).

Modal engineering: The shape of the mode can be engineered to remove modal energy from the III-V. Under this transformation, both modal gain and III-

V absorption losses are reduced by the same factor. In the limit that III-V absorption dominates the total optical losses, modal engineering has the following effects:

1. The total Q of the hybrid laser increases, scaling as $\Gamma_{\text{III-V}}^{-1}$ (equation 3.24).

2. The threshold modal gain of the hybrid laser stays constant with $\Gamma_{\text{III-V}}$, as long as absorption loss in III-V limits Q (equation 3.26).

3. The linewidth of a hybrid laser decreases as $\Gamma_{\text{III-V}}^2$, as long as absorption loss in III-V limits Q (equation 3.32).

Properly executed modal engineering always yields smaller linewidths than replacing III-V with silicon.

3.1 The advantages of hybrid Si/III-V

The Q^{-2} dependence of the Schawlow-Townes linewidth is compelling as a "knob" by which relatively small changes in cavity design may yield great improvements to laser linewidths.

3.1.1 Limitations of traditional semiconductor lasers

Traditional semiconductor lasers have been limited in Q for two reasons: the intrinsic optical absorption in the highly-doped III-V layers that are necessary for efficient electrical performance, and the relatively poor fabrication abilities in III-V when compared to silicon. Table 3.1 presents a short review of published high-Q III-V resonators.

Loss coefficients in III-V cavities including both scattering (from poor fabrication) and absorption (intrinsic to the material) usually are on the order of 10 to $25\,\text{cm}^{-1}$ [36–42]. By shifting the mode away from the active region and etched surfaces, III-V lasers have been made with estimated loss coefficients of 0.5 to $1\,\text{cm}^{-1}$ [43; 44].

The traditional design of semiconductor lasers is therefore constrained by the need to make a compromise between materials with favorable electronic properties (e.g.,

Q	III-V resonator description
1M	No highly-doped active regions. Ring resonators have a very large radius of 13 mm [33].
100k	Ring resonators have 200 μm radius [34].
200k	Ring resonators similar to the 100k result. Here, losses are compensated by including a gain region [35].

Table 3.1: Published III-V high-Q resonators.

low series resistance) for efficient photon generation and materials with favorable optical properties (e.g., low absorption) for photon storage. For example, an ideal active material must have both a smaller electronic bandgap and a larger refractive index compared to the surrounding material in order to confine excited carriers and guided photons to the same region where they can stimulate the emission of new photons efficiently. In addition, the material near the active region must be heavily doped to form efficient p-n junctions for injecting carriers into the active region as well as forming low-resistance electrical contacts to the device. Unfortunately, the heavily doped III-V material causes significant optical absorption, creating a tradeoff between photon generation and storage. Last, all of the materials must have similar lattice constants so they can be grown together on the same wafer. These constraints have restricted semiconductor laser designs to using only a few materials, like the well-developed InGaAsP and AlGaAs systems.

The introduction of quantum-confined structures, such as quantum wells and quantum dots [6], to laser design provided the first step toward de-coupling electronic and optical properties of semiconductor lasers. The use of quantum wells allows the electronic bandgap to be defined by varying the thickness of semiconductor layers during growth instead of being limited to the use of the bulk crystal bandgap. Although these quantum-confined structures allow more flexibility in the design of the electronic half of semiconductor lasers, they don't reduce the need for heavy doping and thus provide no benefit to the equally-important need to store photons.

The previously-published, lowest-noise semiconductor lasers, to my knowledge, are found in table 3.2.

Linewidth	Description
3.6 kHz	III-V distributed phase shift DFB laser. This laser was tested in vacuum with no temperature controller [45].
6 kHz	External-cavity laser, with a large optical mode that has a mode engineered to avoid absorption in the highly-doped III-V regions [46]
64 kHz	III-V laser with the mode far from the etched sidewalls, using an integrated amplifier so the laser can reach high power without linewidth rebroadening due to spatial hole burning [47]
160 kHz	Basic III-V DFB laser [48]
300 kHz	III-V laser in which the mode is engineered to avoid absorption in the highly-doped III-V regions [49]

Table 3.2: Smallest published linewidths of existing semiconductor lasers (to my knowledge).

3.1.2 Silicon photonics

Research on high-quality optical components has been most successful on the silicon-on-insulator (SOI) platform. Silicon has very low optical absorption, with high-resistivity silicon having an absorption Q on the order of 100M; therefore, the total Q of a silicon resonator is determined mostly by fabrication imperfections [50].

Photonic device fabrication on silicon is very advanced because of the investment in technology provided by the integrated circuit industry. The high index contrast between silicon and the easily-grown silicon dioxide or air make waveguiding simple and nanoscale optical resonators possible. Silicon waveguides can be made using industry-standard lithography equipment with loss coefficients of $0.06\,\mathrm{cm}^{-1}$ (including material absorption and fabrication-induced scattering) [51; 52]. Waveguides with very smooth sidewalls can be formed by oxidizing silicon, a technique unavailable in III-V, in addition to or instead of plasma etching, leading to similar loss coefficients of 0.07 to $0.18\,\mathrm{cm}^{-1}$ [53–56]. These fabrication-limited losses are an order of magnitude smaller than the best III-V waveguides mentioned in the previous section and two orders of magnitude better than the absorption losses in highly-doped active III-V.

Simulated silicon nanocavity designs possess Q exceeding 10M [57], so the demonstrated Q of these cavities can be expected to increase even further with new advances

in fabrication technology. Resonators with experimentally-found Q values higher than 1M Q are regularly demonstrated today. In fact, absorption from water vapor adsorbed onto the silicon surface is now suspected to be limiting Q values, and a nano-scale resonator with Q of 9M has been achieved by eliminating ambient humidity [58]. Clearly, silicon has the potential to form laser cavities with much higher Q than III-V cavities, and these lasers would exhibit narrower linewidths according to Q^{-2}.

Silicon is not the perfect material, however. It has an indirect bandgap and therefore does not emit light efficiently. Years of research into direct-bandgap III-V materials, on the other hand, has yielded very efficient photon generators.

3.1.3 The hybrid Si/III-V platform

Heterogeneous integration of silicon with III-V combines the optical advantages of silicon with the electrical advantages of III-V in one platform, circumventing the traditional compromises between photon generation and photon storage. Integrating silicon with III-V via wafer bonding has become very common in recent years [59–64], making this technique an attractive option for a low-noise semiconductor laser.

The process of changing a semiconductor laser from a III-V-only cavity to a hybrid Si/III-V cavity involves two conceptual transformations: (1) replacing excess III-V with low-loss silicon and (2) modal engineering to shift the mode away from the lossy III-V. Both transformations have the goal of storing as much modal energy in silicon as is possible, but they lead to different results. It is important to consider both to minimize phase noise.

3.2 Replacing III-V with silicon

The first of two useful transformations for converting a III-V-only cavity into a hybrid Si/III-V cavity is to replace excess III-V with low-loss silicon. Figure 3.1 shows a cartoon version of this transformation. Because the index of silicon is similar to the index of the relevant III-V materials, this replacement can be made without

efficient photon generation
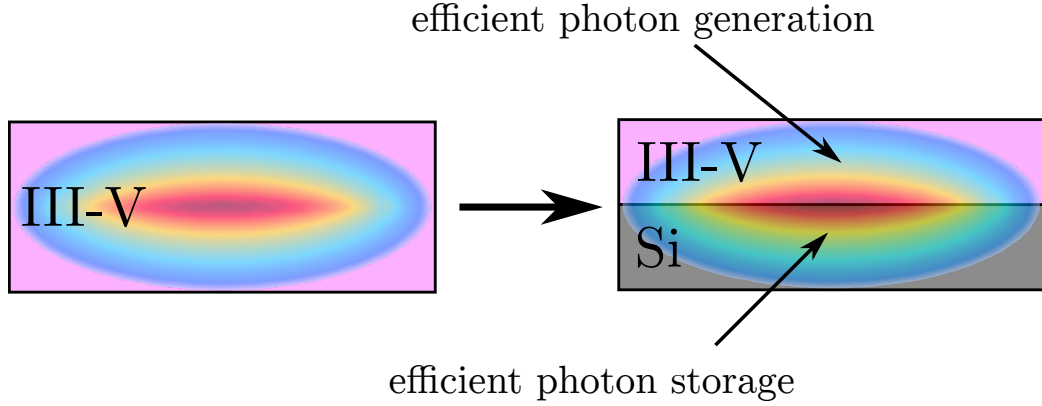

efficient photon storage

Figure 3.1: Replacing lossy III-V with low-loss silicon combines the advantages of efficient photon generation in III-V with low-loss photon storage in silicon.

significantly affecting the properties of the mode. Thus, the laser design can take advantage of the properties of silicon to the extent that silicon replaces III-V, with the goal of replacing as much as possible.

3.2.1 The quality factor of the hybrid cavity

The total Q of the hybrid Si/III-V cavity (Q_{hybrid}) can be broken down into its constituent loss components by equation 2.13. Material absorption is likely to limit the total Q of a well-designed cavity, so it may be singled out:

$$\frac{1}{Q_{\text{hybrid}}} = \frac{1}{Q_{\text{abs}}} + \frac{1}{Q_{\text{other}}}, \tag{3.1}$$

where Q_{abs} represents the quality factor due to material absorption only and Q_{other} represents all other sources of loss (see section A.3).

In a hybrid Si/III-V cavity, the fraction of modal energy located in the absorbing III-V is given by its confinement factor in III-V ($\Gamma_{\text{III-V}}$, equation 2.5). The confinement factor in silicon, which makes up the rest of the cavity, is then $\Gamma_{\text{Si}} = 1 - \Gamma_{\text{III-V}}$. Using these confinement factors, Q_{abs} can be broken down using equation 2.6,

$$\frac{1}{Q_{\text{abs}}} = \frac{\Gamma_{\text{III-V}}}{Q_{\text{III-V}}} + \frac{1 - \Gamma_{\text{III-V}}}{Q_{\text{Si}}}, \tag{3.2}$$

where $Q_{\text{III-V}}$ is the quality factor derived from the III-V material absorption only (about 10k) and Q_{Si} is the quality factor derived from silicon absorption only (as high as 100M).

Inserting equation 3.2 into 3.1 gives

$$\frac{1}{Q_{\text{hybrid}}} = \frac{\Gamma_{\text{III-V}}}{Q_{\text{III-V}}} + \frac{1 - \Gamma_{\text{III-V}}}{Q_{\text{Si}}} + \frac{1}{Q_{\text{passive}}}. \tag{3.3}$$

Material absorption in silicon is extremely low and will probably never limit Q_{hybrid}. Other components of loss, like external coupling and scattering are much larger. Therefore, the Q_{Si} term can be grouped with the "other" sources of loss. This new grouping is given the designation "passive" because it is the Q of the hybrid resonator in the case where $\Gamma_{\text{III-V}}$ is zero or negligibly small, and therefore, is the Q of a passive silicon resonator with no III-V attached. The total hybrid Q is then

$$\frac{1}{Q_{\text{hybrid}}} \approx \frac{\Gamma_{\text{III-V}}}{Q_{\text{III-V}}} + \frac{1}{Q_{\text{passive}}}. \tag{3.4}$$

In this equation, the numerator of the Q_{passive} term is taken to be 1 instead of $1 - \Gamma_{\text{III-V}}$ to account for the sources of loss other than III-V absorption in the case of a III-V-only laser ($\Gamma_{\text{III-V}} = 1$). Narrow-linewidth Si/III-V lasers will be made with very small $\Gamma_{\text{III-V}}$, making the choice of numerator inconsequential for the lasers described in this thesis.

Numerically simulating the optical mode gives $\Gamma_{\text{III-V}}$ and measuring the loaded Q of fabricated silicon-only resonators gives Q_{passive}. With values for these two parameters, Q_{hybrid} can be estimated easily.

This breakdown for Q_{hybrid} defines two regimes: one in which optical absorption in III-V dominates the total Q and one in which other factors, like scattering from rough surfaces, dominate. Replacing silicon with III-V decreases $\Gamma_{\text{III-V}}$ and therefore increases Q_{hybrid}, but only while the other sources of loss are negligible.

Figure 3.2 shows the benefit to Q_{hybrid} of replacing III-V with silicon for various values of Q_{passive}. Clearly, lasers with the highest Q_{hybrid} will have most of their III-V
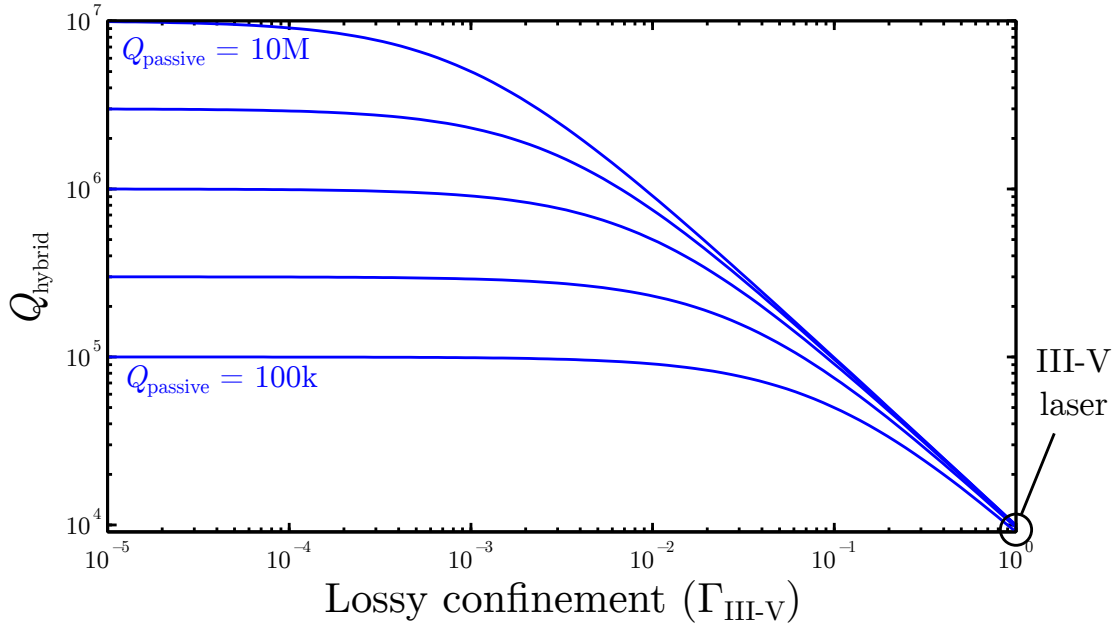
Figure 3.2: Total Q of the hybrid cavity under the III-V-to-silicon replacement. Various values of Q_{passive} are shown. The best Q_{hybrid} is for a cavity with a very high Q_{passive} and minimal $\Gamma_{\text{III-V}}$. Marked on the plot is the total Q of a III-V-only laser. Assumption: $Q_{\text{III-V}} = 10\text{k}$.

replaced with silicon and will feature very high-Q passive resonators.

3.2.2 Threshold gain

The threshold gain of the hybrid laser can be found by substituting Q_{hybrid} (equation 3.4) into the threshold gain formula (equation 2.14);

$$\Gamma_{\text{act}} g_{\text{th}} = \frac{\omega}{v_{\text{g}}} \left(\frac{\Gamma_{\text{III-V}}}{Q_{\text{III-V}}} + \frac{1}{Q_{\text{passive}}} \right). \tag{3.5}$$

As silicon replaces III-V, the confinement factor in the lossy region ($\Gamma_{\text{III-V}}$) decreases. However, the refractive indices of the two materials are similar, so the mode shape remains basically the same. Therefore, the confinement factor in the active region (Γ_{act}) stays approximately constant under this transformation.

In the regime in which III-V absorption dominates Q_{hybrid}, replacing III-V with
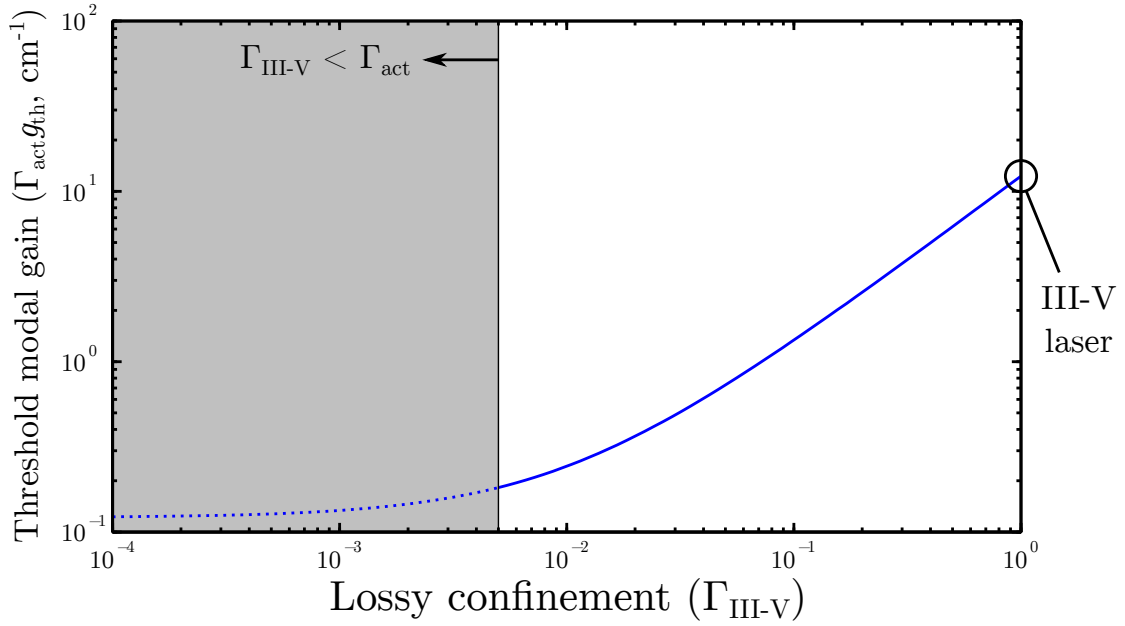
Figure 3.3: Threshold modal gain under the III-V-to-silicon replacement. The amount of III-V replaced by silicon is represented by the confinement factor in III-V, $\Gamma_{\text{III-V}}$. The shaded area represents the non-physical situation in which $\Gamma_{\text{III-V}} < \Gamma_{\text{act}}$. Assumptions: $Q_{\text{passive}} = 1\text{M}$, $Q_{\text{III-V}} = 10\text{k}$.

silicon decreases the threshold modal gain in hybrid Si/III-V lasers;

$$\Gamma_{\text{act}} g_{\text{th}} \approx \frac{\omega}{v_{\text{g}}} \frac{\Gamma_{\text{III-V}}}{Q_{\text{III-V}}} \tag{3.6}$$

$$\propto \Gamma_{\text{III-V}}.$$

However, if Q_{passive} dominates Q_{hybrid}, replacing III-V with silicon yields no further benefit to the threshold modal gain because Q_{hybrid} is independent of $\Gamma_{\text{III-V}}$ in this regime. The value of $\Gamma_{\text{III-V}}$ at which the two terms comprising Q_{hybrid} are equal is termed the "critical confinement" (Γ_{crit}).

Figure 3.3 shows the modal gain required to reach threshold for a hybrid Si/III-V laser undergoing the III-V-to-silicon replacement for typical parameter values.

3.2.3 Population inversion factor

It's important to note that reduced threshold modal gain that results from removing optical energy from the active material does not necessarily mean reduced threshold carrier densities or threshold currents. The need to pump the semiconductor to transparency creates a minimum carrier density and current at threshold. The population inversion factor (μ) accounts for this minimum carrier density in the laser, applying a "penalty" for incomplete inversion. It is important to calculate the effect of the population inversion factor on the spontaneous emission rate (R_{sp}). The spontaneous emission factor is defined in equation 2.60 to be

$$\mu \equiv \frac{f_2(1 - f_1)}{f_2 - f_1}, \tag{3.7}$$

where f_i is the probability of electronic state $|i\rangle$ being occupied by a carrier, according to the Fermi distribution (equation 2.56). The Fermi probabilities are related to the stimulated emission rate by combining equations 2.53, and 2.54 for the individual upward and downward stimulated transition rates, and 2.59 for the net downward stimulated rate:

$$R_{st} = \rho_r V_{act} W_{st}(f_2 - f_1). \tag{3.8}$$

In order to have net positive optical gain, the stimulated downwards transition rate must be higher than the stimulated upwards rate (i.e., absorption), or $f_2 > f_1$. Relating the stimulated emission rate to the optical gain via equation 2.9,

$$f_2 - f_1 = \Gamma_{act} g_{th} \frac{v_g}{\rho_r V_{act}} \frac{N_p}{W_{st}} \tag{3.9}$$

$$\propto \Gamma_{act} g_{th}.$$

This is the denominator of the population inversion factor. The stimulated transition rate (W_{st}) is proportional to the number of photons in the mode (equation 2.26), so the N_p/W_{st} term on the right-hand side of this equation is independent of the silicon-replacing-III-V transformation.

Equation 3.9 gives the denominator of the population inversion factor for any laser. Finding a general expression for the population inversion factor is difficult because the Fermi levels depend on material parameters; however, the marginal change in μ for any laser can be found near complete inversion and near transparency.

Near complete inversion

The marginal change in μ for small changes in carrier density, Δf_2 and Δf_1, is

$$\mu \sim \frac{(f_2 - \Delta f_2)\left(1 - (f_1 + \Delta f_1)\right)}{(f_2 - \Delta f_2) - (f_1 + \Delta f_1)}. \tag{3.10}$$

At complete inversion, $f_2 = 1$ and $f_1 = 0$. Under these conditions, $\mu \sim 1$ and does not change with carrier density, assuming $\Delta f_1, \Delta f_2 \ll 1$. Carrier density changes monotonically with threshold gain, which depends on $\Gamma_{\text{III-V}}$ according to equation 3.5, so μ is independent of $\Gamma_{\text{III-V}}$ near complete inversion.

Near transparency

Near transparency, $f_1 \approx f_2$. Reducing modal gain while requiring gain to remain positive means

$$f_2 - \Delta f_2 > f_1 + \Delta f_1. \tag{3.11}$$

Near transparency, $f_2 - \Delta f_2 \approx f_2$ and $f_1 + \Delta f_1 \approx f_1$, so the numerator of the population inversion factor should be independent of a reduction in modal gain. The denominator of the population inversion factor, on the other hand, is the difference of two similar values and is linear in changes to threshold gain, as seen in equation 3.9. Therefore, the marginal change to the population inversion factor near transparency is dominated by the denominator. Express threshold modal gain in terms of Q (equation 2.14) and insert Q_{hybrid} of a Si/III-V laser (equation 3.4);

$$\mu \sim \left(\frac{\Gamma_{\text{III-V}}}{Q_{\text{III-V}}} + \frac{1}{Q_{\text{passive}}}\right)^{-1}. \tag{3.12}$$

Therefore, near transparency, the population inversion factor is very sensitive to changes in $\Gamma_{\text{III-V}}$ in the case that Q_{hybrid} is dominated by absorption in III-V.

3.2.4 Spontaneous emission rate into the laser mode

The spontaneous emission rate into the mode is given by equation 2.61, with Q_{hybrid} for the replacement transformation representing the total Q of the cavity

$$R_{\text{sp}} = \frac{\omega\mu}{Q_{\text{hybrid}}} = \omega\mu \left(\frac{\Gamma_{\text{III-V}}}{Q_{\text{III-V}}} + \frac{1}{Q_{\text{passive}}} \right). \tag{3.13}$$

The discussion of the population inversion factor in the previous section helps to understand how R_{sp} changes as silicon replaces III-V.

For a III-V laser near complete inversion, Q_{hybrid} scales with $\Gamma_{\text{III-V}}^{-1}$ and μ is independent of $\Gamma_{\text{III-V}}$. Therefore, R_{sp} scales with $\Gamma_{\text{III-V}}$.

However, for a III-V laser which is already operating near transparency, Q_{hybrid} scales with $\Gamma_{\text{III-V}}^{-1}$ and μ scales with $\Gamma_{\text{III-V}}$. The change in μ cancels the change in Q_{hybrid} and the spontaneous emission rate into the mode is independent of $\Gamma_{\text{III-V}}$.

Low-noise lasers should operate near transparency due to the favorable linewidth enhancement factor (see section 2.4.5). The unfortunate conclusion is that there is not any marginal benefit to the spontaneous emission rate into the mode caused by replacing lossy III-V with low-loss silicon if the original III-V-only laser were already operating near transparency.

Even though there may be no marginal benefit to R_{sp}, if the original III-V-only laser being considered were operating far from transparency, R_{sp} will be reduced by replacing III-V with silicon. The benefit will be sub-linear in $\Gamma_{\text{III-V}}$.

The phenomenological description

Equation 2.49 provides a phenomenological way to understand the spontaneous emission rate in hybrid Si/III-V lasers under the III-V-to-silicon transformation. The three terms considered in the phenomenological equation are the number of excited carriers at threshold (N_{th}), the spontaneous emission rate of each individual carrier
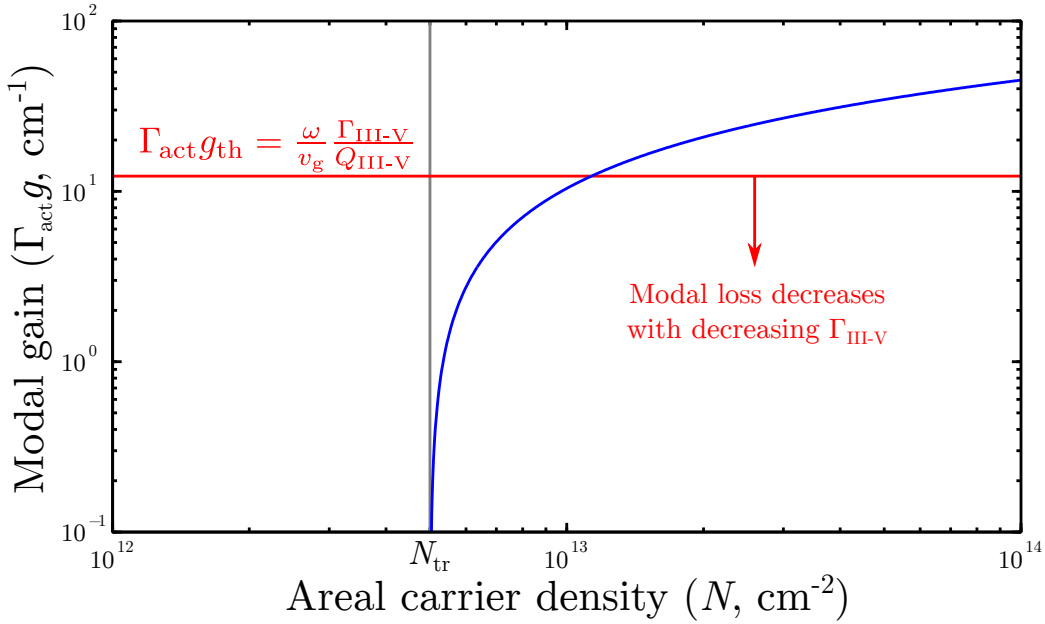
Figure 3.4: Modal gain in a quantum well laser. The horizontal line represents the loss in a III-V-only laser. The intersection of the gain curve with the horizontal loss line gives the threshold carrier density in such a laser. As low-loss silicon replaces lossy III-V, this line will slide downward, meaning that fewer excited carriers are needed to reach threshold in a hybrid Si/III-V laser compared to a III-V only laser. Assumptions: $N_{\text{th}} = 5 \times 10^{12} \, \text{cm}^{-2}$, $g_0 = 3 \times 10^3 \, \text{cm}^{-1}$, $\lambda = 1550 \, \text{nm}$, $n_{\text{g}} = 3$, $Q_{\text{III-V}} = 10\text{k}$, $\Gamma_{\text{act}} = 0.5\%$.

into all modes (τ_{sp}^{-1}), and the fraction of total spontaneous emission that enters the lasing mode (β_{sp}).

The number of excited carriers needed to reach threshold decreases with decreasing threshold modal gain (figure 3.3). However, the transparency carrier density sets a minimum for the number of excited carriers at threshold, meaning that there will be diminishing returns to linewidth from decreasing modal gain as the number of carriers approaches transparency. Figure 3.4 shows the modal gain vs. carrier density curve for a quantum well laser derived from the empirical equation 2.45. Figure 3.5 shows this relationship in terms of $\Gamma_{\text{III-V}}$, demonstrating the diminishing returns from reducing losses as the threshold carrier density approaches transparency. This phenomenological approach provides a physical description for the effect of the population inversion factor, μ, which was found to cancel the effect of Q_{hybrid} in hybrid Si/III-V lasers near transparency.
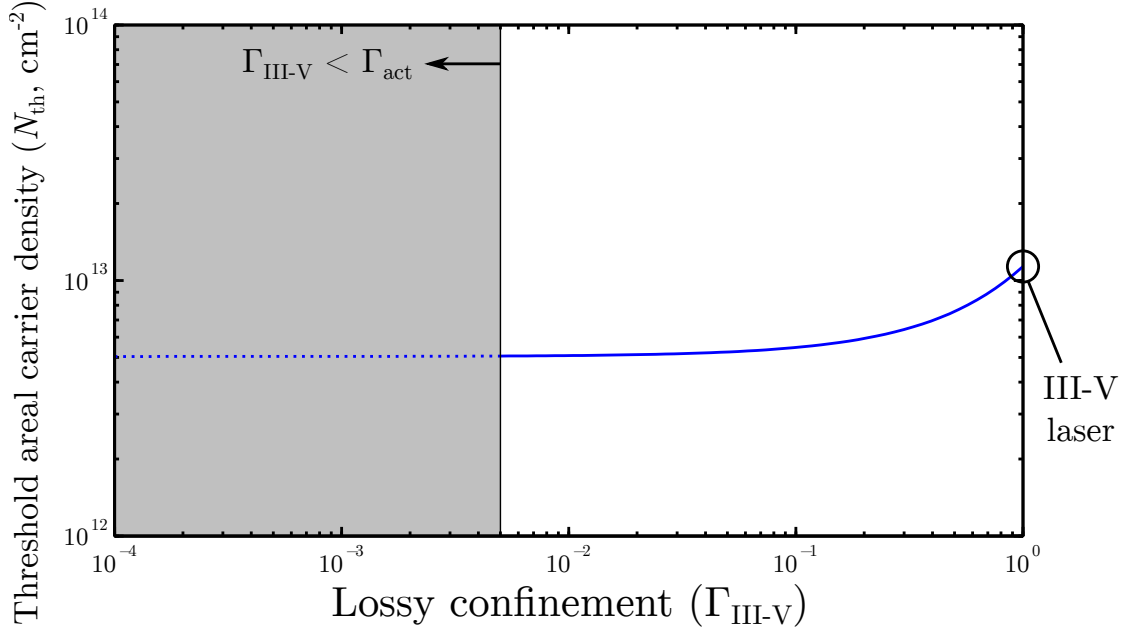
Figure 3.5: Threshold carrier density in a hybrid Si/III-V laser in which some lossy III-V has been replaced with low-loss silicon, calculated using the empirical equation 2.45. Assumptions: $N_{\text{th}} = 5 \times 10^{12} \, \text{cm}^{-2}$, $g_0 = 3 \times 10^3 \, \text{cm}^{-1}$, $\lambda = 1550 \, \text{nm}$, $n_{\text{g}} = 3$, $Q_{\text{III-V}} = 10\text{k}$, $\Gamma_{\text{act}} = 0.5\%$.

The other two terms in the phenomenological description are expected to stay constant as silicon replaces III-V. The spontaneous emission rate of a single carrier into all modes, τ_{sp}^{-1}, is dominated by the non-lasing modes that interact with the carriers. The number of these modes depends on the volume of the laser cavity (equation 2.36), which does not change under the III-V-to-silicon replacement. Similarly, the fraction of spontaneous emission that enters the laser mode (β_{sp}) was shown to scale with the intensity of the mode at the active region (equation 2.44). Both the shape of the laser mode and the other radiation modes are expected to be independent of the III-V-to-silicon replacement; therefore, Fermi's Golden Rule will give the same result for β_{sp} in this case as for a III-V-only laser.

The spontaneous emission rate into the lasing mode of a hybrid Si/III-V laser decreases as more low-loss silicon replaces lossy III-V because the number of excited carriers needed to reach threshold decreases under this replacement transformation. However, the lower bound of transparency on the number of excited carriers means that R_{sp} will be independent of $\Gamma_{\text{III-V}}$ for marginal replacement near transparency.

3.2.5 Photon storage

Although the spontaneous emission rate into the mode may be independent of $\Gamma_{\text{III-V}}$ in some cases, there is still a benefit to photon storage from replacing III-V with silicon. Equation 2.65 for the number of stored photons was derived without any assumptions about the cavity design or the operating point. It states that the number of stored photons (N_{p}) scales with Q_{hybrid}

$$N_{\text{p}} = \frac{\eta_{\text{i}}}{\omega} \frac{(I - I_{\text{th}})}{q} \left(\frac{\Gamma_{\text{III-V}}}{Q_{\text{III-V}}} + \frac{1}{Q_{\text{passive}}} \right)^{-1}. \tag{3.14}$$

The two regimes for this equation are the same as for Q_{hybrid}. For $\Gamma_{\text{III-V}} > \Gamma_{\text{crit}}$, N_{p} scales as $\Gamma_{\text{III-V}}$. For $\Gamma_{\text{III-V}} < \Gamma_{\text{crit}}$, N_{p} is independent of the replacement transformation. The number of stored photons scales in exactly the same way as Q_{hybrid}, which was plotted in figure 3.10.

3.2.6 Linewidth

The linewidth of a hybrid Si/III-V laser under the III-V-to-silicon replacement can be found by combining the calculated spontaneous emission rate (equation 3.13) and photon storage (equation 3.14), similar to the way equation 2.79 was derived.

$$\Delta f = \frac{\omega^2}{4\pi} \left(\frac{\Gamma_{\text{III-V}}}{Q_{\text{III-V}}} + \frac{1}{Q_{\text{passive}}} \right)^2 \frac{q}{I - I_{\text{th}}} \frac{\mu}{\eta_{\text{i}}} (1 + \alpha^2). \tag{3.15}$$

Equation 3.15 has two regimes, one in which absorption in III-V dominates Q_{hybrid} and the other in which Q_{passive} dominates. It is difficult to replace virtually all of the lossy III-V because a certain amount is needed for efficient electrical operation. Assuming III-V absorption continues to dominate Q_{hybrid} after replacement, the total linewidth of these lasers is

$$\Delta f \approx \frac{\omega^2}{4\pi} \frac{\Gamma_{\text{III-V}}^2}{Q_{\text{III-V}}^2} \frac{q}{I - I_{\text{th}}} \frac{\mu}{\eta_{\text{i}}} (1 + \alpha^2) \tag{3.16}$$

$$\propto \mu \Gamma_{\text{III-V}}^2.$$

This is an important result! Replacing III-V with silicon decreases the linewidth of the laser by a factor between $\Gamma_{\text{III-V}}$ and $\Gamma_{\text{III-V}}^2$ (depending on how μ changes), which can be controlled in the laser design by the fraction of lossy III-V that is replaced by low-loss silicon. Note that this result assumes that all other sources of optical loss besides absorption in III-V are sufficiently small.

The phenomenological description

Once again, the phenomenological approach to calculating the spontaneous emission rate into the mode provides a physical description of the hybrid Si/III-V laser's linewidth. The two terms expected to affect the linewidth calculation are the number of excited carriers at threshold ($R_{\text{sp}} \propto N_{\text{th}}$) and the number of photons stored in the cavity ($N_{\text{p}} \propto Q_{\text{hybrid}}^{-1}$). These two terms provide a linewidth metric by which hybrid Si/III-V lasers can be compared relative to III-V-only lasers as low-loss silicon replaces III-V;

$$\text{relative linewidth} \equiv \frac{N_{\text{th}}}{Q_{\text{hybrid}}}. \tag{3.17}$$

Figure 3.6 shows this relative linewidth calculated using the empirical equation 2.45 for N_{th} and the exact equation 3.4 for Q_{hybrid}. Noise can be reduced as much as $\Gamma_{\text{III-V}}^2$ relative to a III-V-only laser, with one factor of $\Gamma_{\text{III-V}}$ each coming from improvements to spontaneous photon generation and photon storage. However, the effects of both of these improvements saturate as there are limits to the replacement transformation.

3.2.7 Limits of the replacement transformation

The practical limit on how much III-V can be replaced by silicon is set by the need to make the III-V electrically efficient. Research into III-V semiconductors over many decades has resulted in standard III-V materials systems that have layers which cannot be replaced with silicon without suffering consequences on the electrical side of the design.

In addition to the practical limit, there are two points at which reducing $\Gamma_{\text{III-V}}$ results in diminishing returns to narrower linewidths:
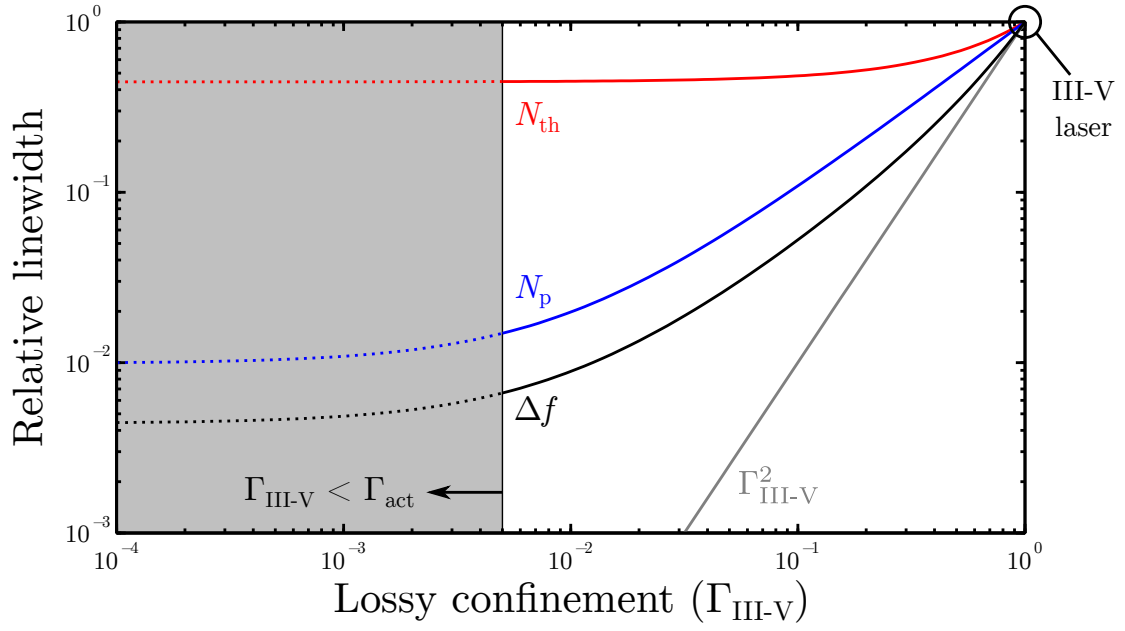
Figure 3.6: The linewidth of a hybrid Si/III-V laser under the III-V-to-silicon replacement transformation. The two components expected to change under this replacement are plotted along with the overall linewidth, with all parameters normalized to the values found in a III-V-only laser. The $\Gamma^2_{\text{III-V}}$ line is plotted to show the lower limit on linewidth. Assumptions: $Q_{\text{passive}} = 1\text{M}$, $Q_{\text{III-V}} = 10\text{k}$, $\lambda = 1550\,\text{nm}$, $n_{\text{g}} = 3$, $\Gamma_{\text{act}} = 0.5\%$, $N_{\text{th}} = 5 \times 10^{12}\,\text{cm}^{-2}$.

1. The spontaneous emission rate into the mode is limited by the need to pump the active medium to transparency. For low-loss hybrid Si/III-V lasers already operating near transparency, further loss reduction will not reduce the spontaneous emission rate into the mode appreciably. Mathematically, this is accounted for by the population inversion factor (μ, equation 3.12).

2. Photon storage is limited by the attainable values of Q_{passive}. If sources of loss other than optical absorption in III-V dominate the total losses, reducing optical absorption will not reduce the total losses (equation 3.4). Note that this will also affect the spontaneous emission rate into the mode if it has not already saturated at transparency.

These saturation effects can be seen in the noise reduction plot that was shown in figure 3.6.

3.3   Modal engineering

Modal engineering is a second transformation that can be used in addition to replacing III-V with silicon. Modal engineering changes the shape of the laser mode by engineering waveguide geometry and can be used to make the mode weaker in III-V.

The results from quantum mechanics derived in section 2.2 show that stimulated emission, spontaneous emission, and loss in regions immediately surrounding the active region are proportional to the normalized electric field intensity at the active region. Making the mode weaker at the active region will therefore decrease spontaneous emission into the lasing mode and modal gain, which would cause thresholds to increase immensely in an ordinary laser. However, in a hybrid Si/III-V laser modal engineering will shift modal energy towards silicon, where it can be stored with very low losses. In the case that optical absorption in III-V dominates the total losses, modal engineering will reduce modal gain and losses by the same factor, keeping threshold constant.

This section describes the modal engineering transformation and shows that it

reduced spontaneous photon generation
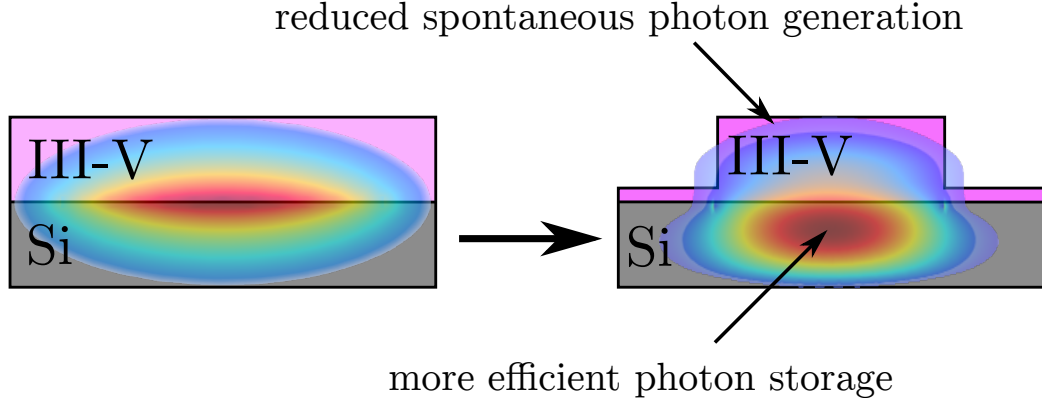

more efficient photon storage

Figure 3.7: Engineering the mode to shift more of its energy into the low-loss silicon reduces spontaneous photon generation and increases photon storage.

has very different effects on the various laser properties compared to the replacement transformation. The results derived from the modal engineering transformation will show that the naïve approach of reducing losses relative to gain (or, equivalently, increasing gain relative to loss) used in the replacement transformation and in most laser design is sub-optimal. Instead, the best strategy is, counter-intuitively, to reduce the modal gain provided by the active material as long as losses can be reduced by the same factor.

Figure 3.7 shows a cartoon example of modal engineering.

3.3.1 Supermode model

Modal engineering could greatly benefit from a "knob" to tune the strength of the electric field in the III-V region of the hybrid Si/III-V laser cavity. Typical III-V active material forms a waveguide in order to confine photons to the same region as the excited electrons. Silicon that has replaced some of the lossy III-V forms a second waveguide that is coupled to the III-V waveguide.

The eigenmodes of the coupled waveguide system can be viewed as linear combinations of the individual waveguide modes called "supermodes" [65, p.526]. Some of the early research on hybrid Si/III-V lasers in this group concentrated on using supermodes to *increase* the modal confinement in III-V to increase modal gain, reducing threshold [66–70]. Now, the goal has changed to *reducing* the modal confinement in
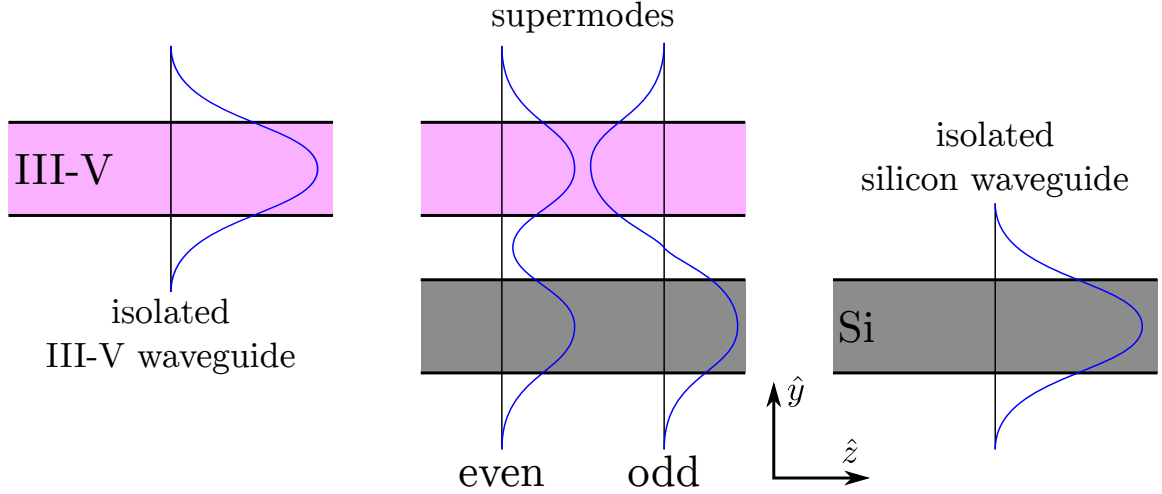
Figure 3.8: Supermodes are formed by linear combinations of the individual waveguide modes, producing odd and even modes. These two supermodes have equal weight.

III-V to reduce the spontaneous emission rate into the mode.

Figure 3.8 shows a cartoon version of a pair of slab waveguides arrayed in the $\hat{y}$ direction, with the mode propagating in the $\hat{z}$ direction. The supermode can be represented as a linear combination of the individual waveguide modes [65, p.527],

$$E(y, z) = A_{\text{III-V}} E_{\text{III-V}}(y) \exp(-\mathrm{i}\beta_{\text{III-V}} z) + A_{\text{Si}} E_{\text{Si}}(y) \exp(-\mathrm{i}\beta_{\text{Si}} z), \quad (3.18)$$

where $E_i(y)$ is the transverse electric field of the individual (non-coupled) waveguide mode in material i, A_i is a weighting factor applied to the individual modes in material i to form the supermode, and the complex exponentials represent a phase term. There are two supermodes in a system of two coupled waveguides: one with even symmetry and one with odd symmetry (see figure 3.8). The amplitude weighting factors for the even supermode are given by

$$\begin{pmatrix} A_{\text{III-V}} \\ A_{\text{Si}} \end{pmatrix} = \begin{pmatrix} \frac{\mathrm{i}\kappa^*}{\delta - S} \\ 1 \end{pmatrix}, \quad (3.19)$$

where the various parameters are defined as

$$\kappa \equiv -\mathrm{i}\frac{\omega\epsilon_0}{4} \int_{-\infty}^{\infty} E_{\text{III-V}}^{*}(y)\ \Delta n^2\ E_{\text{Si}}(y)\ \mathrm{d}y, \tag{3.20}$$

$$2\delta \equiv \beta_{\text{Si}} - \beta_{\text{III-V}}, \tag{3.21}$$

$$S \equiv \sqrt{\delta^2 + |\kappa|^2}. \tag{3.22}$$

Physically, κ is the coupling strength between the two individual waveguides, Δn is the perturbation of the index resulting from the presence of the other waveguide [2, p.613], and δ is the phase detuning between the two individual waveguide modes.

An interesting case arises for $\delta < 0$ and $|\delta| \gg |\kappa|$. In this case, the amplitude weighting factors for the supermode are given by [66]

$$\begin{pmatrix} A_{\text{III-V}} \\ A_{\text{Si}} \end{pmatrix} = \begin{pmatrix} \frac{\mathrm{i}\kappa^*}{2\delta} \\ 1 \end{pmatrix}. \tag{3.23}$$

This is the desired result for modal engineering: the amplitude weighting factor for the supermode in the III-V waveguide is very small (by assumption of $|\delta| \gg |\kappa|$) and is tunable with the parameters κ and δ.

The field in the III-V waveguide is the sum of the exponentially decaying field from the silicon waveguide and the weighted field from the III-V waveguide (equation 3.18). The steep exponential decay of the silicon portion of the sum is expected to make the total field in the III-V waveguide dominated by the III-V portion of the sum. Equation 3.23 indicates two parameters that could be tuned in order to reduce $A_{\text{III-V}}$, thereby reducing the total field in the III-V portion of the waveguide:

Waveguide coupling (κ): Decreasing coupling between the silicon and III-V waveguides would reduce the supermode field in the III-V waveguide. Coupling could be decreased by moving the waveguides farther from each other, separating them with a low-index material.

Phase detuning (δ): Changing the transverse geometry of the silicon or III-V waveguide will change its individual propagation constant (β_i) thereby changing the
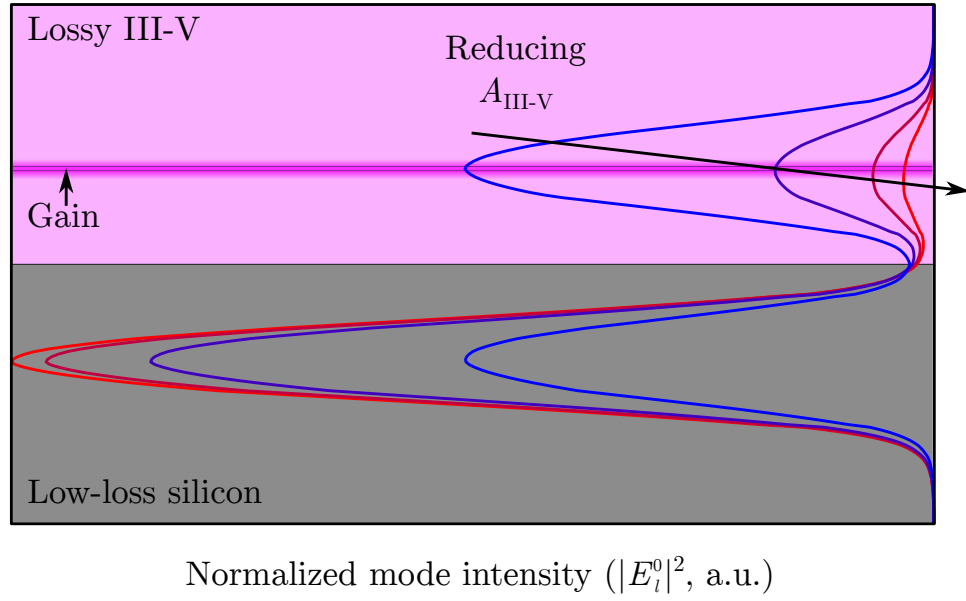
Figure 3.9: Simulated mode in a hybrid Si/III-V waveguide. As $\beta_{\text{III-V}}$ is decreased, $A_{\text{III-V}}$ decreases, and modal energy is removed from the III-V part of the hybrid Si/III-V waveguide.

phase detuning between the two waveguides. This was the technique previously used in our group to *increase* the electric field strength in the III-V region [66–70].

Figure 3.9 shows a simulated mode in a hybrid Si/III-V waveguide. In this figure, the propagation constant of the individual III-V waveguide ($\beta_{\text{III-V}}$) is decreased, causing $A_{\text{III-V}}$ to decrease, shifting modal energy away from the III-V and towards the low-loss silicon.

Reducing the laser mode intensity at the active region via modal engineering will decrease the single-carrier spontaneous transition rate into the laser mode according to Fermi's Golden Rule (W_{sp}, equation 2.26). The total spontaneous emission rate into the mode also depends on the total number of excited carriers (equation 2.55), so care must be taken that modal engineering does not cause the number of excited carriers at threshold to increase. Modal gain is proportional to the confinement factor of the mode in the active region (Γ_{act}) and optical absorption in III-V is proportional to the confinement factor of the mode in III-V ($\Gamma_{\text{III-V}}$). The supermode model shows

that these two confinement factors are expected to be proportional to $A_{\text{III-V}}^2$, so the ratio between the two should be constant under the modal engineering transformation.

In the end, supermode theory only provides a simple model for calculating how the confinement factors vary based on waveguide parameters. Numerical simulation of the actual transverse Si/III-V structure should be performed to verify the assumption that $\Gamma_{\text{III-V}}/\Gamma_{\text{act}}$ is constant for modal engineering.

3.3.2 Total quality factor

The total quality factor of the hybrid cavity under the modal engineering transformation is broken down into its constituent loss components, similar to the way it was done for the replacement transformation (equation 3.4). The equation for the total Q of a hybrid Si/III-V cavity (Q_{hybrid}) breaks down according to equation 2.13 to become

$$\frac{1}{Q_{\text{hybrid}}} = \frac{\Gamma_{\text{III-V}}}{Q_{\text{III-V}}} + \frac{1}{Q_{\text{passive}}}, \tag{3.24}$$

where $Q_{\text{III-V}}$ is the absorption loss in III-V and Q_{passive} includes all of the other sources of loss from the laser cavity.

Equation 3.24 has two regimes: one in which $\Gamma_{\text{III-V}}Q_{\text{III-V}}^{-1}$ limits Q_{hybrid} and one in which Q_{passive}^{-1} does. The value of $\Gamma_{\text{III-V}}$ at which the two component Q values are equal is termed the "critical confinement" (Γ_{crit}) because it designates a critical point in this analysis. At this point, Q_{hybrid} is half of Q_{passive}. Figure 3.10 shows an example plot of Q_{hybrid}.

Using supermode theory as a knob to tune $\Gamma_{\text{III-V}}$, the total Q of hybrid Si/III-V lasers is only limited by Q_{passive}, which must be maximized to get the highest Q_{hybrid}. Compare this to lasers which only undergo the replacement transformation, in which a fair amount of III-V must remain for electrical reasons and, consequently, are still limited by $\Gamma_{\text{III-V}}$.
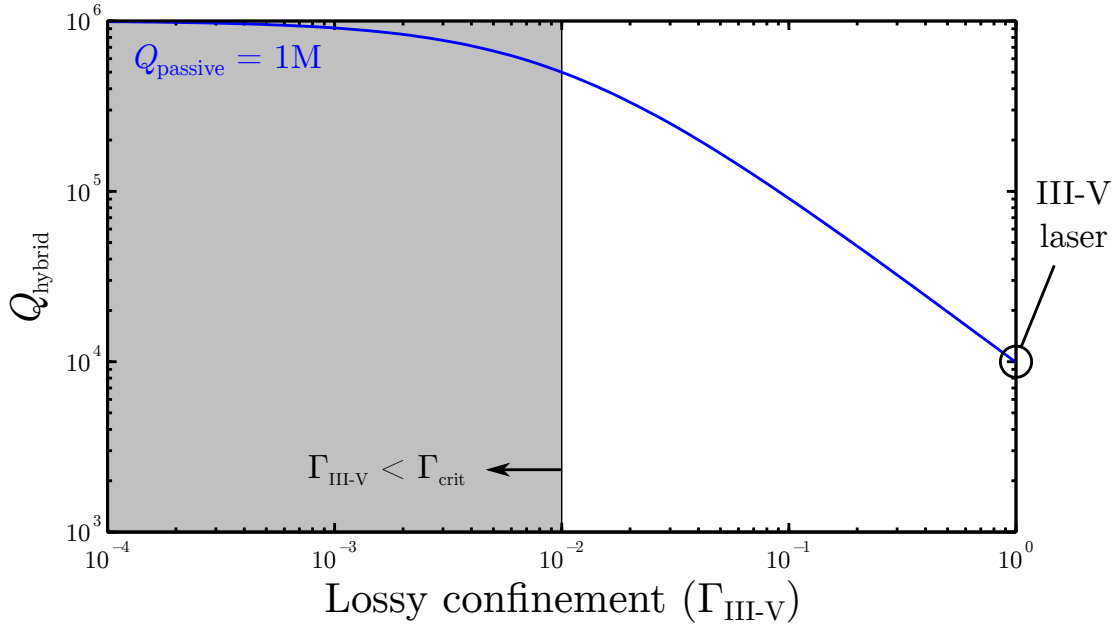
Figure 3.10: Total Q of the hybrid cavity under the modal engineering transformation only. The vertical line indicates the critical confinement, below which Q_{hybrid} saturates at the value of Q_{passive}. Assumptions: $Q_{\text{passive}} = 1\text{M}$, $Q_{\text{III-V}} = 10\text{k}$.

3.3.3 Threshold gain

The most important parameters determining the properties of modal engineering are the confinement factor in the lossy III-V material ($\Gamma_{\text{III-V}}$), causing loss, and the confinement factor of the mode in the active region (Γ_{act}), causing gain. The supermode model of modal engineering suggests that the ratio between these two ($\Gamma_{\text{III-V}}/\Gamma_{\text{act}}$) should be constant under this transformation.

The threshold modal gain of a hybrid Si/III-V laser undergoing modal engineering is found by substituting the hybrid cavity Q (equation 3.24) into the threshold modal gain for a general cavity (equation 2.14);

$$\Gamma_{\text{act}} g_{\text{th}} = \frac{\omega}{v_{\text{g}} Q_{\text{hybrid}}} = \frac{\omega}{v_{\text{g}}} \left(\frac{\Gamma_{\text{III-V}}}{Q_{\text{III-V}}} + \frac{1}{Q_{\text{passive}}} \right). \tag{3.25}$$

The threshold material gain is thus given by

$$g_{\text{th}} = \frac{\omega}{v_{\text{g}}} \left(\frac{\Gamma_{\text{III-V}}}{\Gamma_{\text{act}}} \frac{1}{Q_{\text{III-V}}} + \frac{1}{\Gamma_{\text{act}} Q_{\text{passive}}} \right). \tag{3.26}$$
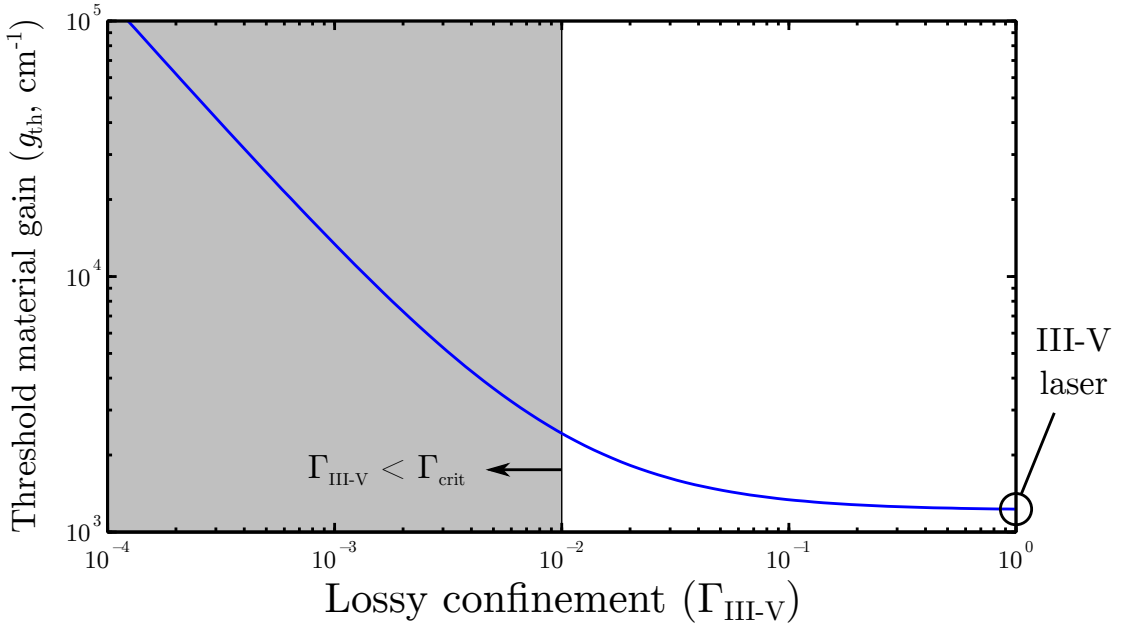
Figure 3.11: Threshold material gain of a hybrid Si/III-V laser under the modal engineering transformation. Material gain is approximately constant for $\Gamma_{\text{III-V}}$ greater than the critical confinement. Compare this figure to figure 3.3 to see the difference between this transformation and the replacing III-V with silicon transformation. Assumptions: $Q_{\text{III-V}} = 10\text{k}$, $Q_{\text{passive}} = 1\text{M}$, $\Gamma_{\text{III-V}}/\Gamma_{\text{act}} = 100$, $g_0 = 3 \times 10^3 \, \text{cm}^{-1}$, $n_{\text{g}} = 3$.

For $\Gamma_{\text{III-V}} > \Gamma_{\text{crit}}$, absorption losses in III-V dominate the total threshold material gain.

From the supermode model of the confinement factors in a hybrid Si/III-V laser undergoing this transformation, the ratio $\Gamma_{\text{III-V}}/\Gamma_{\text{act}}$ is expected to be constant. Therefore, the threshold material gain is constant under the modal engineering transformation for $\Gamma_{\text{III-V}} > \Gamma_{\text{crit}}$. This is a very important result! The simple explanation of this behavior is that as the shape of the mode is engineered, both losses and modal gain decrease by the same factor, so threshold is unchanged.

For $\Gamma_{\text{III-V}} < \Gamma_{\text{crit}}$, the second term on the right-hand side of equation 3.26 dominates the threshold material gain. In this regime, reducing $\Gamma_{\text{III-V}}$ causes an increase in threshold material gain. This is usually undesirable, though perhaps some amount of increased material gain can be tolerated. Figure 3.11 shows the threshold material gain in a hybrid Si/III-V laser under the modal engineering transformation.

This discussion highlights the importance of both transformations available for making hybrid Si/III-V lasers. First, replacing lossy III-V with low-loss silicon reduces the threshold gain. Then, engineering the mode to further reduce confinement in the lossy region keeps threshold gain constant while continuing to increase Q_{hybrid}.

3.3.4 Spontaneous emission rate into the laser mode

The spontaneous emission rate into the laser mode is related to the cavity Q by equation 2.61

$$R_{\text{sp}} = \frac{\omega\mu}{Q_{\text{hybrid}}} = \omega\mu\left(\frac{\Gamma_{\text{III-V}}}{Q_{\text{III-V}}} + \frac{1}{Q_{\text{passive}}}\right),\tag{3.27}$$

where equation 3.24 was used to express Q_{hybrid}. Like all equations related to the modal engineering transformation, this equation is split into two regimes by the critical confinement (Γ_{crit}). The spontaneous emission rate into the mode varies differently in these two regimes.

$\Gamma_{\text{III-V}} > \Gamma_{\text{crit}}$: Equation 3.26 shows that the threshold gain is independent of $\Gamma_{\text{III-V}}$ in this regime because the ratio of $\Gamma_{\text{III-V}}/\Gamma_{\text{act}}$ stays constant. Therefore, it is reasonable to assume that the carrier populations in both the valence and conduction bands will be independent of $\Gamma_{\text{III-V}}$, making the population inversion factor (μ) independent of $\Gamma_{\text{III-V}}$.

Therefore, in this regime, the spontaneous emission rate scales with $\Gamma_{\text{III-V}}$. Hybrid Si/III-V lasers receive the full benefit of scaling with $\Gamma_{\text{III-V}}$ under the modal engineering transformation, even near transparency. This is different from the replacement transformation in which R_{sp} is constant near transparency. Threshold inversion is the same for all values of $\Gamma_{\text{III-V}}$ in this regime. The spontaneous emission rate is

$$R_{\text{sp}} = \omega\mu\frac{\Gamma_{\text{III-V}}}{Q_{\text{III-V}}}\tag{3.28}$$

$$\propto \Gamma_{\text{III-V}}.$$

$\boldsymbol{\Gamma_{\text{III-V}} \ll \Gamma_{\text{crit}}}$: In this regime, the threshold material gain increases with decreasing $\Gamma_{\text{III-V}}$ (equation 3.26), so changes in the population inversion factor (μ) must be considered. This regime is to be avoided because of increasing threshold. The spontaneous emission rate is

$$R_{\text{sp}} = \frac{\omega\mu}{Q_{\text{passive}}} \qquad (3.29)$$

$$\not\propto \Gamma_{\text{III-V}}.$$

The phenomenological description

Once again, the phenomenological approach to calculating R_{sp} gives an intuitive physical description of the effects of modal engineering in hybrid Si/III-V lasers. This approach yields the same results for the regime in which III-V absorption dominates Q_{hybrid}, but it differs somewhat for very small $\Gamma_{\text{III-V}}$. The current required to pump a hybrid Si/III-V laser operating in that regime is extraordinarily high, so any useful laser will avoid this regime and the difference in expected linewidth is unimportant.

The spontaneous emission rate into the mode is described by the phenomenological equation 2.49, reproduced here

$$R_{\text{sp}} = \frac{\beta_{\text{sp}} N_{\text{th}}}{\tau_{\text{sp}}}. \qquad (3.30)$$

This equation is intuitive: to reduce R_{sp}, the laser design must reduce the number of carriers at threshold (N_{th}), reduce the fraction of the total spontaneous emission that enters the lasing mode (β_{sp}), and/or reduce the spontaneous emission rate into all modes (τ_{sp}^{-1}). This phenomenological approach to calculating R_{sp} is somewhat inaccurate because β_{sp} and N_{th} are hard to calculate *ab initio*. However, this approach leads to a more intuitive understanding of how the various components of R_{sp} vary with $\Gamma_{\text{III-V}}$ under the modal engineering transformation.

Carrier density is monotonically related to gain (above transparency), so the number of excited carriers at threshold will remain unchanged if threshold material gain
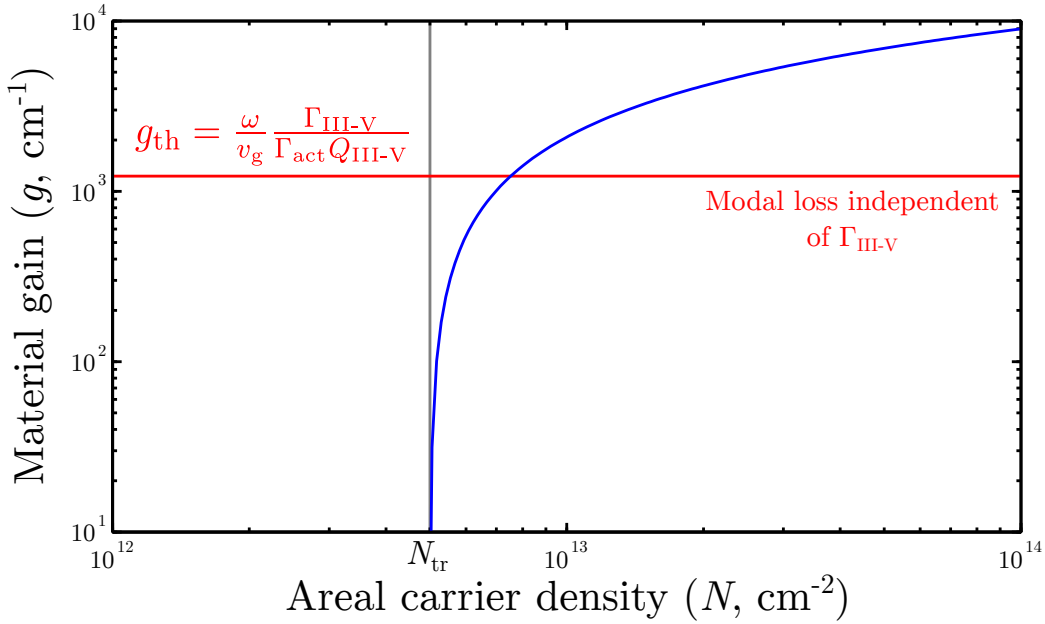
Figure 3.12: Material gain vs. carrier density in hybrid Si/III-V lasers. The horizontal red line shows the threshold material gain in lasers undergoing the modal engineering transformation with confinement greater than the critical confinement. Assumptions: $Q_{\text{III-V}} = 10\text{k}$, $\Gamma_{\text{III-V}}/\Gamma_{\text{act}} = 100$, $g_0 = 3 \times 10^3 \, \text{cm}^{-1}$, and $N_{\text{tr}} = 5 \times 10^{12} \, \text{cm}^{-2}$.

also remains unchanged. Empirical equation 2.45, relating gain and carrier density, shows that threshold carrier density will blow up exponentially with increasing threshold gain. Figure 3.12 shows this exponential relationship along with the estimated threshold gain of a hybrid Si/III-V laser undergoing the modal engineering transformation with $\Gamma_{\text{III-V}} > \Gamma_{\text{crit}}$. The intersection of these two lines gives the threshold gain and carrier density.

Figure 3.13 shows the threshold carrier density in hybrid Si/III-V lasers under the modal engineering transformation. For $\Gamma_{\text{III-V}} < \Gamma_{\text{crit}}$, threshold carrier density increases exponentially with decreasing $\Gamma_{\text{III-V}}$. This regime should be avoided at all costs.

The spontaneous emission coupling factor (β_{sp}) was shown in equation 2.44 to be proportional to Γ_{act}. It also has a dependence on the inhomogeneous linewidth (Δf_{i}), which will increase with an increase in N_{th} as low-energy states fill. Therefore, β_{sp} is expected to scale as $\Gamma_{\text{III-V}}$ in the constant-threshold regime, but its behavior is complicated as threshold increases.
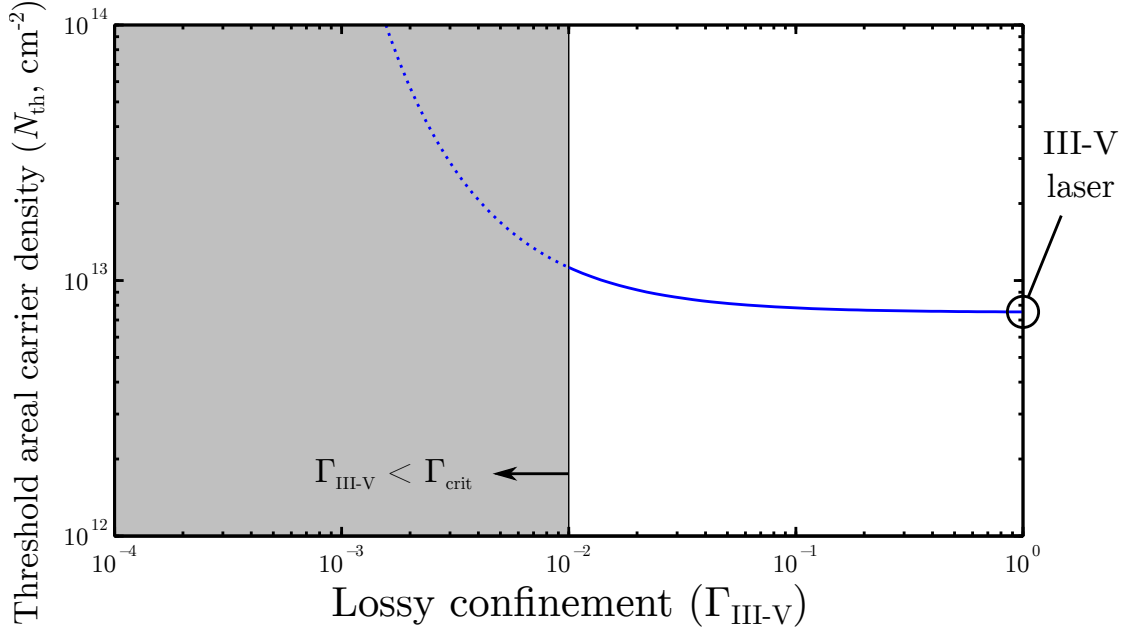
Figure 3.13: Threshold carrier density in a laser undergoing the modal engineering transformation. Assumptions: $Q_{\text{III-V}} = 10k$, $Q_{\text{passive}} = 1M$, $\Gamma_{\text{III-V}}/\Gamma_{\text{act}} = 100$, $g_0 = 3 \times 10^3 \, \text{cm}^{-1}$, and $N_{\text{tr}} = 5 \times 10^{12} \, \text{cm}^{-2}$.

The spontaneous transition rate into all modes (τ_{sp}^{-1}) was calculated in equation 2.42 to be independent of the shape of the lasing mode.

Combining these individual results, the big effect of modal engineering is to decrease the spontaneous emission rate into the laser mode while leaving the spontaneous emission rate into all other modes unchanged. The spontaneous emission coupling factor (β_{sp}) is the only term that affects R_{sp} under modal engineering while absorption losses in III-V dominate. The spontaneous emission rate into the laser mode is therefore expected to scale as $\Gamma_{\text{III-V}}$.

3.3.5 Photon storage

Equation 2.65 for the number of stored photons was calculated without any assumptions about the cavity design or the operating point. It states that the number of stored photons (N_{p}) scales with Q_{hybrid}

$$N_{\text{p}} = \frac{\eta_{\text{i}}}{\omega} \frac{(I - I_{\text{th}})}{q} \left(\frac{\Gamma_{\text{III-V}}}{Q_{\text{III-V}}} + \frac{1}{Q_{\text{passive}}} \right)^{-1}, \tag{3.31}$$

where equation 3.24 was used to express Q_{hybrid}.

The two regimes for this equation are the same as for the replacement transformation. For $\Gamma_{\text{III-V}} > \Gamma_{\text{crit}}$, N_{p} scales as $\Gamma_{\text{III-V}}$. For $\Gamma_{\text{III-V}} < \Gamma_{\text{crit}}$, N_{p} is independent of $\Gamma_{\text{III-V}}$. The number of stored photons scales in exactly the same way as Q_{hybrid}, which was plotted in figure 3.10.

3.3.6 Linewidth

The results of calculating the spontaneous emission rate into the mode and photon storage can be inserted into the Schawlow-Townes linewidth formula (equation 2.71), showing how linewidth varies under the modal engineering transformation. There are two relevant regimes:

$\boldsymbol{\Gamma_{\text{III-V}} > \Gamma_{\text{crit}}}$: Linewidth scales with $\Gamma_{\text{III-V}}^2$. This is a very important result! For the replacement transformation, the scaling factor was as low as $\Gamma_{\text{III-V}}$ for lasers operating near transparency. The modal engineering transformation receives the full $\Gamma_{\text{III-V}}^2$ regardless of operating point. The linewidth is

$$\Delta f = \frac{\omega^2}{4\pi} \left(\frac{\Gamma_{\text{III-V}}}{Q_{\text{III-V}}} \right)^2 \frac{q}{I - I_{\text{th}}} \frac{\mu}{\eta_{\text{i}}} (1 + \alpha^2) \tag{3.32}$$
$$\propto \Gamma_{\text{III-V}}^2.$$

$\boldsymbol{\Gamma_{\text{III-V}} \ll \Gamma_{\text{crit}}}$: Linewidth is independent of $\Gamma_{\text{III-V}}$. Both the spontaneous emission rate into the mode and number of stored photons have saturated at their values limited by Q_{passive}, demonstrating the importance of a high Q_{passive}. Threshold carrier density increases exponentially with $\Gamma_{\text{III-V}}^{-1}$ in this regime, so it should be avoided. The linewidth is

$$\Delta f = \frac{\omega^2}{4\pi} \left(\frac{1}{Q_{\text{passive}}} \right)^2 \frac{q}{I - I_{\text{th}}} \frac{\mu}{\eta_{\text{i}}} (1 + \alpha^2) \tag{3.33}$$
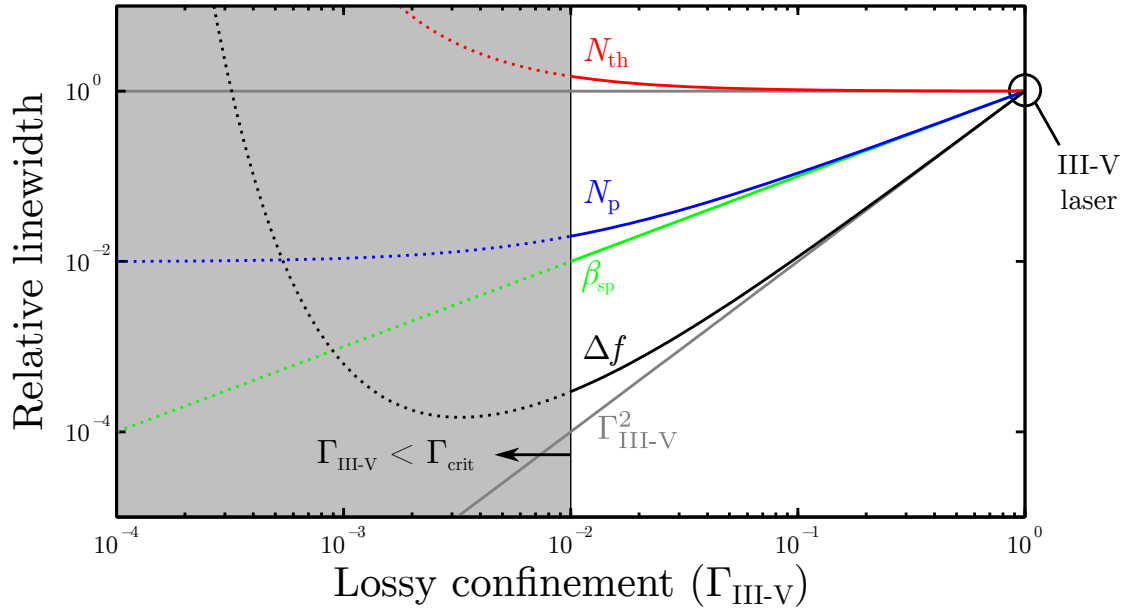$$\not\propto \Gamma_{\text{III-V}}^2.$$

Figure 3.14: The relative linewidth of a hybrid Si/III-V laser undergoing the modal engineering transformation. The various components affecting the relative linewidth are plotted as colored lines and the linewidth itself (Δf) is plotted in black. This plot should not be trusted in the $\Gamma_{\text{III-V}} < \Gamma_{\text{crit}}$ regime because changes in the inhomogenously-broadened spontaneous emission lineshape are not included. Assumptions: $Q_{\text{III-V}} = 10\text{k}$, $Q_{\text{passive}} = 1\text{M}$, $\Gamma_{\text{III-V}}/\Gamma_{\text{act}} = 100$, $g_0 = 3 \times 10^3 \, \text{cm}^{-1}$, and $N_{\text{tr}} = 5 \times 10^{12} \, \text{cm}^{-2}$.

The phenomenological description

Alternately, the phenomenological approach to calculating the spontaneous emission rate can also be combined with photon storage to understand intuitively how linewidth varies with $\Gamma_{\text{III-V}}$. The confinement factor in the active region (Γ_{act}) affects the fraction of the total spontaneous emission that couples to the lasing mode (β_{sp}), the number of excited carriers at threshold (N_{th}), and the number of stored photons (N_{p}). These three terms can be combined to calculate relative linewidths:

$$\text{relative linewidth} \equiv \frac{N_{\text{th}}\beta_{\text{sp}}}{Q_{\text{hybrid}}}. \tag{3.34}$$

A hybrid Si/III-V laser with a relative linewidth less than unity thus has a narrower linewidth than a corresponding III-V-only laser. Figure 3.14 shows a plot of this relative linewidth.

Note that the result from this method varies significantly from the (more accurate) result derived from the rate equations and quantum mechanics for $\Gamma_{\text{III-V}} \ll \Gamma_{\text{crit}}$. For $\Gamma_{\text{III-V}} > \Gamma_{\text{crit}}$, the two approaches yield identical results and the phenomenological approach provides a valuable physical description of modal engineering. The apparent optimum confinement lies in a region where the two approaches differ and therefore should be ignored. The linewidth derived from the phenomenological approach is invalid in that regime.

3.3.7 Limits of modal engineering

Laser linewidths attainable by modal engineering are fundamentally limited by the value of Q_{passive} which can be achieved. The narrowest practical linewidths will be found in lasers which have reduced $\Gamma_{\text{III-V}}$ to be equal to the critical confinement, which was defined based on the value of Q_{passive}.

Fabrication defects are likely to limit Q_{passive}. As fabrication techniques improve, this modal engineering technique will be pushed further to create lasers with modes that are weaker in III-V than what is achievable today.

3.4 Designing a low-noise Si/III-V laser

Two steps for reducing the noise in semiconductor lasers have been presented in this chapter: replacing lossy III-V with low-loss silicon and engineering the shape of the laser mode to reduce energy storage in lossy III-V to the extreme.

3.4.1 Comparing replacement to modal engineering

Figure 3.15 compares the relative linewidth of a hybrid Si/III-V laser under the replacement and modal engineering transformations relative to a III-V only laser (see figures 3.6 and 3.14 for the sources).

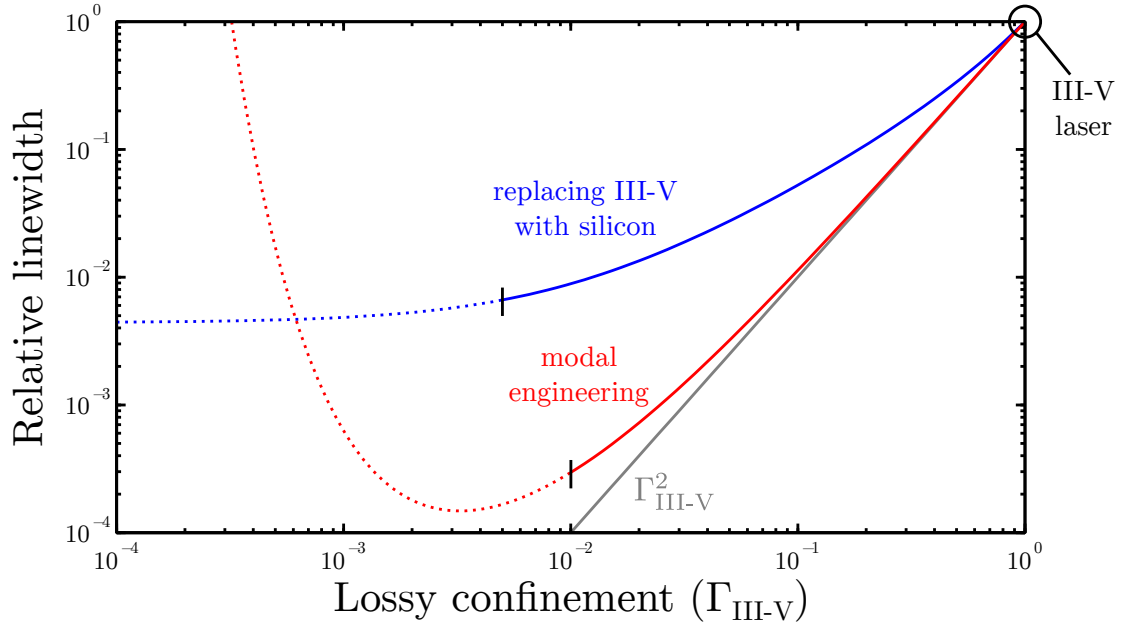The linewidth formula that is valid for any laser was derived in equation 2.79,

Figure 3.15: Comparison of the noise performance of hybrid Si/III-V lasers under the replacement and modal engineering transformations individually. Each transformation is marked with a cutoff: replacement at the point were the solution becomes non-physical ($\Gamma_{\text{III-V}} < \Gamma_{\text{act}}$) and modal engineering at the critical confinement where threshold gain starts to increase. Assumptions: $Q_{\text{passive}} = 1\text{M}$, $Q_{\text{III-V}} = 10\text{k}$, $g_0 = 3 \times 10^3 \, \text{cm}^{-1}$, $N_{\text{th}} = 5 \times 10^{12} \, \text{cm}^{-2}$, $\Gamma_{\text{act}} = 0.5\%$ (replacement), $\Gamma_{\text{act}} = \Gamma_{\text{III-V}}/100$ (modal engineering).

reproduced here:

$$\Delta f = \frac{1}{4\pi} \frac{\omega^2}{Q^2} \frac{q}{I - I_{\text{th}}} \frac{\mu}{\eta_{\text{i}}} (1 + \alpha^2). \tag{3.35}$$

Keeping pump current above threshold constant, the linewidth of a laser will vary with μ/Q^2. The difference between the two transformations comes in how the population inversion factor (μ) varies with $\Gamma_{\text{III-V}}$. These differences can be summarized as:

Replacing III-V with silicon: This transformation decreases linewidths and decreases threshold current, with diminishing returns to both coming as threshold carrier density nears transparency. Replacing III-V with silicon yields a maximum benefit to linewidth of a factor of $\Gamma_{\text{III-V}}^2$. The improvement drops to a factor of $\Gamma_{\text{III-V}}$ near transparency. Reducing transparency (e.g., by reducing the number of quantum wells) will recover the $\Gamma_{\text{III-V}}^2$ dependence.

Modal engineering: Modal engineering decreases linewidths while keeping threshold constant as long as optical absorption in III-V dominates total losses. Modal engineering is necessary to reach the extremely small modal confinement in III-V needed to take full advantage of high Q_{passive}. Linewidths decrease by a factor of $\Gamma_{\text{III-V}}^2$ regardless of the transparency value, so reducing transparency will have no effect on hybrid Si/III-V lasers undergoing the modal engineering transformation.

Reduced thresholds are the only advantage that the replacement transformation has over modal engineering. Considering linewidths only, the dependence of linewidth on μ/Q^2 indicates that lasers having equally-narrow linewidths can be made using modal engineering with any value for transparency as long as the population inversion factor is the same in each laser.

The differences between the two transformations reveal that the traditional laser design strategy of "maximizing gain while reducing losses" does not result in the narrowest possible linewidths. This naïve approach is embodied by the replacement transformation, which is never better than properly-executed modal engineering. Similarly, a design strategy of "decreasing gain relative to loss" is bad because it results

in increased thresholds. This approach is embodied by modal engineering with $\Gamma_{\text{III-V}}$ less than the critical confinement. The optimal strategy for reducing phase noise in a laser turns out to be modal engineering, which reduces loss and gain by the same factor.

3.4.2   Combining replacement with modal engineering

The discussion in this chapter leads to a simple design process for making narrow linewidth semiconductor lasers. Replacing III-V with silicon should be done in the regime where linewidth has the full $\Gamma_{\text{III-V}}^2$ dependence in order to reduce thresholds. Otherwise modal engineering should be used. The basic strategy is then to:

1. Reduce the transparency carrier density to the smallest attainable value for a low-loss laser. This is probably done by reducing the number of quantum wells used in the gain medium.

2. Replace excess lossy III-V in the laser cavity with low-loss silicon until threshold carrier density nears transparency. This transformation decreases linewidth by a factor of nearly $\Gamma_{\text{III-V}}^2$.

3. Engineer the mode to remove modal energy from III-V until absorption no longer dominates the total Q of the laser cavity. This transformation decreases linewidth by a factor of $\Gamma_{\text{III-V}}^2$.

The replacement and modal engineering transformations form a basis for converting any III-V-only laser to a hybrid Si/III-V laser by starting with the value of Γ_{act} of the III-V laser and $\Gamma_{\text{III-V}} = 100\%$. Figure 3.16 shows the linewidth of a hybrid Si/III-V laser made by combining the two transformations relative to a III-V-only laser. The "switching" point between the two transformations is taken to be $\Gamma_{\text{III-V}} = 25\%$. With the parameters chosen, the narrowest achievable linewidth using both transformations is basically the same as it would be with the modal engineering transformation only. By including the replacement transformation, there is an additional benefit of lower threshold currents in hybrid Si/III-V lasers.
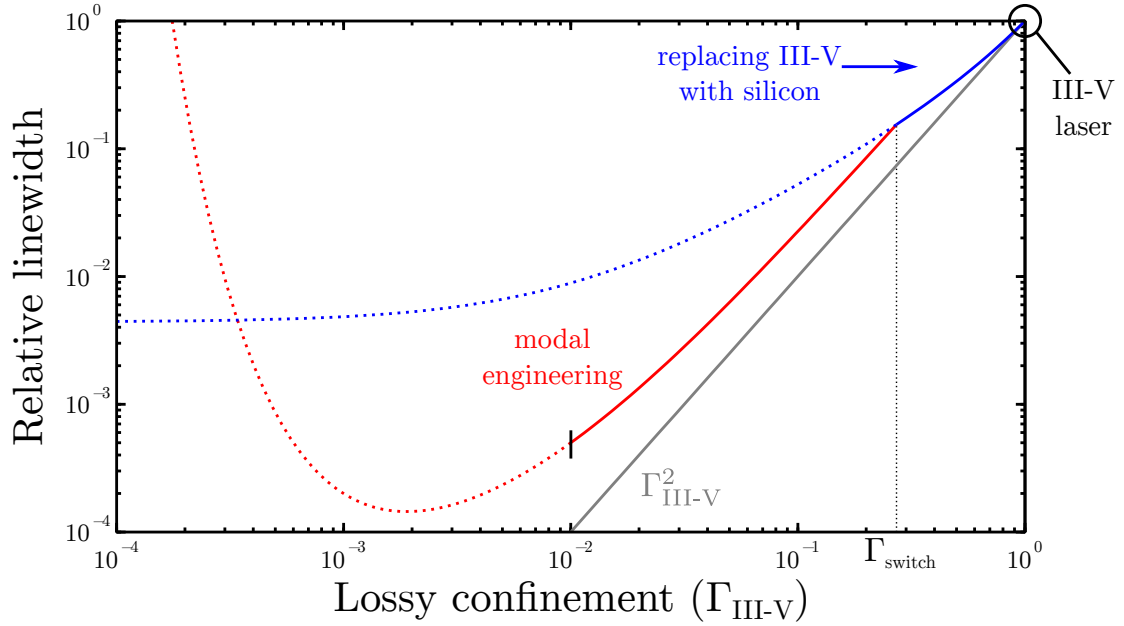
Figure 3.16: Phase noise performance of a hybrid Si/III-V laser combining the replacement and modal engineering transformations relative to a III-V-only laser. Assumptions: $Q_{\text{passive}} = 1M$, $Q_{\text{III-V}} = 10k$, $g_0 = 3 \times 10^3\,\text{cm}^{-1}$, $N_{\text{th}} = 5 \times 10^{12}\,\text{cm}^{-2}$, $\Gamma_{\text{act}} = 0.5\%$ (replacement), $\Gamma_{\text{act}}/\Gamma_{\text{III-V}}$ taken at the switching point between the two transformations (modal engineering).

Two types of hybrid Si/III-V lasers are presented in this thesis: the high-Q hybrid laser (the replacement transformation) and the spacer laser (modal engineering).

In the end, a hybrid Si/III-V laser must be analyzed using a numerical simulation of the mode so that the real values of $\Gamma_{\text{III-V}}$ and Γ_{act} can be found. All of this discussion of "transformations" is simply a way to understand the algebra involved in designing hybrid Si/III-V lasers. The relative linewidths presented indicate that hybrid Si/III-V lasers may have linewidths more than 1,000 times narrower than similar III-V-only lasers, if a passive silicon Q of 1M is reached.

Chapter 4

High-Q hybrid lasers

Experimental results for replacing III-V with silicon

This chapter presents the high-Q hybrid laser as an experimental test of the transformation by which low-loss silicon replaces lossy III-V in a hybrid Si/III-V laser cavity. The theory for this replacement transformation was discussed in section 3.2.

In the replacement transformation, the modal confinement in the lossy III-V region decreases while confinement in the active region stays constant. The replacement transformation describes high-Q hybrid lasers well because existing narrow-linewidth [47; 48] or high-power [43; 49] III-V lasers have similar active confinement factors (Γ_{act}) as the lasers described here. The primary improvements made to high-Q hybrid lasers over these existing lasers are the introduction of silicon as a low-loss material and the use of a high-Q modegap grating to reduce non-absorption sources of loss.

As expected from the replacement transformation theory, high-Q hybrid lasers are found to have low threshold current densities and narrow linewidths. The lowest estimated threshold current densities in fabricated high-Q hybrid lasers are around $400\,\text{A}\,\text{cm}^{-2}$. The best measured high-Q hybrid laser has an upper bound on its "spontaneous emission linewidth" of $18\,\text{kHz}$ and all high-Q hybrid lasers have linewidths narrower than $80\,\text{kHz}$.

The high-Q hybrid laser presented in this chapter serves as a baseline for the improvements described in next chapter. The key metrics of linewidth and threshold
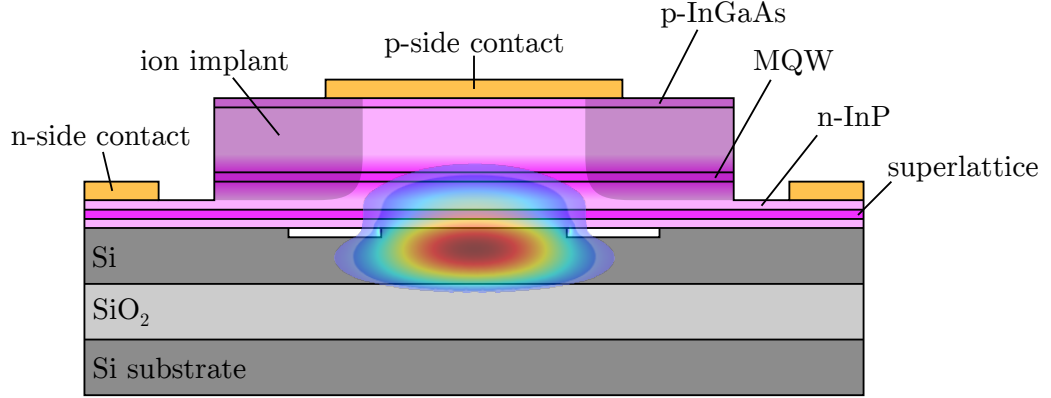
Figure 4.1: Cartoon cross-section of the transverse hybrid Si/III-V geometry used in high-Q hybrid lasers.
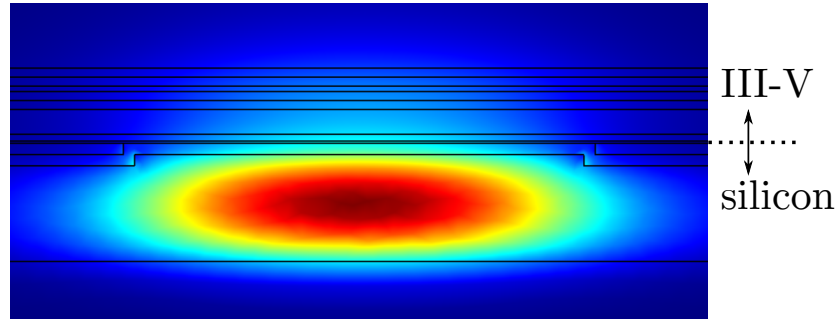

Figure 4.2: The fundamental transverse mode supported by high-Q hybrid laser waveguides, as calculated in Comsol. The mode is mostly located in the silicon device layer. Above the mode is the thin thermal oxide layer, conforming to the waveguide shape, and the various III-V layers bonded to the SOI chip.

will be compared to other designs. The information in this chapter is incomplete and more detail can be found in Christos Santis's thesis [71].

4.1 Simulation

Two-dimensional simulation is used to design the transverse geometry of high-Q hybrid lasers by calculating optical confinement factors in the lossy and active regions. Figure 4.1 presents a cartoon version of the waveguide's transverse structure. A very thin thermal oxide layer is grown on the top of the silicon device layer in order to smooth the etched sidewalls. The fundamental TE mode supported by such a waveguide can be seen in figure 4.2. The confinement factors for the fundamental mode are

Parameter	Value
Confinement in III-V ($\Gamma_{\text{III-V}}$)	18%
Confinement in MQW (Γ_{act})	1.4%
Q_{passive} (assumed)	1M
Quadratic well depth (V)	$\{100, 120\}$ GHz
Quadratic well width (L_{d})	200 µm
Period (Λ)	$\{230, 232.5, 235, 237.5, 240\}$ nm
Waveguide rib width	2 µm
Waveguide etch depth	50 nm
Grown oxide thickness	30 nm
Device layer thickness	485 nm
Buried oxide thickness	1 µm

Table 4.1: Nominal parameters used to fabricate high-Q hybrid lasers.

given in table 4.1. The active confinement factor of 1.4% is very similar to comparable III-V-only lasers.

4.2 Fabrication and characterization

High-Q hybrid lasers were fabricated based on the parameters in table 4.1. Fabrication details can be found in appendix C.

Facets are cleaved after lapping the silicon handle down to around 150 µm, and a single layer of aluminum oxide around 220 nm thick is applied as an anti-reflection coating. The cleave is not perfect, so the exact number of mirror holes is unknown for each cleaved bar, though the number should be large enough so that external coupling is very small compared to other sources of loss.

Bare lasers are tested on a temperature-controlled stage. Some are die bonded to a C-mount using an indium-based solder for better temperature control. The lasers are unpackaged, though they are contained within a large plastic box which reduces temperature variations due to air currents.
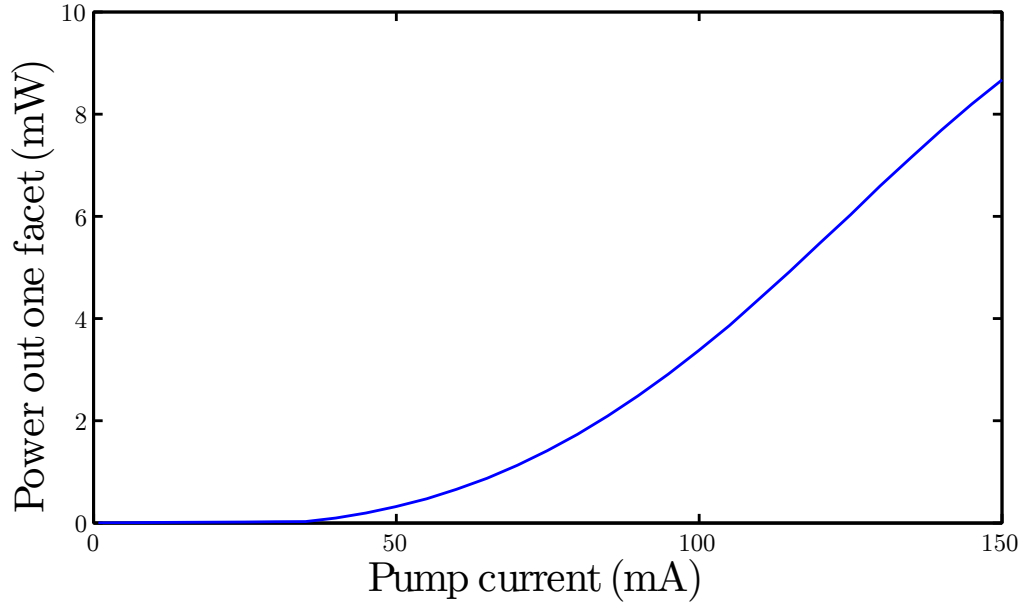
Figure 4.3: LI curve for the high-Q hybrid laser with the highest single-sided output power. The laser begins to mode-hop between longitudinal modes at pump currents slightly higher than those shown here. (Device ID: HQhL1 Ch1 B5 S1 D8, $\lambda \approx$ 1546 nm)

4.2.1 Threshold and power output

High-Q hybrid lasers have thresholds as low as 27 mA and output power as high as 9 mW.

The LI curve for the laser with the highest single-mode output power is shown in figure 4.3. This laser has a threshold of 30 mA and an output power of nearly 9 mW. The lowest measured threshold is 27 mA. The active region of this laser is approximately 8 μm by 1 mm, so the threshold current density may be lower than 400 mA cm^{-2}, assuming uniform current density. This assumption is probably wrong, and the real value could be higher.

A scatter plot of all measured thresholds is shown in figure 4.4. Wavelength is determined mostly by the period of the grating. The best thresholds are found in lasers operating near the peak of the gain spectrum (see figure 4.7). Lasing is achieved over a wavelength span from 1520 to 1580 nm.
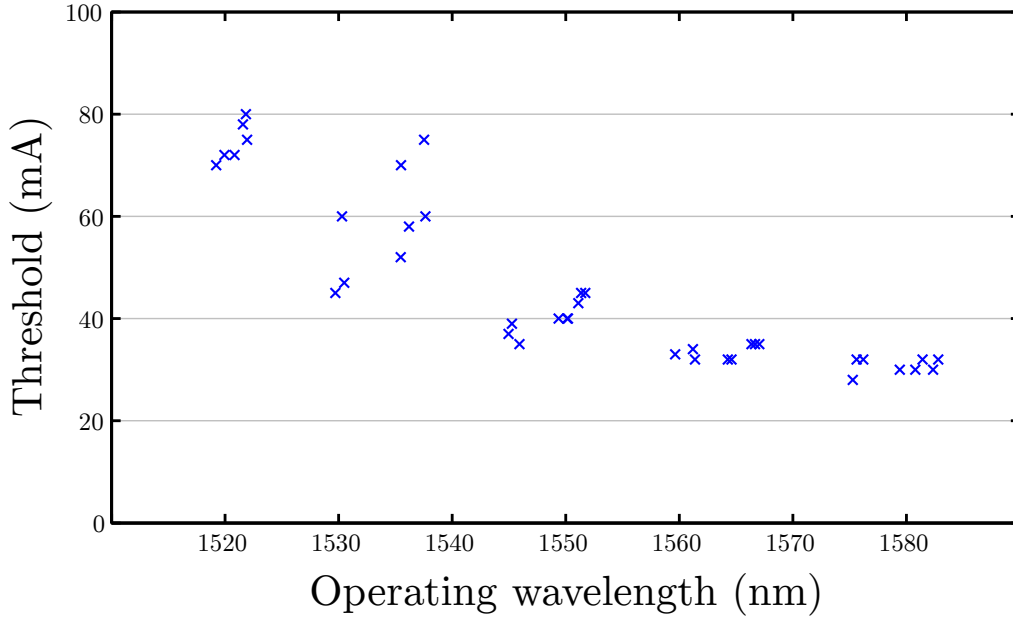
Figure 4.4: Scatter plot of all measured thresholds for high-Q hybrid lasers. Wavelength values for each data point have been jittered slightly to separate duplicates. (Stage temperature 20 °C)

Temperature dependence

The temperature dependence of threshold was determined by taking LI curves and varying the stage temperature. The laser used in this experiment was die bonded to a C-mount for good heat sinking. Figure 4.5 shows the data. Lasing is achieved up to a stage temperature of 75 °C. Thermal rolloff occurs at the relatively low multiple of 7 times threshold at 20 °C.

4.2.2 Optical spectrum and sidemode suppression

The optical spectrum is found using an optical spectrum analyzer with a resolution of 0.08 nm. This measurement will not sufficiently resolve the spectrum to make a linewidth measurement, but it can be used to determine the lasing wavelength relative to the bandgap and the sidemode suppression ratio (SMSR).

Figure 4.6 shows the optical spectrum of the device with the best sidemode suppression ratio of 51 dB. This figure should be compared qualitatively to figure A.10, the simulated transmission spectrum of a passive device. The lasing mode is found
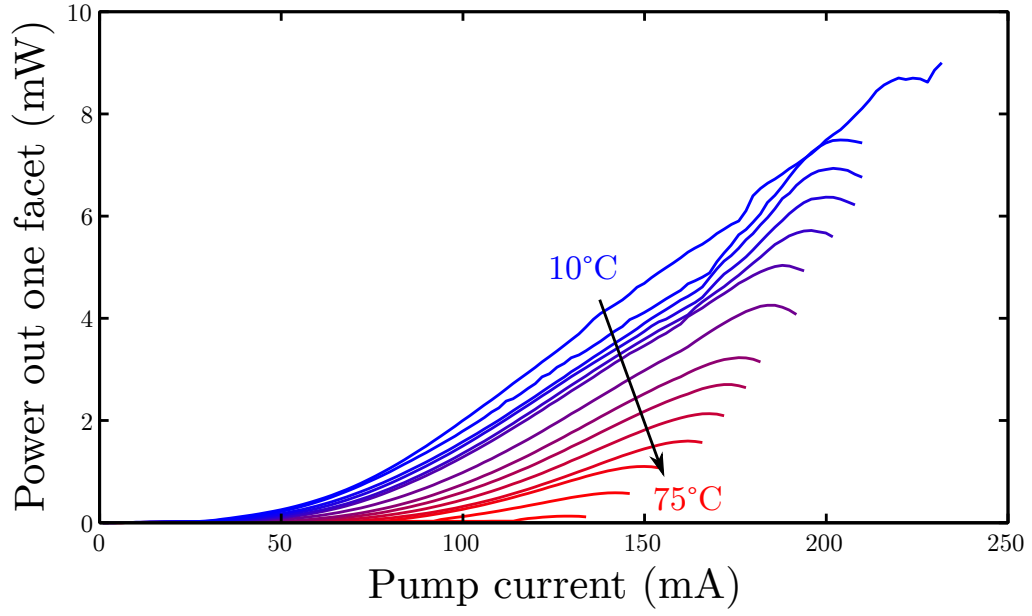
Figure 4.5: Temperature dependence of LIV curves. Curves are taken from 10 to 75 °C, with steps of 5 °C. (Device ID: HQhL1 Ch1 B5 S1 D15, $\lambda \approx 1575\,\text{nm}$)
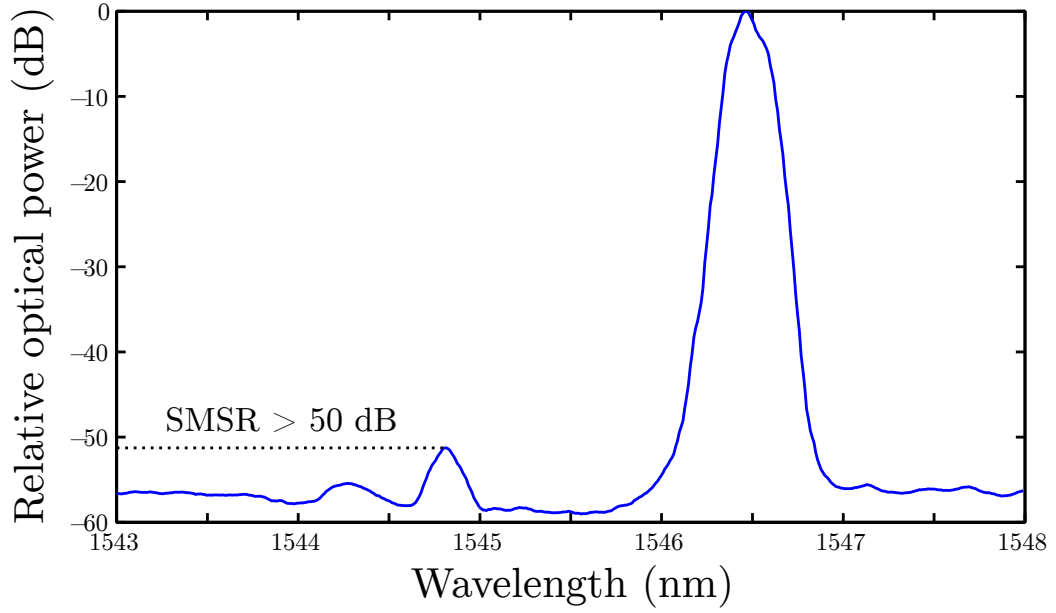

Figure 4.6: Optical spectrum of the high-Q hybrid laser with the best sidemode suppression ratio. (Device ID: HQhL1 Ch1 B5 S1 D7, $\lambda \approx 1546\,\text{nm}$)
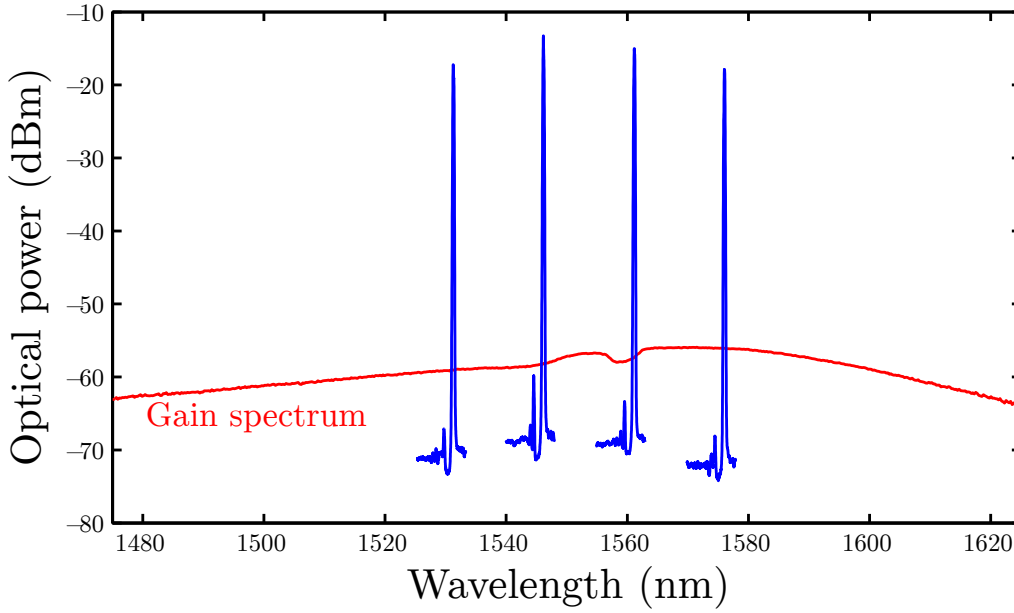
Figure 4.7: Optical spectra of four devices. The spontaneous emission spectrum of the active III-V material is shown in red. The dip in the spontaneous emission spectrum around 1560 nm is the photonic bandgap, as this measurement was taken from one of the real devices below threshold. (Device IDs HQhL1 Ch1 B5 S1 D6; HQhL1 Ch1 B5 S1 D7; HQhL1 Ch1 B5 S1 D12; HQhL1 Ch1 B5 S1 D15)

near the red side of the photonic bandgap, where the photonic well is located. The strongest sidemode is observed on the blue side of the photonic bandgap because these modes have low spatial overlap with the lasing mode.

Figure 4.7 shows the spectra of four devices with different operating wavelengths (due to different grating periods) with the gain spectrum of the III-V material below threshold.

4.2.3 Frequency noise PSD and linewidth

Frequency noise power spectral density measurements are taken using the experimental setup described in appendix B.1.

Figure 4.8 shows the frequency noise spectrum (S_f) for the device with the lowest noise. The steep $1/f$ segment at frequency offsets less than 10 kHz is the combination of natural $1/f$ noise in the laser (due to temperature fluctuations, etc.) and noise that is injected into the laser from the feedback circuit used to keep the system locked
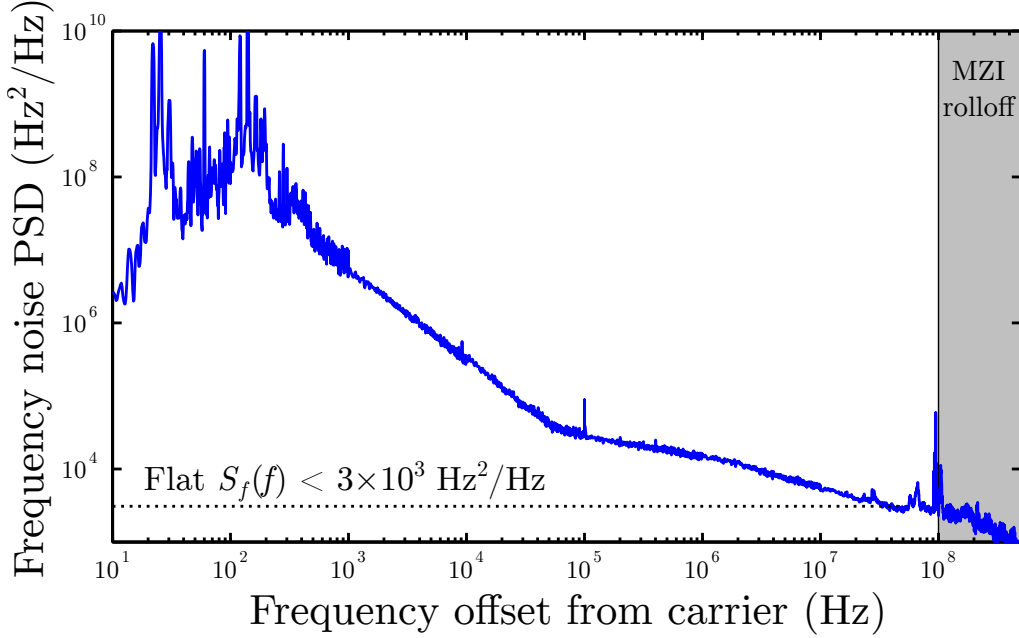
Figure 4.8: Frequency noise power spectral density (S_f) of the lowest-noise high-Q hybrid laser. The dotted line indicates an upper bound on the flat, "white" power spectral density expected from spontaneous emission. (Device ID: HQhL1 Ch2 B5 S2 D10, $\lambda \approx 1567\,\mathrm{nm}$. $I = 160\,\mathrm{mA}$; $I - I_{\mathrm{th}} = 125\,\mathrm{mA}$)

in quadrature. The second $1/f$ segment at frequency offsets higher than $10\,\mathrm{kHz}$ is less steep, but still definitely sloped downward. This specific slope is common to all high-Q hybrid lasers. At $100\,\mathrm{MHz}$, commercial radio interferes with the spectrum and the response of the interferometer rolls off at higher frequency offsets, limiting the useful range of the measurement.

Noise from spontaneous emission alone should result in a flat, "white" frequency spectrum, which is not observed in the data for these lasers. Only an upper bound can be placed on the white frequency noise power spectral density. The upper bound is taken to be the value measured at offset frequencies just less than $100\,\mathrm{MHz}$.

This value of S_f can be converted to a "spontaneous emission linewidth" (due to spontaneous emission only) by using equation 2.75, providing a number that is easily compared to other lasers. The narrowest-linewidth high-Q hybrid laser has $S_f < 3 \times 10^3\,\mathrm{Hz^2\,Hz^{-1}}$, and therefore has a "spontaneous emission linewidth" of, at most, $18\,\mathrm{kHz}$.

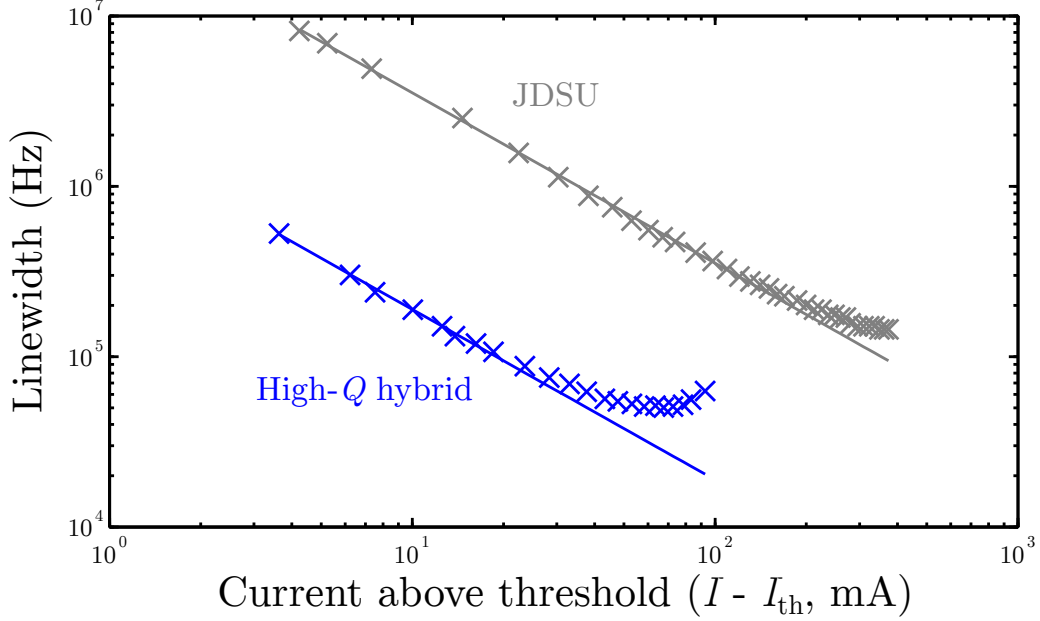The linewidth of the laser also has a $q/(I - I_{\mathrm{th}})$ dependence according to equa-

Figure 4.9: Linewidth as a function of pump current above threshold for a high-Q hybrid laser and the control JDSU laser. Crosses are experimental data, while the solid lines are calculated fits to $A(I - I_{th})^{-1}$. (Device ID HQhL1 Ch1 B5 S1 D11, $\lambda \approx 1560\,\mathrm{nm}$)

tion 2.79. Figure 4.9 shows the linewidth of a high-Q hybrid laser compared to a commercially-available laser used as a control (see appendix B.1 for details of the JDSU control laser). The high-Q hybrid laser has a linewidth 20 times narrower than the control laser at the same pump current above threshold.

Figure 4.10 presents the calculated "spontaneous emission linewidths" for each of the high-Q hybrid lasers tested.

4.3 Conclusions

Fabricated high-Q hybrid lasers were measured to have "spontaneous emission linewidths" narrower than $18\,\mathrm{kHz}$. These linewidths are much smaller than those measured for comparable monolithic semiconductor lasers (see competitors listed in section 3.1.1).

The high-Q hybrid lasers described in this chapter do have some downsides, though, and there is substantial room for improvement. Notably:
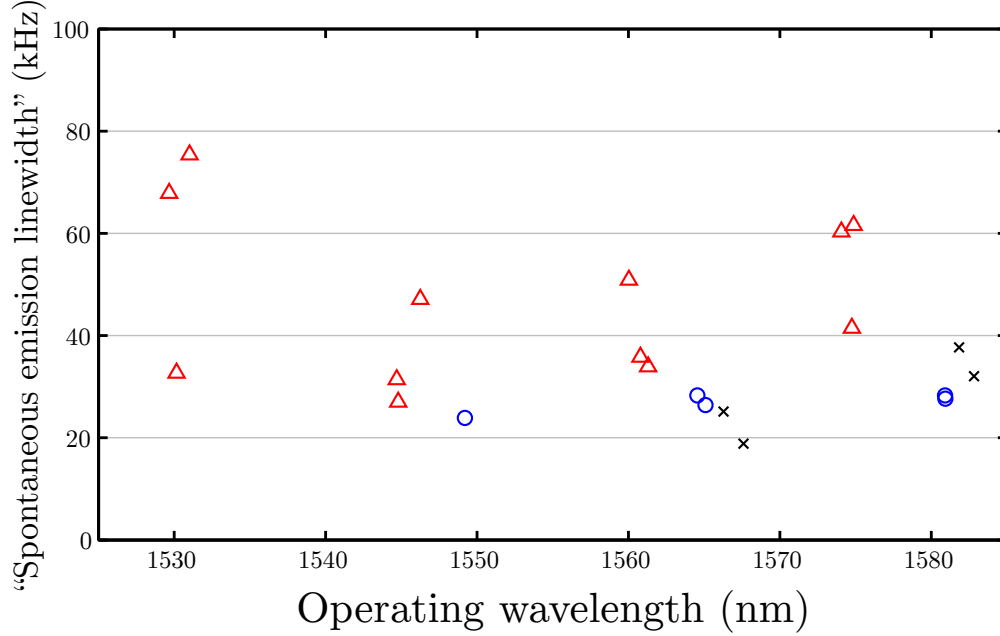
Figure 4.10: Calculated "spontaneous emission linewidths" of all measured high-Q hybrid lasers. Different markers indicate devices from different chips and cleaved bars which may have experienced different processing conditions. (Red triangles: Bar ID HQhL1 Ch1 B5 S1; blue circles: Bar ID HQhL1 Ch2 B5 S3; black crosses: Bar ID HQhL1 Ch2 B5 S2)

1. The confinement in the lossy III-V region is still high ($\Gamma_{\text{III-V}} = 18\%$). The remarkable consistency observed between different measured devices indicates that threshold and noise are being limited by absorption in III-V instead of fabrication imperfections. The spacer laser, described in chapter 5, pushes $\Gamma_{\text{III-V}}$ to its lower limit.

2. The threshold current needed to reach the lasing threshold is dominated by the transparency current. Reducing the number of quantum wells in the active region should reduce the threshold carrier density, thereby further reducing spontaneous emission into the mode without modal engineering.

3. The thick buried oxide layer, necessary for optical confinement in silicon, causes poor heat sinking from the active region. Because of heating, high-Q hybrid lasers are restricted to operating below about $5 \times I_{\text{th}}$, a rather low number. Flip-chip bonding of the III-V side to a heat sink may improve the performance.

Chapter 5

Spacer lasers

Experimental results for modal engineering

Spacer lasers introduce a low-index "spacer" layer between silicon and III-V, causing a controlled removal of optical energy from the lossy III-V material via modal engineering. Increasing the thickness of the spacer laser will reduce modal confinement in III-V ($\Gamma_{\text{III-V}}$) to the extreme where optical absorption no longer limits the total cavity Q. Figure 5.1 shows a cross-section of the spacer cavity.

Significant results from this chapter include

1. Simulation predicts that the modal engineering transformation used to make spacer lasers may reduce lossy confinement ($\Gamma_{\text{III-V}}$) by a factor of 20 times compared to the value calculated for no-spacer lasers presented in chapter 4. Under the modal engineering transformation, linewidth scales as $\Gamma_{\text{III-V}}^2$, therefore predicting a linewidth 400 times narrower for a spacer laser made with the
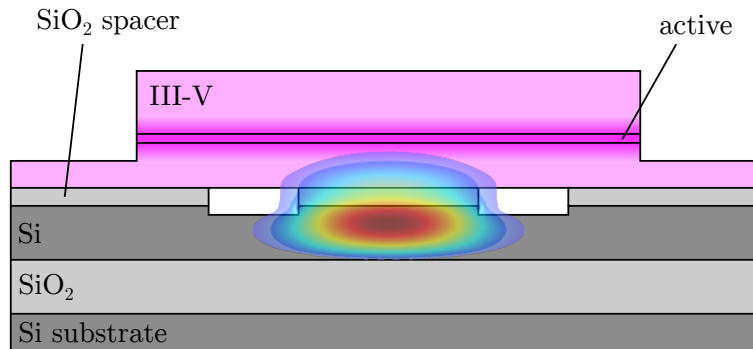

Figure 5.1: Cross-section of a spacer laser cavity, with the low-index oxide spacer located between the silicon and III-V regions.

optimum spacer thickness compared to the already-record high-Q hybrid laser linewidths (figure 5.7).

2. Fabricated spacer lasers have linewidths at least 5.4 times narrower than no-spacer lasers at the same pump current above threshold (figure 5.21). Spontaneous emission-limited linewidths are not found, so some other factor is limiting the measurement.

3. The best fabricated spacer lasers have the same threshold current as the non-spacer lasers (figure 5.9), as predicted by the theory.

Thanks to Christos Santis for the idea for the spacer implementation of modal engineering to reduce absorption losses.

5.1 Design and simulation

Numerical simulation must be used to verify the critical assumption made when describing modal engineering: that supermode theory predicts the ratio $\Gamma_{\text{III-V}}/\Gamma_{\text{act}}$ is constant under the modal engineering transformation. By calculating confinement factors as a function of spacer thickness, the parameters of spacer lasers (e.g., Q_{hybrid}, g_{th}, etc.) may be calculated as a function of spacer thickness.

5.1.1 Modal confinement

Supermode theory applied to coupled waveguides with very different propagation constants predicts that the eigenmode of the system is given by equation 3.23, reproduced here:

$$E_{\text{even}}(z) = \begin{pmatrix} \frac{i\kappa^*}{2\delta} \\ 1 \end{pmatrix} e^{-i\beta_{\text{Si}}z}, \tag{5.1}$$

for the case of $\delta < 0$ and $|\delta| \gg |\kappa|$. The various parameters are given by

$$\kappa \equiv -i\frac{\omega\epsilon_0}{4}\int_{-\infty}^{\infty} E_{\text{III-V}}^*(y)\,\Delta n_{\text{III-V}}^2\,E_{\text{Si}}(y)\,\mathrm{d}y, \tag{5.2}$$

$$2\delta \equiv \beta_{\text{Si}} - \beta_{\text{III-V}}, \tag{5.3}$$

where the subscripts "Si" and "III-V" refer to parameters for the individual, uncoupled silicon and III-V waveguides.

The spacer layer physically moves the individual III-V and silicon waveguides farther from each other. The propagation constant of each individual waveguide mode (β_{Si} and $\beta_{\text{III-V}}$) is unchanged by the presence of the spacer, but the coupling between the two waveguides (κ) changes. Coupling is defined in equation 5.2 as an integral of the two individual waveguide modes over the perturbation caused by the presence of one waveguide on the other waveguide [2, p.613]. The III-V perturbation is located in the exponentially decaying part of the silicon waveguide mode [2, p.112]. As the spacer thickness increases, that integral is taken over an exponentially weaker individual silicon waveguide mode.

The weighting of the individual III-V waveguide mode in the supermode is proportional to κ (equation 5.1), so both $\Gamma_{\text{III-V}}$ and Γ_{act} are expected to decrease exponentially with increasing spacer thickness.

Comsol (a commercial finite element solver) is used to calculate the optical mode for varying spacer thicknesses, using the exact 2D cross-section as input. The oxide spacer is included as in figure 5.1, with air holes above the waveguide trenches resulting from the trench etch step. The transverse waveguide parameters are given in table 5.1 (note that they are different from the high-Q hybrid laser parameters). The spacer consists of two layers: the grown oxide used to smooth the rough etched silicon sidewalls plus a previously-existing oxide. The total oxide spacer thickness, including the 50 nm grown oxide, ranges from 50 to 400 nm.

Figure 5.2 shows transverse modes for two spacer thicknesses, 50 nm and 200 nm. Note that much less of the mode overlaps with the lossy III-V and active MQW regions for the thicker spacer. Figure 5.3 shows a more obvious trend with spacer thickness

Parameter	Value
Waveguide rib width	$2.5\,\mu m$
Waveguide etch depth	$100\,nm$
Grown oxide thickness	$50\,nm$
Device layer thickness	$475\,nm$
Buried oxide thickness	$1\,\mu m$

Table 5.1: Transverse geometry parameters for spacer lasers.
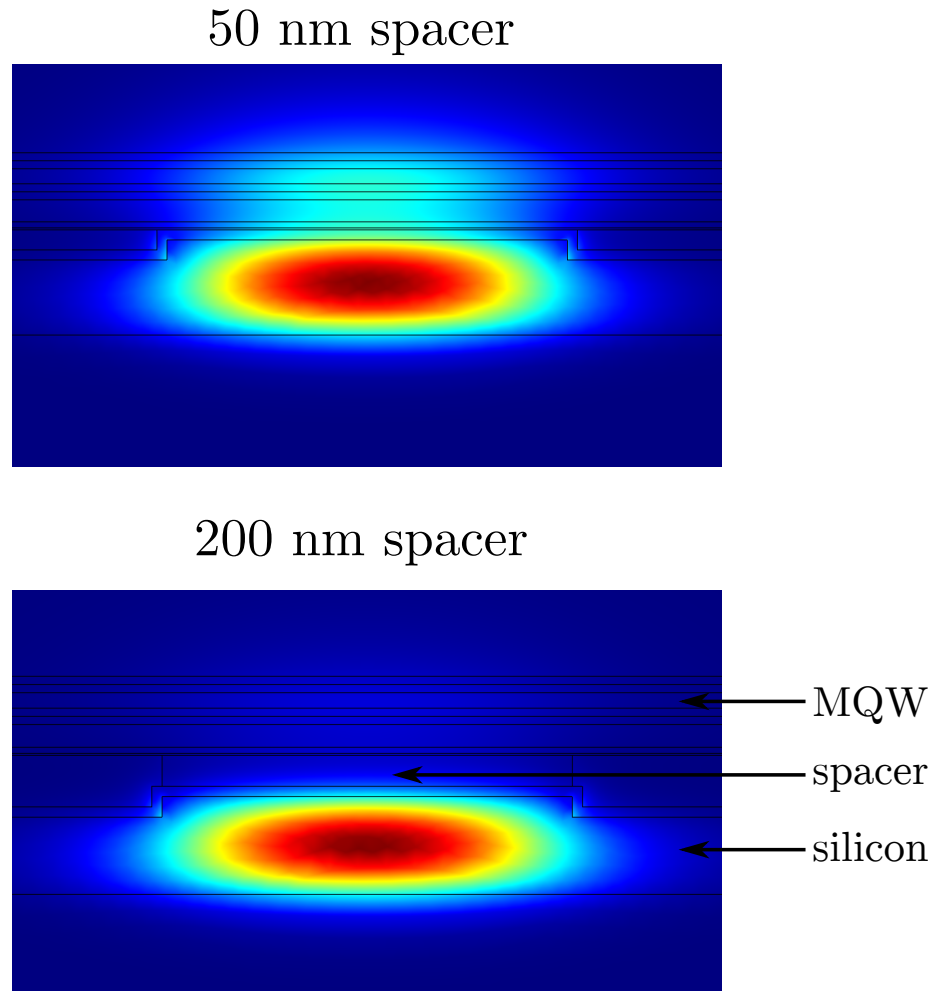
50 nm spacer

200 nm spacer

Figure 5.2: Transverse waveguide modes in the spacer laser, as solved for by Comsol. Spacer thicknesses include the $50\,nm$ grown thermal oxide.
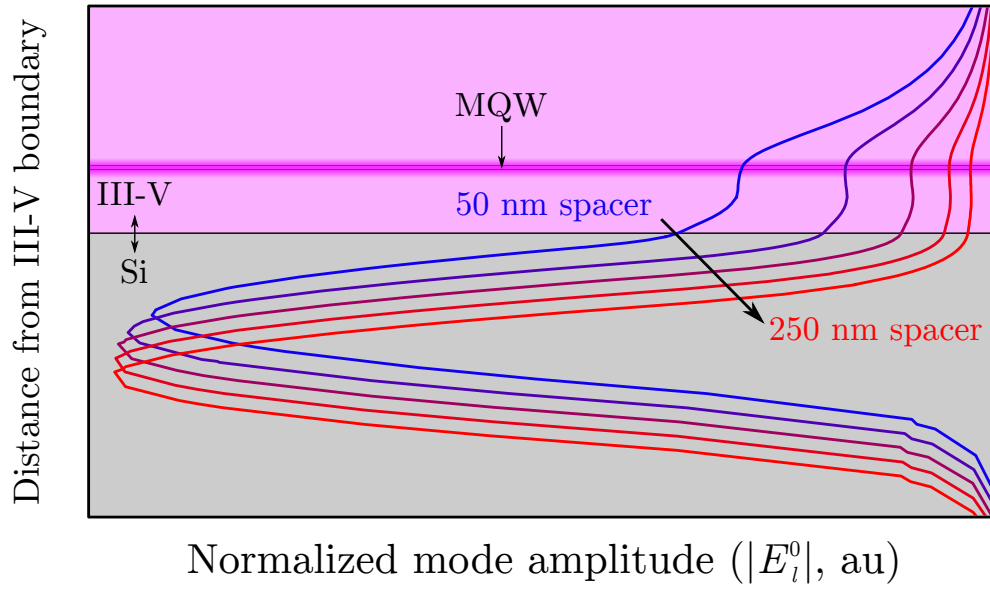
Figure 5.3: Vertical sections for the calculated modes with various spacer thicknesses. The sections are taken along the vertical center line of the waveguides. The III-V region to the right and the low-loss silicon and oxide regions to the left are marked.

by comparing sections taken from the vertical center line of the waveguides. Last, the confinement factors in lossy III-V and the active region are calculated numerically. Figure 5.4 shows how these vary with spacer thickness. Note that indeed both confinement factors scale exponentially with increased spacer thickness and that the ratio between the two is constant with spacer thickness, as expected from supermode theory.

5.1.2 Total quality factor

The confinement factors as a function of spacer thickness that were calculated numerically in the previous section can be used to convert equation 3.24 from depending on $\Gamma_{\text{III-V}}$ to depending on spacer thickness. Figure 5.5 shows how Q_{hybrid} depends on the spacer thickness.

The spacer thickness at which III-V absorption loss is equal to all other sources of loss is a critical thickness (t_{crit}). Thinner spacers have Q_{hybrid} limited by absorption in III-V and thicker spacers have Q_{hybrid} limited by Q_{passive}. The critical spacer thickness
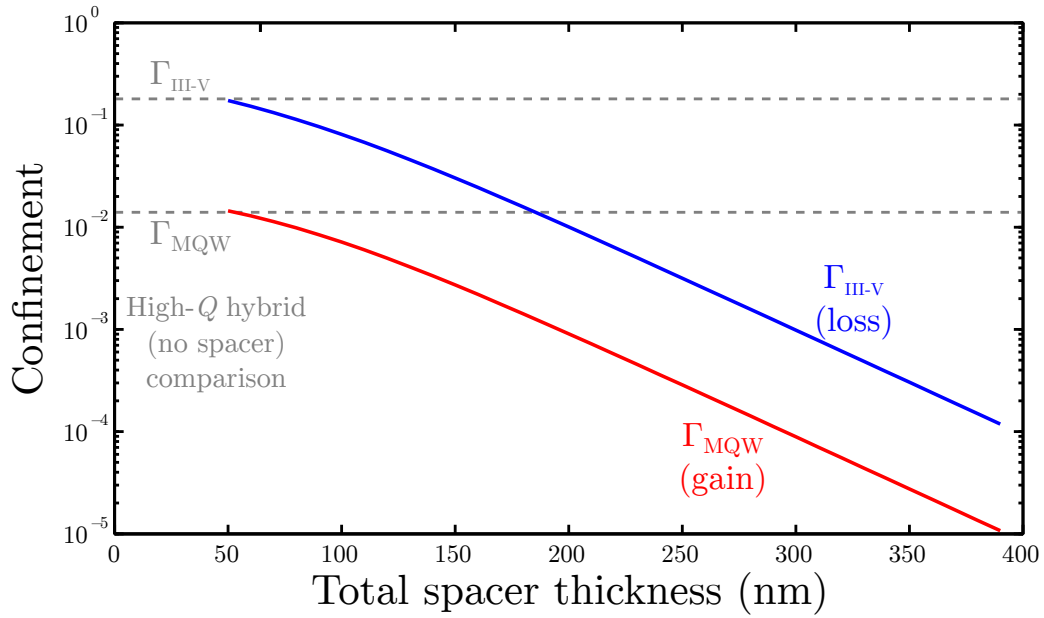
Figure 5.4: Calculated confinement factors for lossy III-V and the active region, as solved for in Comsol.
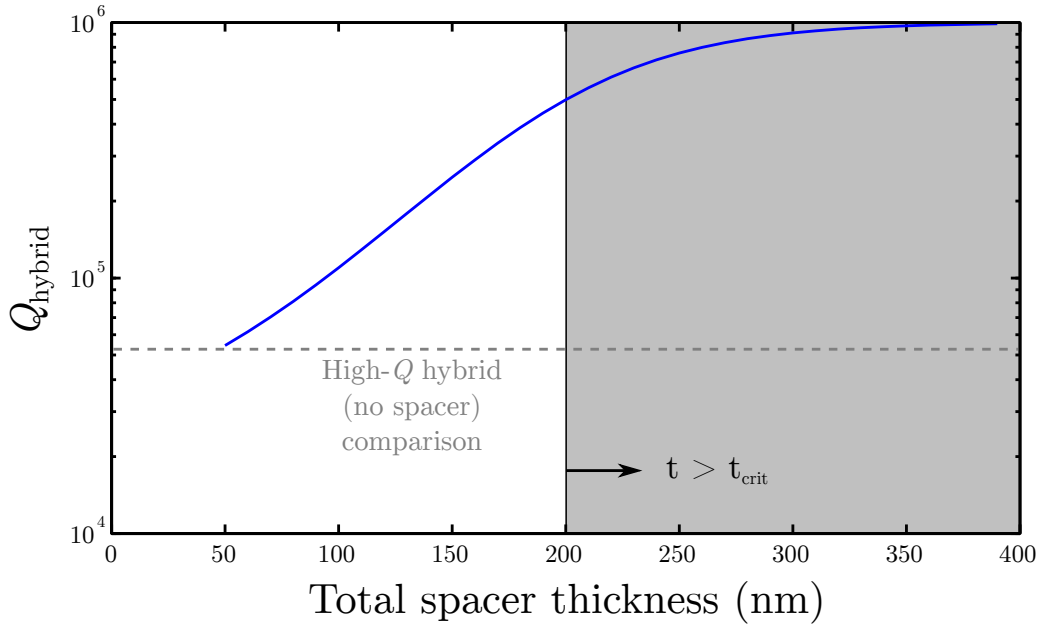

Figure 5.5: The total Q of the hybrid cavity increases with thicker spacer layers. The gray shaded area indicates thicknesses greater than the critical spacer thickness. The horizontal gray line represents Q_{hybrid} in high-Q hybrid lasers and is provided for comparison to spacer lasers. Assumptions: $Q_{III-V} = 10k$, $Q_{Si} = 1M$, and confinement factors taken from the numerical simulation.
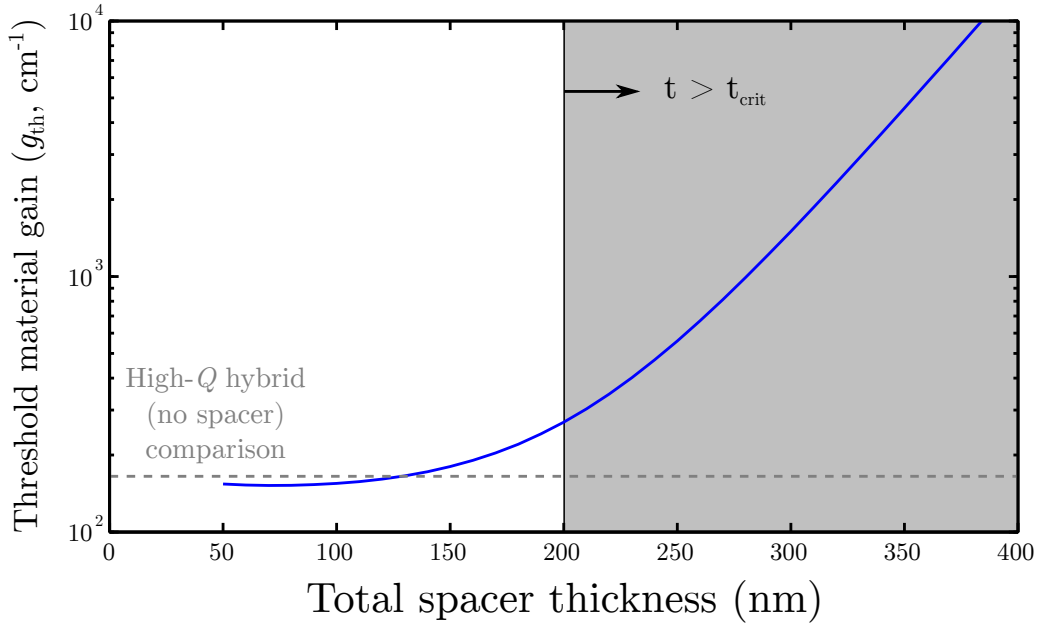
Figure 5.6: Threshold material gain in a spacer laser. Assumptions: $Q_{\text{III-V}} = 10\text{k}$, $Q_{\text{Si}} = 1\text{M}$, and confinement factors taken from the numerical simulation.

is approximately $200\,\text{nm}$ for this design.

The modal engineering used to create spacer lasers reduces $\Gamma_{\text{III-V}}$ compared to high-Q hybrid lasers which have no spacer, thereby increasing Q_{hybrid}. The total Q of the old high-Q hybrid lasers is provided as a reference in the figure. A spacer laser with the critical spacer thickness would have a total Q nearly 10 times higher than the high-Q hybrid lasers!

5.1.3 Threshold gain

The threshold material gain of a laser undergoing the modal engineering transformation is given by equation 3.26. Figure 5.6 uses the calculated confinement factors in spacer lasers to show threshold material gain as a function of spacer thickness. This figure indicates that Q_{hybrid} can be increased by 10 times compared to the old high-Q hybrid value with no spacer without changing the material gain required to reach threshold.
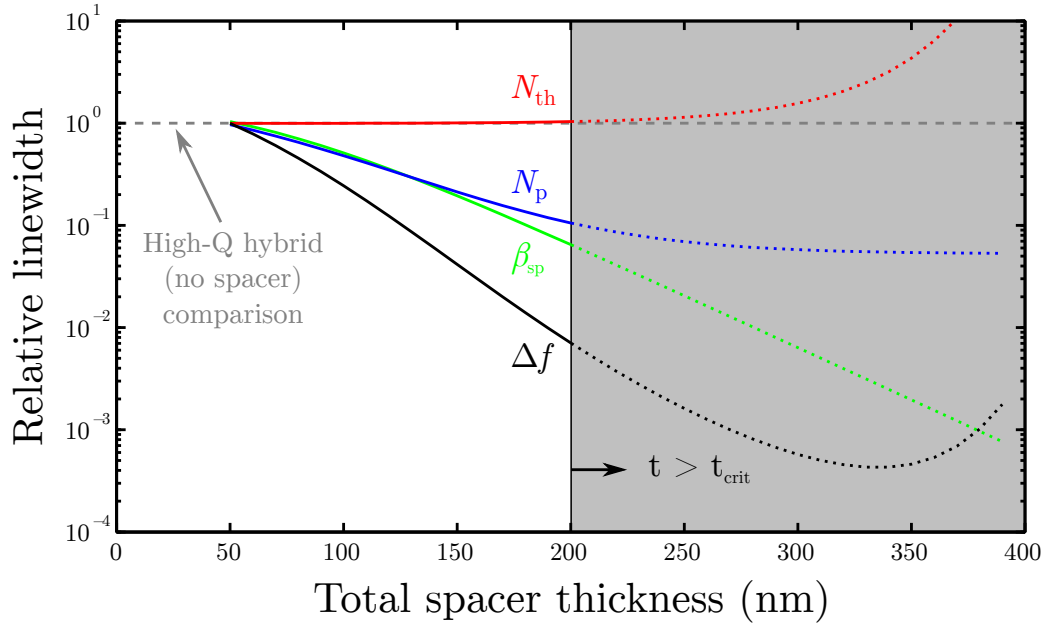
Figure 5.7: Calculated linewidth of a spacer laser. The linewidth is normalized to a no-spacer presented in chapter 4. The various components of the relative linewidth are plotted as colored lines and the product of these components gives the linewidth (Δf), plotted in black. This plot should not be trusted in the $t > t_{\mathrm{crit}}$ regime because changes in the inhomogenously-broadened spontaneous emission lineshape are not included. Assumptions: $Q_{\mathrm{III\text{-}V}} = 10\mathrm{k}$, $Q_{\mathrm{passive}} = 1\mathrm{M}$, confinement factors taken from the numerical simulation, $g_0 = 3 \times 10^3\,\mathrm{cm}^{-1}$, and $N_{\mathrm{tr}} = 5 \times 10^{12}\,\mathrm{cm}^{-2}$.

5.1.4 Linewidth

The linewidth of a spacer laser can be estimated by using the phenomenological approach outlined in section 3.3.4. Figure 5.7 shows the linewidth of spacer lasers relative to high-Q hybrid lasers which have no spacer.

5.1.5 Coupling to passive waveguides

A important benefit to using the spacer platform is that storing much of the modal energy in low-loss silicon minimizes coupling losses to passive silicon waveguides (i.e., without III-V attached). Though not directly beneficial to spacer lasers, this ability makes the spacer platform attractive for use in photonic integrated circuits.

Coupling losses are calculated by taking a two-dimensional overlap integral between the numerically calculated modes for the laser (with III-V) and the passive
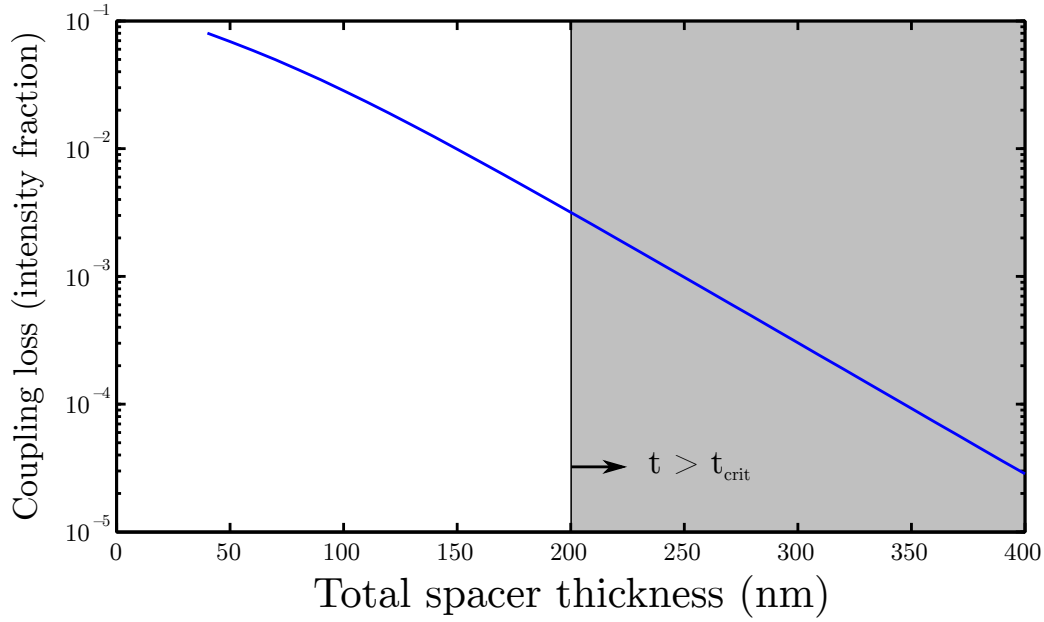
Figure 5.8: Coupling loss between a spacer laser (with III-V attached) and a passive silicon waveguide (with no III-V). The loss is applied to the intensity of the wave.

section (with air replacing III-V) [2, p.205]. Figure 5.8 shows the calculated coupling loss (intensity fraction) between the two segments as a function of spacer thickness. As expected, thicker spacers have less coupling loss because more of the mode resides in the low-loss silicon.

5.2 Fabrication and characterization

Spacer lasers were fabricated with three different spacer thicknesses. Important parameters can be found in table 5.2. The critical spacer thickness is about 200 nm. The maximum fabricated spacer thickness of 200 nm is about the critical thickness, so it is expected to have mildly increased threshold currents if all of the model parameters are correct.

The oxide spacer layer presents some difficult fabrication challenges. The thickest desired spacer dimension is comparable to the grating period, so the oxide spacer can't be grown without seriously changing the grating. Instead, most of the oxide spacer is present before the grating is etched. The waveguide and grating are defined

Parameter	Value
Spacer thickness (total)	$\{100, 150, 200\}$ nm
Q_{passive} (assumed)	1M
Quadratic well depth (V)	$\{100\,\text{GHz}, 120\,\text{GHz}\}$
Number of defect holes (N_{d})	999
Number of mirror holes on each side (N_{m})	$\{1400, 1600, 1800, 2000\}$
Period (Λ)	$\{240, 242.5, 245\}$ nm
Waveguide rib width	$2.5\,\mu\text{m}$
Waveguide etch depth	100 nm into silicon
Grown oxide thickness	50 nm
Device layer thickness	475 nm
Buried oxide thickness	$1\,\mu\text{m}$

Table 5.2: Nominal parameters used to fabricate spacer lasers.

by lithography on top of the oxide spacer and etched. The increased etch depth and area differences between the waveguide trench and the tiny grating holes means very different aspect ratios for the different desired features. Plasma etch rate typically depends on aspect ratio, so the waveguide trenches will etch faster than the grating holes [72–74]. Therefore, the waveguide trench etch depth has been increased from 50 nm in high-Q hybrid laser to 100 nm in spacer lasers in order to make sure the etched grating holes reach the silicon.

5.2.1 Threshold and power output

Threshold current density is expected to be the same in spacer lasers with spacer thickness less than the critical thickness of 200 nm. Figure 5.9 shows a scatter plot of thresholds for the fabricated spacer lasers, which have approximately the same cross-sectional area as the high-Q hybrid lasers with no spacer presented in chapter 4. Spacer lasers show significantly more threshold variation compared to the high-Q hybrid lasers, indicating that fabrication imperfections more strongly affect spacer lasers. This behavior is expected as Q_{passive} is a critical parameter in modal engineering theory, and it is sensitive to fabrication defects. The lowest-threshold spacer lasers have thresholds similar to the high-Q hybrid laser which have no spacer. Presumably, these low-threshold spacer lasers have the highest Q_{passive} values.
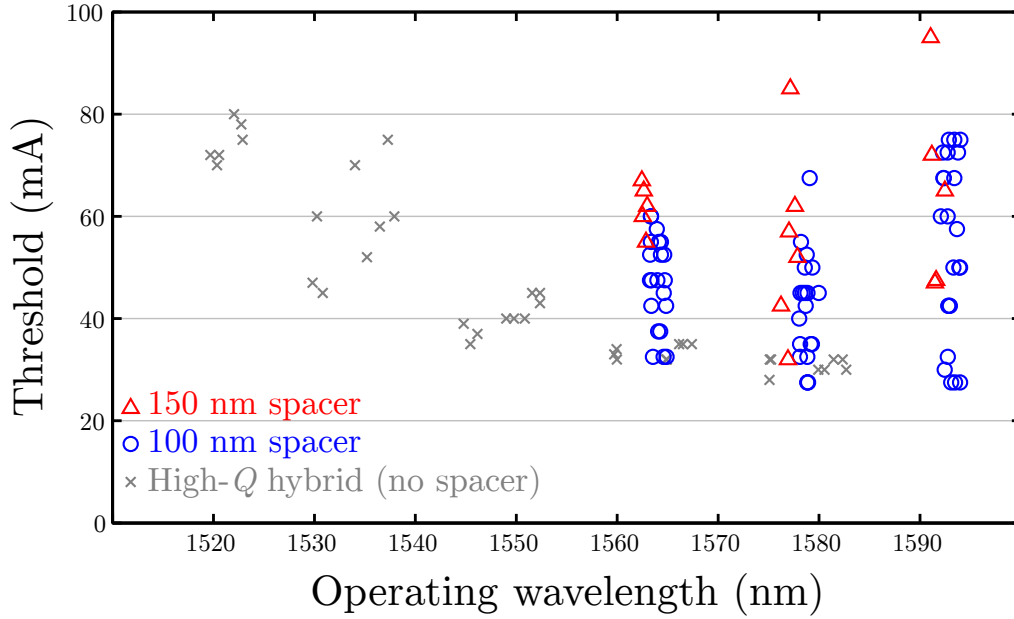
Figure 5.9: Scatter plot of threshold current in hybrid Si/III-V lasers with different spacer thicknesses. "High-Q hybrid" refers to the data presented in chapter 4. Wavelength values for each data point have been jittered slightly to separate duplicates. (Stage temperature 20 °C)

Figure 5.10 shows CW LI curves for a 100 nm spacer laser with varying stage temperature. This laser bar was attached to a temperature-controlled copper block with thermal paste. A maximum power output of nearly 4 mW was observed at a pump current of 300 mA and a stage temperature of 15 °C. Lasing was observed up to a stage temperature of 85 °C. No thermal rolloff is observed for the cooler stage temperatures, but measurements were limited to pump currents less than 300 mA to protect the laser bar. No mode hops were observed.

Spacer lasers have the same active region area as high-Q hybrid lasers, so they also have threshold current densities of less than $400\,\mathrm{kA\,cm^{-2}}$ (assuming uniform current density).

Figure 5.11 shows CW LI curves for a 150 nm spacer laser with varying stage temperature. This laser bar was die bonded to a C-mount with indium-based solder. In the past, thermal paste and die bonding have produced similar results for other lasers, so these LI curves can be compared to the LI curves for the 100 nm spacer laser accurately. These LI curves show thermal rolloff, indicating that the thicker spacer
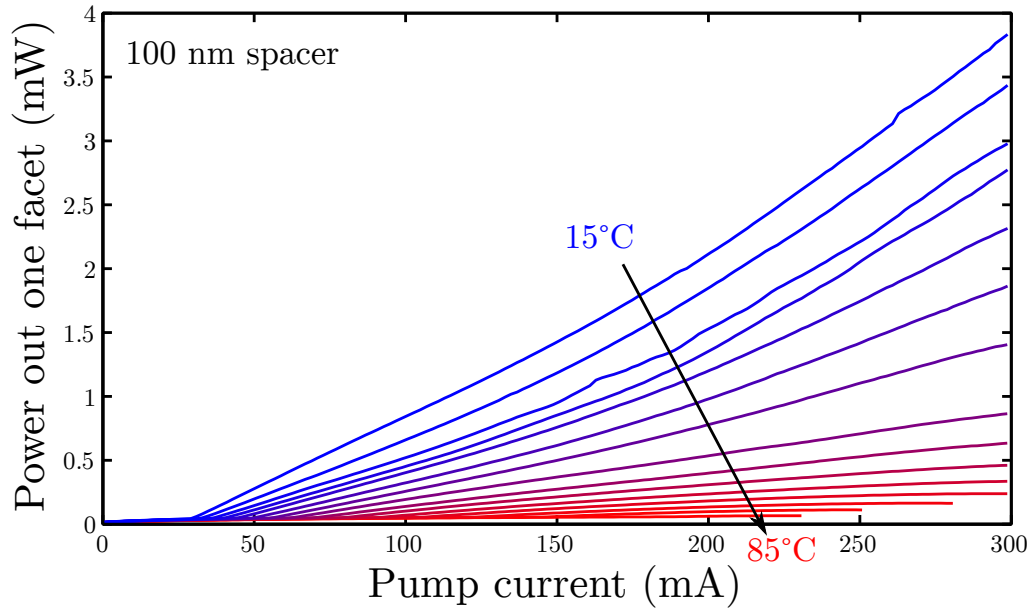
Figure 5.10: LI curves for a 100 nm spacer laser with varying stage temperature. Light is collected from one facet with an integrating sphere. (Device ID: Spacer100 B1 S2 D13, $\lambda \approx 1563$ nm)
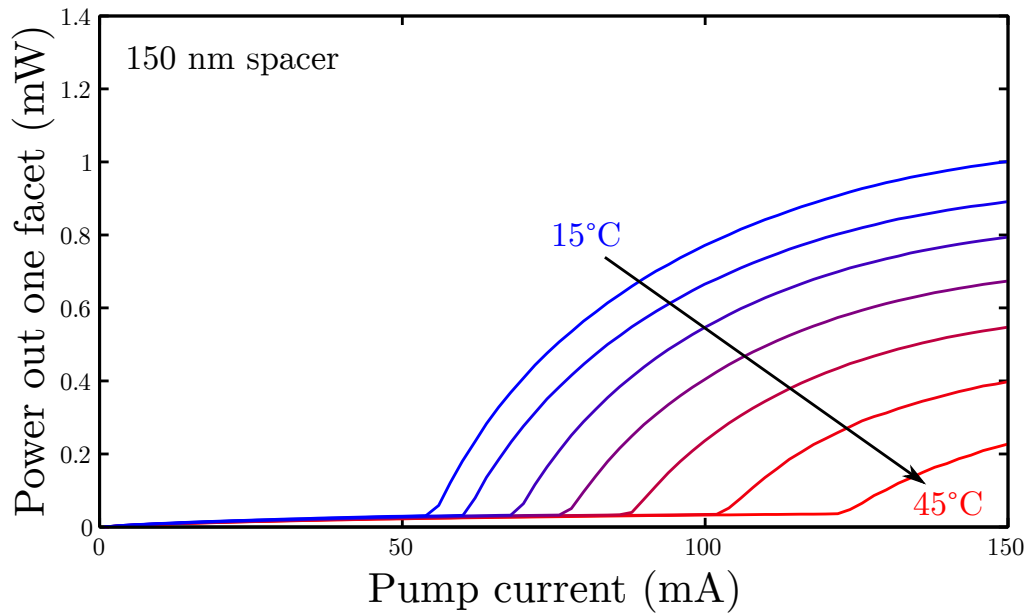

Figure 5.11: LI curves for a 150 nm spacer laser with varying stage temperature. Light is collected from one facet with an integrating sphere. (Device ID: Spacer150 B1 S2 D19, $\lambda \approx 1562$ nm)

degrades thermal performance.

None of the lasers fabricated with a 200 nm spacer layer lased. The theoretical model presented at the beginning of this chapter predicts that the critical spacer thickness is about 200 nm. Threshold is expected to increase for spacers thicker than the critical thickness, so the fact that none of these lasers worked means that either the assumed value for Q_{passive} of 1M is too optimistic or active confinement is less than the simulated value.

Temperature dependence

From empirical observations of semiconductor lasers, threshold increases exponentially with temperature because excited carriers will span a larger energy range at higher temperatures, providing less gain at each frequency [4, p.81]. The relationship can be modeled as

$$I_{\text{th}} = I_0 \ e^{T/T_0}, \tag{5.4}$$

where I_0 and T_0 are the characteristic threshold current and temperature, respectively. A laser with a low characteristic temperature is sensitive to temperature.

Figure 5.12 shows a fit to this characteristic temperature for spacer lasers with 100 and 150 nm spacer thicknesses. As expected, the laser with the thicker spacer has a lower characteristic temperature, suggesting that the thermally insulating SiO_2 spacer degrades performance.

5.2.2   IV performance

IV curves for the spacer lasers are given in figure 5.13. The diode has a turn-on voltage of about 0.7 V. The slope of the IV curve after the diode has turned on gives the series resistance of the device. Both spacer lasers have a series resistance of about 5 Ω, compared to 10 Ω in the no-spacer laser. This value is a little high for diode lasers, and it may be explained by the thin n-contact layer through which the current must pass. Additionally, imperfect optimization of the contact resistance may have led to increased series resistance.
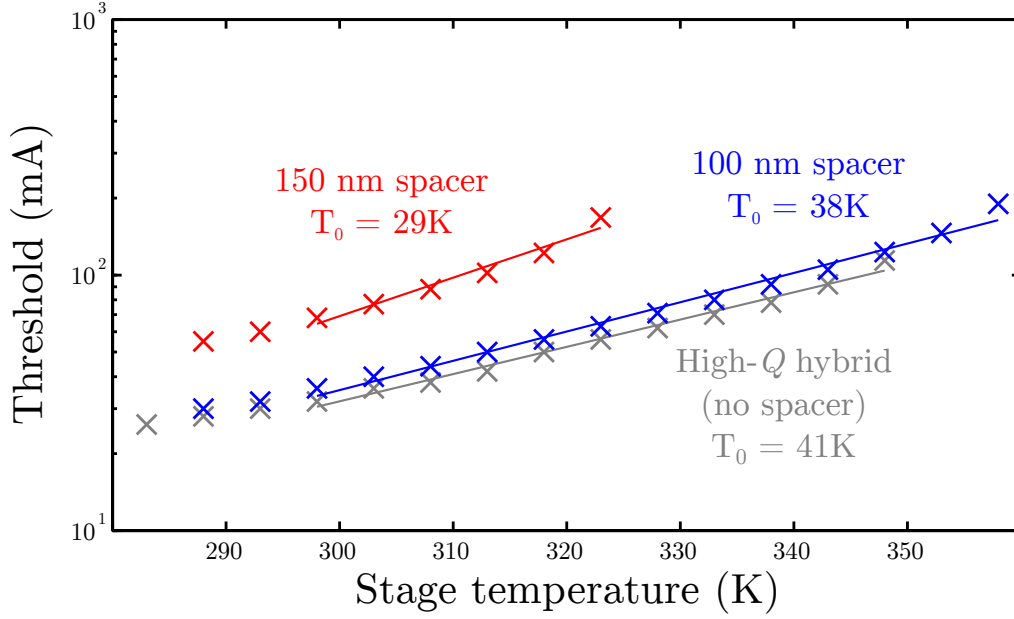
Figure 5.12: Laser threshold at varying stage temperature. The data is fitted to calculate a characteristic temperature for each device. Stage temperatures below 25 °C are excluded from the fit to avoid the effect of transparency in the data. (Device IDs: Spacer100 B1 S2 D13, $\lambda \approx 1563$ nm; Spacer150 B1 S2 D19, $\lambda \approx 1562$ nm; HQhL1 Ch1 B5 S1 D15, $\lambda \approx 1575$ nm)
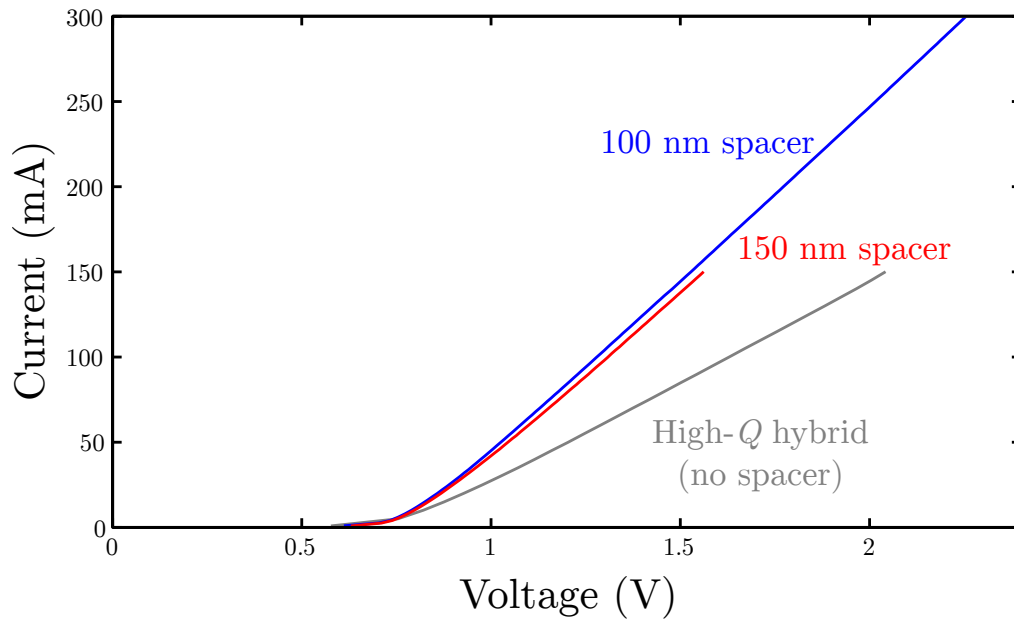

Figure 5.13: IV performance of spacer lasers compared to the no-spacer laser. Both spacer lasers have a series resistance of $5\,\Omega$, while the no-spacer laser has a series resistance of $10\,\Omega$. (Stage temperature 20 °C. Device IDs: Spacer100 B1 S2 D13, $\lambda \approx 1563$ nm; Spacer150 B1 S2 D19, $\lambda \approx 1562$ nm; HQhL1 Ch1 B5 S1 D8, $\lambda \approx 1546$ nm)
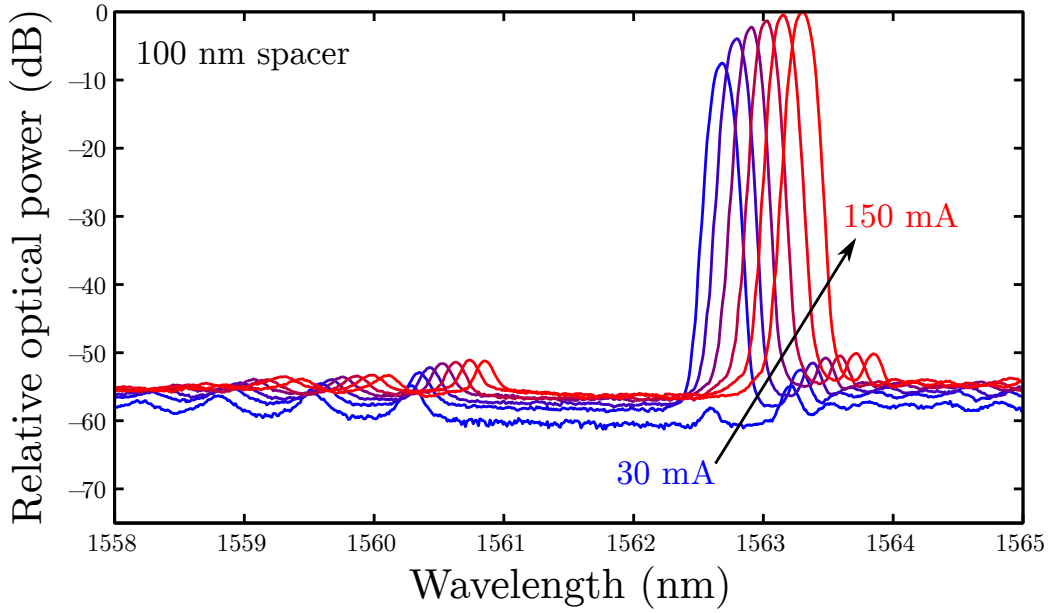
Figure 5.14: Optical spectrum of a 100 nm spacer laser at different pump currents. (Stage temperature 20 °C. Device ID: Spacer100 B1 S2 D13, $\lambda \approx 1563$ nm)

5.2.3 Optical spectrum and sidemode suppression

Optical spectra for the selected lasers are taken with an optical spectrum analyzer. They show good qualitative agreement with the passive spectrum simulated in appendix A (figure A.10).

Figure 5.14 shows the optical spectrum of the 100 nm spacer laser at varying pump currents, from below threshold up to 150 mA. Figure 5.15 shows the calculated sidemode suppression ratio from these optical spectra. A bit strangely, the strongest sidemode is seen on the red side of the bandgap, next to the lasing mode. This mode is 57 GHz away from the lasing mode, so it may be a second-order mode in the 120 GHz deep photonic well. Compared to the fundamental high-Q mode, a higher-order mode will experience much more loss through the grating mirrors and therefore will be unlikely to lase. The measured intensity of this mode may also be an artifact of being near the strong, fundamental mode. In any case, sidemode suppression ratios greater than 50 dB are observed at modest pump currents.

Figure 5.16 shows the optical spectrum of the 150 nm spacer laser at varying pump currents. This laser has a low output power, causing the sidemodes to be lost in the
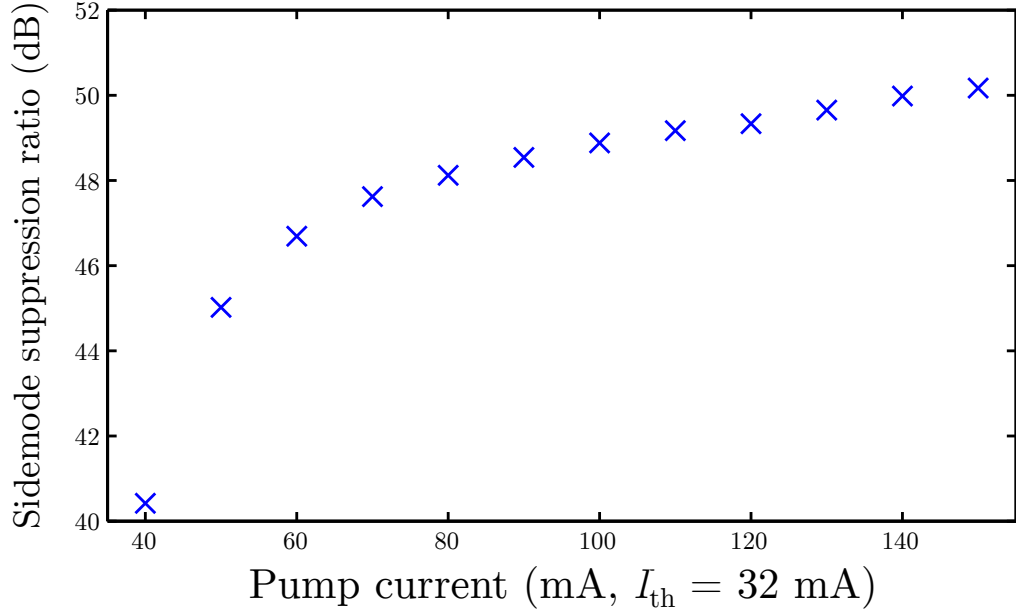
Figure 5.15: Sidemode suppression in a 100 nm spacer laser, calculated from optical spectra taken with a resolution bandwidth of 100 pm. (Device ID: Spacer100 B1 S2 D13, $\lambda \approx 1563$ nm)
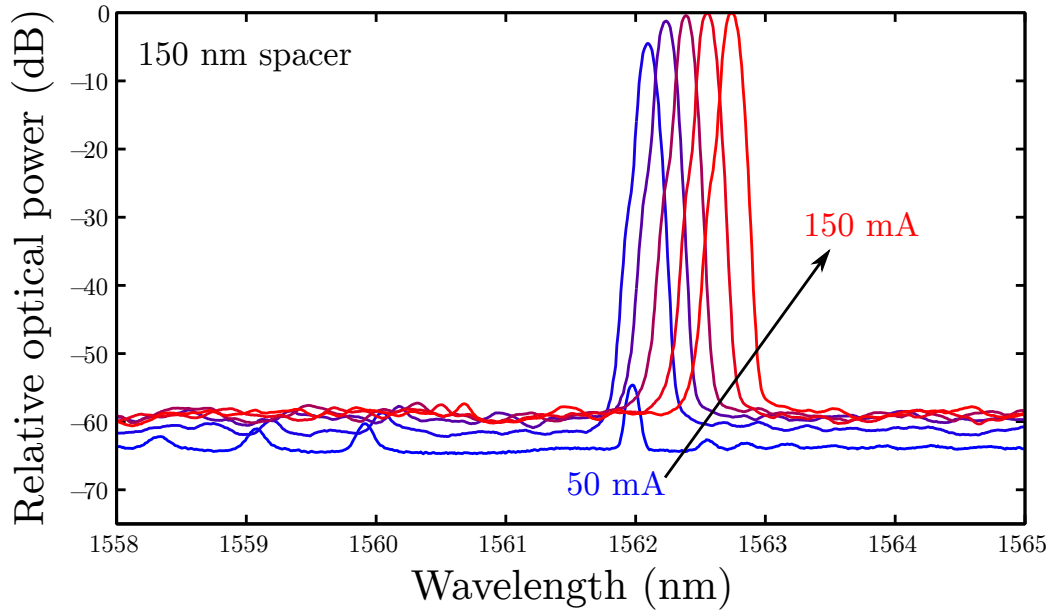

Figure 5.16: Optical spectrum of a 150 nm spacer laser at different pump currents. (Stage temperature 20 °C. Device ID: Spacer150 B1 S2 D19, $\lambda \approx 1562$ nm)
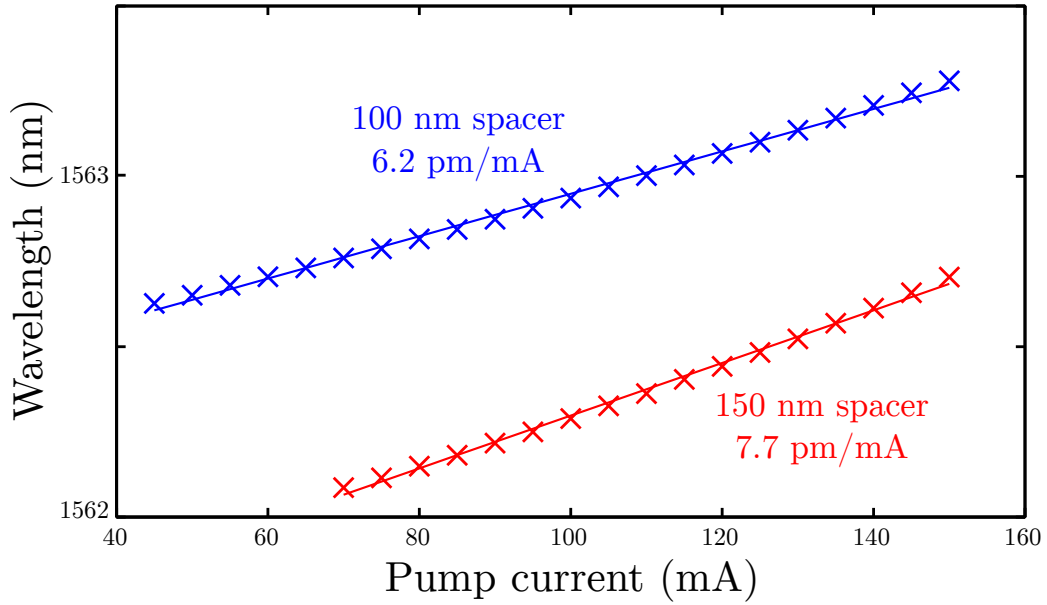
Figure 5.17: Laser wavelength measured by a wavemeter for varying pump current. Measurements are taken after the temperature controller has time to stabilize. (Stage temperature 20 °C. Device IDs: Spacer100 B1 S2 D13, $\lambda \approx 1563$ nm; Spacer150 B1 S2 D19, $\lambda \approx 1562$ nm; HQhL1 Ch1 B5 S2 D15)

noise of the OSA. Sidemode suppression is greater than 55 dB.

5.2.4   Wavelength tuning

Wavelength tuning by the thermo-optic effect is measured both as a function of pump current and stage temperature. Figure 5.17 shows tuning as a function of DC pump (i.e., not a fast sweep). The device with the thicker SiO_2 spacer tunes slightly more with pump current, further indicating that heating is greater for thicker spacers.

Figure 5.18 shows tuning as a function of stage temperature. The device with the thicker SiO_2 spacer also tunes slightly more with stage temperature, probably indicating worse heat sinking.

5.2.5   Frequency noise PSD and linewidth

The frequency noise power spectrum of the spacer lasers is measured with the experimental setup described in section B.1. Figure 5.19 shows the frequency noise PSD for
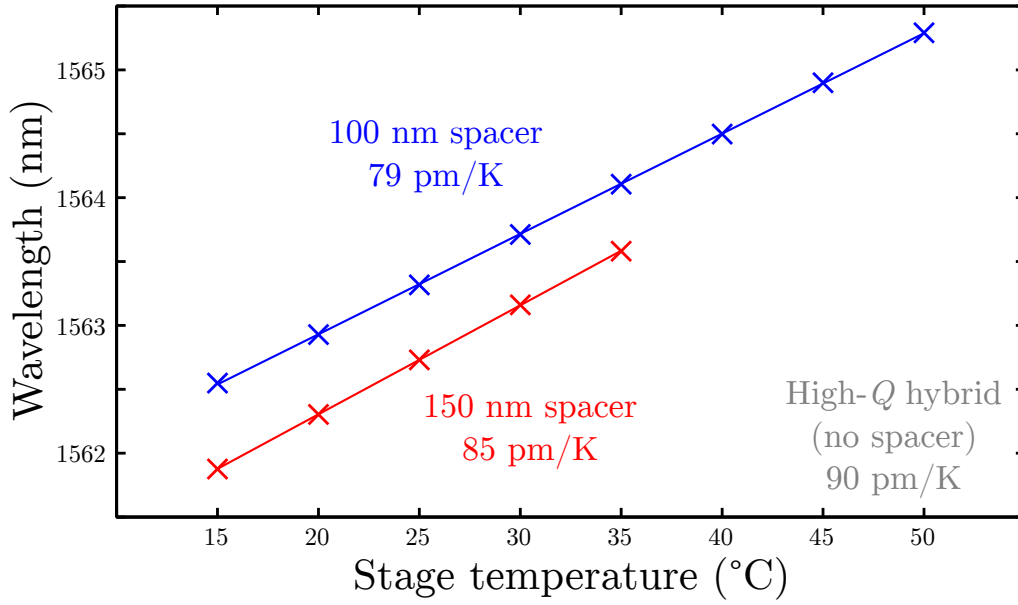
Figure 5.18: Laser wavelength measured by a wavemeter for varying stage temperature. Measurements are taken after the temperature controller has time to stabilize. (Pump 100 mA. Device IDs: Spacer100 B1 S2 D13, $\lambda \approx 1563$ nm; Spacer150 B1 S2 D19, $\lambda \approx 1562$ nm; HQhL1 Ch1 B5 S2 D15, $\lambda \approx 1575$ nm)

the lowest-noise 100 nm spacer laser. The spontaneous emission contribution to laser linewidth is expected to have a white frequency noise spectrum. The measurement shown here does not have a flat noise spectrum characteristic of white noise, so the lowest frequency noise PSD value is used to set an upper bound on the linewidth due to spontaneous emission using equation 2.75. This laser has a "spontaneous emission linewidth" narrower than 20 kHz at a pump current 45 mA above threshold.

Figure 5.20 shows the frequency noise PSD for the lowest-noise 150 nm spacer laser. This spectrum does not have a flat segment either, so an upper bound for the "spontaneous emission linewidth" is set at 16 kHz at a pump current 30 mA above threshold.

Figure 5.21 shows the upper bound on the "spontaneous emission linewidth" of these two spacer lasers compared to the no-spacer lasers presented in chapter 4. The linewidths of two no-spacer lasers are presented because the lowest-noise laser was physically damaged by the electrical probe before enough low-pump data points were taken. Increasing the pump level above threshold increases the number of stored

Figure 5.19: Frequency noise power spectral density for the lowest-noise 100 nm spacer laser. (Pump 80 mA; $I - I_{th} = 45$ mA. Device IDs: Spacer100 B1 S2 D13, $\lambda \approx 1563$ nm)

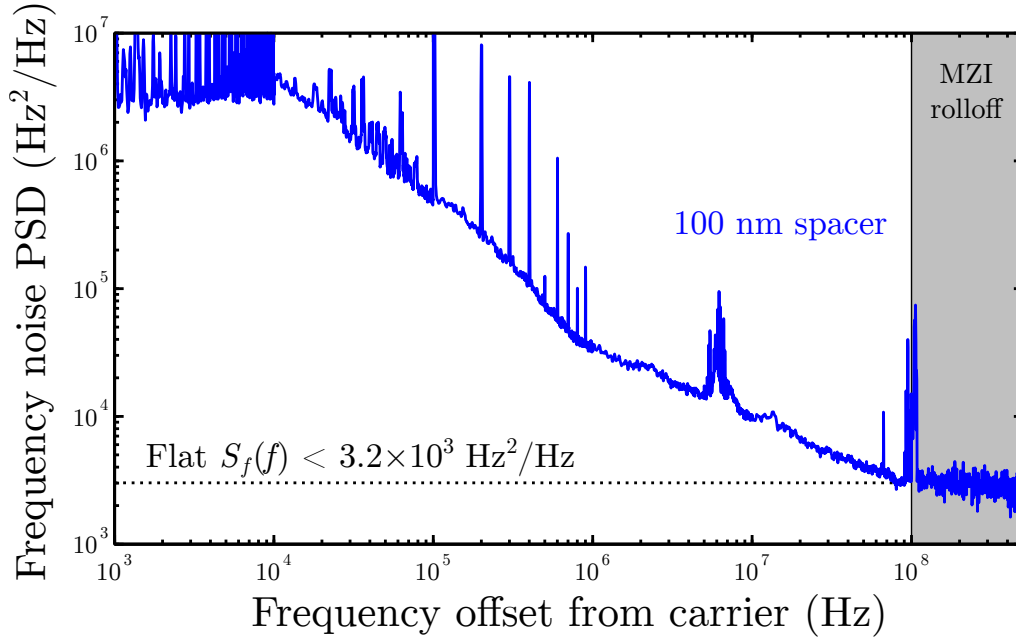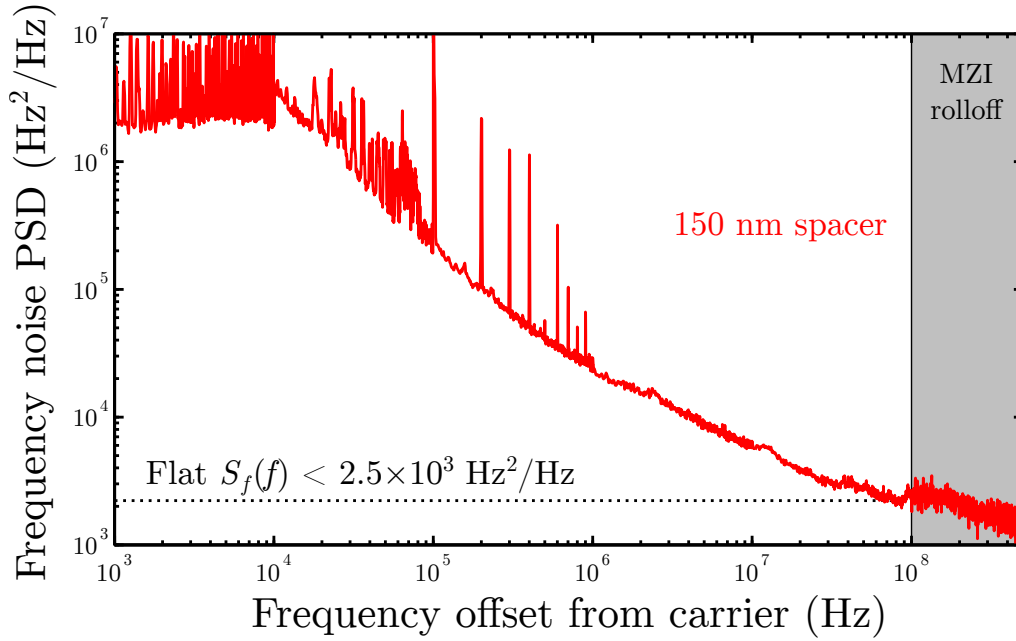Figure 5.20: Frequency noise power spectral density for the lowest-noise 150 nm spacer laser. (Pump 95 mA; $I - I_{th} = 30$ mA. Device ID: Spacer150 B1 S2 D19, $\lambda \approx 1562$ nm)
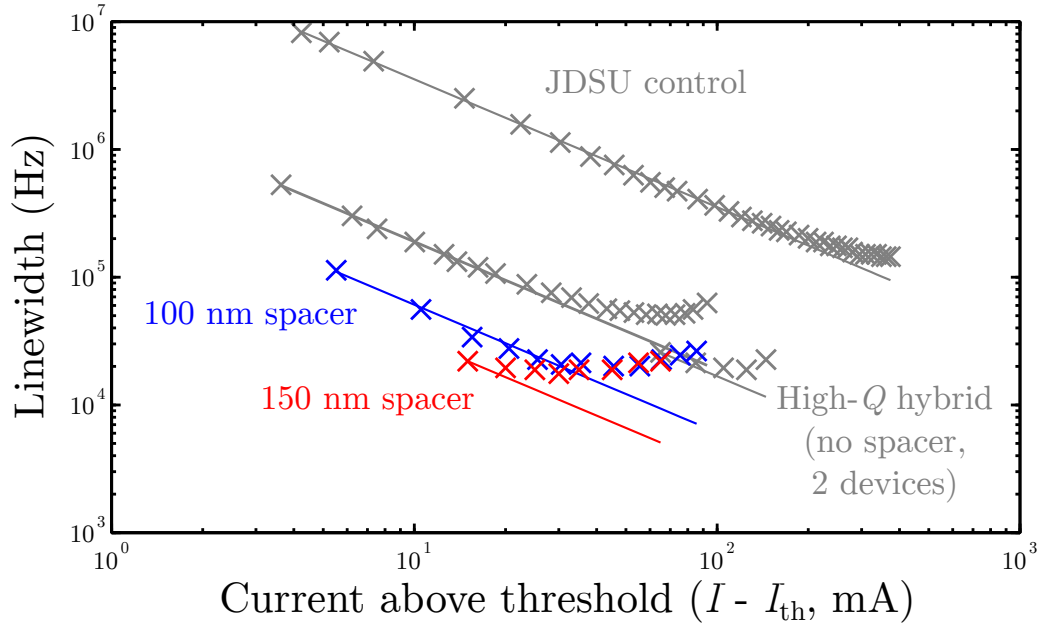
Figure 5.21: Upper bound on the "spontaneous emission linewidth" of various hybrid Si/III-V lasers as a function of pump current above threshold. Solid lines indicate best-fits to $A(I-I_{\text{th}})^{-1}$. Both the amplitude (A) and threshold current (I_{th}) are fitted, except for the narrower-linewidth no-spacer laser and $150\,\text{nm}$ spacer laser which don't have enough good data points at low pump currents to show the dependence. (Device IDs: Spacer100 B1 S2 D13, $\lambda \approx 1563\,\text{nm}$; Spacer150 B1 S2 D19, $\lambda \approx 1562\,\text{nm}$; HQhL1 Ch2 B5 S2 D10, $\lambda \approx 1567\,\text{nm}$; HQhL1 Ch1 B5 S1 D11, $\lambda \approx 1560\,\text{nm}$)

Spacer thickness (nm)	Measured linewidth (relative)	Predicted linewidth (relative)
0	1	1
100	1/2.9	1/4.0
150	< 1/5.4	1/25

Table 5.3: Relative linewidth of spacer lasers compared to the high-Q hybrid (no-spacer) laser, from both simulation and measurement. Linewidth values are taken at the same pump current above threshold.

photons (equation 2.65), leading to a $(I - I_{\text{th}})^{-1}$ dependence in the linewidth of the laser (equation 2.79). Thus, a fair comparison of two lasers should be made at the same pump level above threshold and the vertical distance between two of the fit lines in figure 5.21 reflects the difference due to μ/Q^2 between the two lasers.

Table 5.3 presents the linewidth of spacer lasers relative to the no-spacer laser. The 100 nm spacer laser has a linewidth 2.9 times narrower than the no-spacer lasers presented in chapter 4. The 150 nm spacer laser has a linewidth at least 1.8 times narrower than the 100 nm spacer laser, for a total improvement of at least 5.4 times compared to the no-spacer laser at the same pump current above threshold. A semiconductor DFB laser manufactured by JDS Uniphase is presented as a control (see section B.2). The thick spacer laser has a linewidth at least 110 times narrower than this already-narrow control laser at the same pump level above threshold.

While spacer lasers have narrower linewidths than the comparison lasers at the same pump current above threshold, the measured upper bound on linewidth at high pump currents is the same for all lasers. Section B.2 discusses the various calibration and control procedures used for the measurement. A fiber laser is measured to have more than an order of magnitude less frequency noise than the values discussed here, showing that the measurement setup is capable of measuring much narrower linewidths and that these measurements are valid upper bounds.

Figure 5.22 shows the minimum measured upper bound on the "spontaneous emission linewidth" for all hybrid Si/III-V lasers.
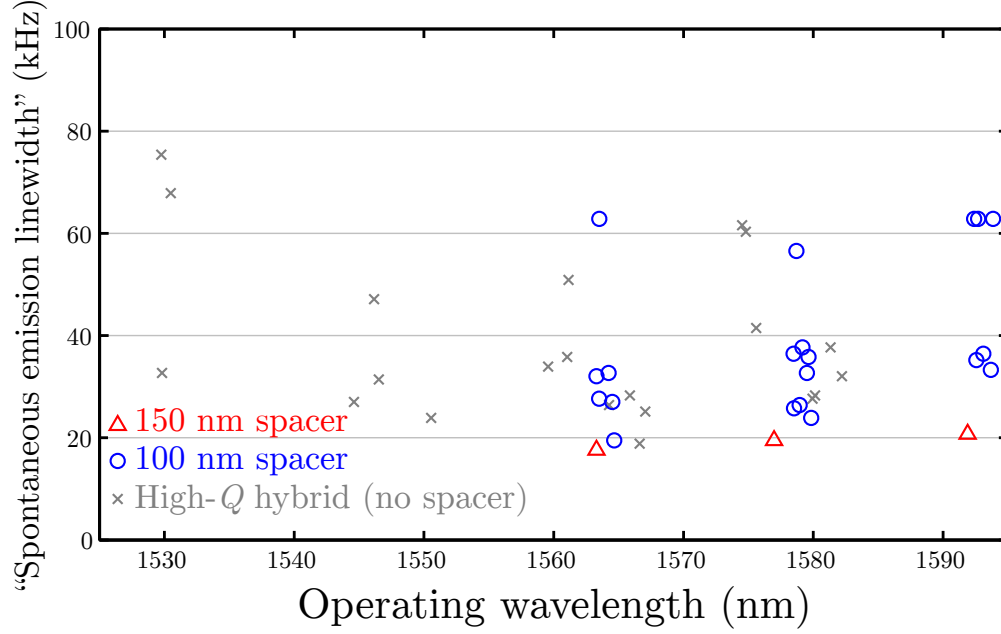
Figure 5.22: Minimum measured upper bounds on the "spontaneous emission line-width" of spacer lasers, with no-spacer lasers presented as a comparison. Wavelength values for each data point have been jittered slightly to separate duplicates. (Stage temperature $20\,°C$)

5.3   Conclusions

Fabricated spacer lasers exhibit many of the properties predicted by the theory:

1. Linewidths are more than 5.4 times narrower than the non-spacer lasers presented in chapter 4 at the same pump current above threshold, though linewidths limited by spontaneous emission are not found.

2. The lowest thresholds of thin-spacer lasers and non-spacer lasers are the same, even with 5 times less modal gain in the devices with 150 nm spacer.

3. Measured spacer laser properties show high variance, indicating that they are sensitive to fabrication defects because of the critical dependence on Q_{passive}. Lasers with thicker spacers have higher variance.

4. The addition of the SiO_2 spacer makes heat sinking even worse in these spacer lasers compared to non-spacer Si/III-V lasers. The p-side of these lasers should be mounted to a heat sink to greatly improve thermal performance.

It's unfortunate that the demonstrated linewidth narrowing in spacer lasers is less than the predicted value of up to 400 times compared to non-spacer Si/III-V lasers. However, there is hope left due to the fact that the values discussed in this chapter are only upper bounds on the "spontaneous emission linewidth". The smallest upper bound on linewidth is approximately the same for five different chips with three different spacer thicknesses fabricated in two different runs, hinting that a bigger effect is masking the true "spontaneous emission linewidth". Three likely candidates to explain the linewidth floor seen in hybrid Si/III-V lasers are apparent: (1) two-photon absorption leading to a saturation in Q_{hybrid}, (2) diffusion of heat or carriers due to spatial hole burning [75–79], and/or (3) thermal noise inducing refractive index fluctuations via the thermo-optic effect [80; 81]. Future work should include cryogenic testing of the lasers and replacing silicon with a material that has reduced or no two-photon absorption.

Chapter 6

Conclusions

6.1 Modal engineering

This thesis has presented modal engineering as the optimal way to decrease phase noise in lasers where optical losses are dominated by absorption near the active region. Modal engineering shifts modal energy away from the active region, reducing gain, loss, and the spontaneous emission rate by the same factor, thereby keeping threshold constant while decreasing linewidth.

Modal engineering was compared to the straightforward approach in which low-loss silicon replaces lossy III-V, reducing losses while keeping gain constant. The replacement transformation was found to suffer from diminishing returns because transparency sets a minimum amount of spontaneous emission into the mode. Modal engineering, by contrast, avoids this problem by reducing modal gain.

Modal engineering was demonstrated on the hybrid Si/III-V platform by introducing a low-index spacer layer to reduce the coupling between the silicon and III-V waveguides by physically moving them farther apart. These spacer lasers were shown to have narrower linewidths than non-spacer lasers at the same pump current above threshold. They also have similar thresholds as non-spacer lasers.

Modal engineering can be applied to any platform on which optical losses are dominated by absorption near the active region. All types of semiconductor lasers fit this profile now or will fit the profile as fabrication techniques improve. Furthermore, the spacer laser is only one implementation of modal engineering. Any method of varying

the coupling strength or phase detuning between two adjacent waveguides will change the fraction of the mode in each waveguide and can be used for modal engineering. For example, modal engineering could be used in two coplanar waveguides defined in the same semiconductor layer.

6.2 The hybrid Si/III-V platform

Hybrid Si/III-V de-couples electrical and optical performance, making it an exciting platform for future devices because it integrates materials good for making electronics and photonics on a single chip. The excellent fabrication quality in silicon determines the losses of the laser instead of the relatively poor fabrication quality in III-V materials. Many of the advances made in large-scale integration of silicon electronics will transfer to the hybrid Si/III-V platform.

Conveniently, modal engineering in Si/III-V moves the III-V farther from the silicon, meaning that each material will disturb the other less. Because nearly all of the light in a spacer laser is confined in silicon, coupling between active and passive photonic segments is effortless. Reflections from simply terminating the III-V will be very weak. Spacer lasers, therefore, can be integrated with a wide range of on-chip photonic devices.

Heterogeneous integration via wafer bonding is not limited to the silicon and InP/InGaAsP materials used in this thesis. Various semiconductor materials provide gain over a wide range of wavelengths, and a process could be developed to bond each to the amorphous SiO_2 spacer layer. Gain materials are not limited to quantum wells; in fact, hybrid Si/III-V lasers with quantum dots have been demonstrated [82] and may provide many advantages over quantum well material. Silicon is absorbing at shorter wavelengths, below about $1100\,\mathrm{nm}$, but it could be replaced with silicon nitride, for example, to make visible lasers. Magneto-optical materials can be integrated with silicon to create on-chip isolators [83–85] or birefringent materials can be integrated with silicon to make modulators [86–88]. Modal engineering is compatible with all of these methods and therefore could be used improve virtually any

semiconductor laser.

6.3   Future outlook

Modal engineering has immediate commercial potential as hybrid Si/III-V lasers are already sold in niche markets. Future research to narrow linewidths, on the other hand, may concentrate on extending the platform by integrating other electronic or photonic devices on-chip.

Electronic feedback to stabilize the phase of a laser will be essential to future narrow-linewidth lasers. Feedback can be provided by a high-Q cavity external to the laser [89] or by beating the laser against a narrower-linewidth master laser or against a delayed version of itself [90]. Hybrid Si/III-V offers the ability to integrate the optical and electrical components needed for these feedback techniques with a narrow-linewidth laser employing modal engineering.

Nonlinear optics require a laser source with very low phase noise in order for coherent interactions to build up. Modal engineering therefore can be used to create pumps for on-chip Brillouin lasers that could have linewidths orders of magnitude narrower than the values presented in this thesis [91–93].

Narrow linewidth lasers can be used to probe atomic frequency standards to reduce drift, leading to applications in chip-scale atomic clocks [94; 95].

Appendix A

High-Q single-mode resonator design

The noise theory presented in this thesis is valid for any resonator in which in the hybrid Si/III-V cavity losses are dominated by absorption in III-V. It is independent of any specific resonator design. The challenge of making all other sources of loss small is met by careful design of a high-Q silicon resonator.

Modegap waveguide resonators are chosen for the lasers made in this thesis because they can host a single longitudinal mode with very high Q. The quality factor of the passive resonator (Q_{passive}) is used as a metric for the upper bound on the amount of III-V that can be usefully replaced with silicon. Passive modegap resonators designed to be similar to the active laser resonator were fabricated and measured to have Q_{passive} around 1M [96]. This value of Q_{passive} has been assumed in calculations throughout this thesis. More information on modegap resonator design can be found in Christos Santis's thesis [71].

A.1   Modegap grating resonators

A periodic perturbation to a waveguide, known as a grating, will couple a forward-propagating wave to a backward-propagating wave. Let the field in such a waveguide be given as the sum of the forward- ($+\hat{z}$) and backward- ($-\hat{z}$) propagating waves,

$$E(z) = A(z)E_0(x,y)\exp[\mathrm{i}(\omega t - \beta z)] + B(z)E_0(x,y)\exp[\mathrm{i}(\omega t + \beta z)], \qquad \text{(A.1)}$$

where $A(z)$ and $B(z)$ are the slowly-varying mode amplitudes, $E_0(x, y)$ is the transverse mode profile, and β is the propagation constant of the mode. Let the slowly-varying mode amplitudes be given by

$$A(z) = a(z) \exp(i\Delta\beta z) \tag{A.2}$$
$$B(z) = b(z) \exp(i\Delta\beta z),$$

where $\Delta\beta$ is the phase mismatch between the mode and the grating, given by

$$\Delta\beta = \frac{2\pi n_{\text{eff}}}{c}(f - f_{\text{B}}), \tag{A.3}$$

where n_{eff} is the effective index of the mode and f_{B} is the Bragg frequency of the grating. Then, the coupled-mode equations relating a and b for a weak grating are given by [2, p.727]

$$\frac{\mathrm{d}}{\mathrm{d}z}a(z) = (\gamma - i\Delta\beta)a(z) - i\kappa b(z) \tag{A.4}$$
$$\frac{\mathrm{d}}{\mathrm{d}z}b(z) = i\kappa^* a(z) + (-\gamma + i\Delta\beta)b(z),$$

where γ is the net gain coefficient ($\gamma = \Gamma_{\text{act}}g - \alpha$), and κ is the coupling strength of the grating. A waveguide grating like this will reflect incident light over a certain frequency range, known as its "photonic bandgap" in reference to electronic bandgaps in crystals. Continuing the analogy, the high-frequency edge of the photonic bandgap is called the "conduction bandedge" (f_{c}) and the low-frequency edge the "valence bandedge" (f_{v}). The coupling constant κ is related to the bandgap width by [2, p.577]

$$|\kappa| = \frac{n_{\text{eff}}\pi}{c}(f_{\text{c}} - f_{\text{v}}). \tag{A.5}$$

These coupled mode equations can be diagonalized to find second-order differential equations for $a(z)$ and $b(z)$. In the case that $\Delta\beta$ and κ are nearly constant in z and
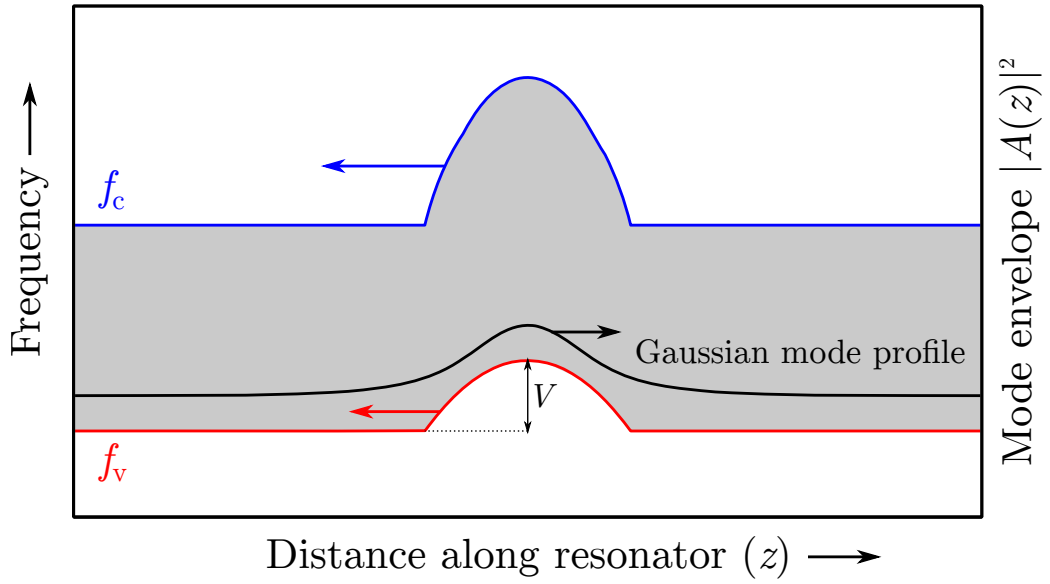
Figure A.1: A quadratically-modulated photonic well. The shaded area represents the bandgap, in which optical waves are forbidden to propagate except at the resonance frequency. The Gaussian-like envelope for the resonant mode is plotted also.

$\gamma = 0$, the equation for the forward-propagating wave is

$$\frac{\mathrm{d}^2}{\mathrm{d}z^2}a(z) = -(\Delta\beta^2 - \kappa^2)a(z). \tag{A.6}$$

This equation is analogous to the 1D, time-independent Schrödinger equation in which the frequency valence band edge (f_v) is the analogue of the potential energy function from quantum mechanics. Therefore, the solutions known for particles trapped in energy wells in quantum mechanics are useful to understand how optical modes can be localized in photonic wells in these grating resonators.

In quantum mechanics, a particle in an infinite quadratic energy well (the quantum harmonic oscillator) is known to exist in quantized energy states. The ground state has a longitudinal Gaussian profile, which is "well-behaved" in both real space and k space. A shallow, quadratic photonic well which only hosts the single "ground state" is therefore a good design for a laser resonator. Figure A.1 shows an example of a photonic well like the ones used in this thesis. The valence bandedge of the well is modulated quadratically at the center of the resonator to create the photonic well
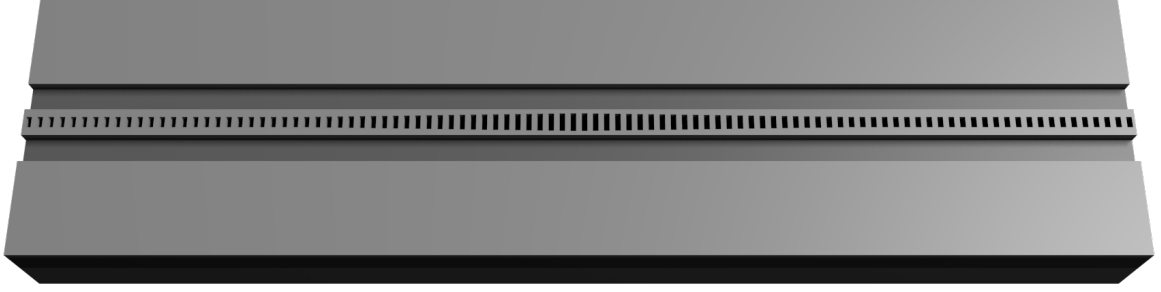
Figure A.2: Cartoon drawing of a 1D modegap resonator. The width of the holes in the waveguide are modulated to form a quadratic photonic well.
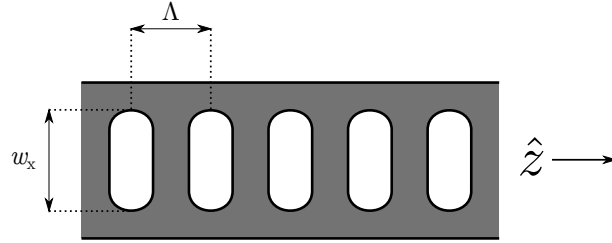

Figure A.3: Size and shape of the holes fabricated by electron beam lithography. The width of the holes (w_x) is varied along z to achieve the desired valence frequency bandedge (f_v). The period (Λ) is kept constant for a single device, but varied between devices to tune the operating wavelength of a high-Q hybrid laser. Here, the wave propagates in $\pm\hat{z}$.

with uniform mirror sections on each side of the well. The frequency depth of the well is V, as shown in the figure. The uniform mirrors are terminated after a certain length, allowing light to couple out of the resonator. A single mode is localized in this well, with the Gaussian-like mode envelope plotted near the well. Optical resonators made using this design methodology are known as "modegap" resonators, and they have very high quality factors [50; 58; 97].

The quadratic modulation can be applied in one-dimensional photonic crystal waveguide resonators by modulating the width of periodic holes in the waveguide [98–102], as seen in figure A.2. The grating in the lasers from this thesis is formed by etching holes in a silicon waveguide (which will then be bonded to III-V). Holes are rectangular with round caps as seen in figure A.3. They have constant period Λ, around 240 nm, and a duty cycle of 50%.

A.2 Transverse geometry

The transverse cross-section of the waveguide is designed using Comsol (a commercial finite element solver) to solve for the eigenmodes of the waveguide. The design constraints are:

1. Most of the mode should reside in the low-loss silicon, in order to make $\Gamma_{\text{III-V}}$ as small as possible.

2. The waveguide trench etch should be shallow and the waveguide rib wide in order to keep the mode weak at the rough etched sidewalls.

3. The waveguide should be single-mode or nearly single-mode, with any higher-order modes having odd symmetry so they are not reflected by an even grating.

The III-V structure is mostly determined by the need to have it perform well electrically, so there is little flexibility for changing its structure to get better optical performance. Actually, this constraint is an advantage of the hybrid Si/III-V platform: the silicon portion of the cavity can be designed for good optical performance, leaving the III-V design to concentrate on good electrical performance. More details on the III-V wafer structure used in high-Q hybrid lasers can be found in section C.2.2, and a cartoon cross section of the final design can be found in figure 4.1.

A.3 The resonator's quality factor

The total quality factor of a cavity can be broken down into its constituent parts according to equation 2.13. The notable sources of loss in these cavities are absorption, scattering, coupling to radiation modes, and external coupling as useful output. The total Q is then

$$Q_{\text{tot}}^{-1} = Q_{\text{abs}}^{-1} + Q_{\text{sc}}^{-1} + Q_{\text{rad}}^{-1} + Q_{\text{e}}^{-1}, \tag{A.7}$$

with their respective subscripts. The total Q is therefore limited by its lowest component, which in III-V lasers is usually either absorption or external coupling in III-V

lasers. The lasers presented in this thesis aim to minimize these components of loss. A side effect of increasing Q_{abs} and Q_{e} is that the other components of loss begin to limit the total Q. Thus, all of these components should be considered during the design of a high-Q hybrid laser. This section will show that the components other than absorption are independent of $\Gamma_{\text{III-V}}$, so the assumption that Q_{passive} is independent of $\Gamma_{\text{III-V}}$ in equation 3.4 is a good approximation.

A.3.1 Absorption

Optical absorption is weighted by the confinement factor of the mode in each material, as given by equation 2.6. III-V is much more absorbing than silicon; therefore, Q_{abs} is maximized by shifting as much modal energy away from lossy III-V into low-loss silicon as is possible, either through replacing the III-V with silicon or through modal engineering. The total absorption Q is

$$
\begin{aligned}
Q_{\text{abs}}^{-1} &= \frac{\Gamma_{\text{III-V}}}{Q_{\text{III-V}}} + \frac{1 - \Gamma_{\text{III-V}}}{Q_{\text{Si}}} \\
&\approx \frac{\Gamma_{\text{III-V}}}{Q_{\text{III-V}}}.
\end{aligned}
\tag{A.8}
$$

Here, $Q_{\text{III-V}}$ is the material absorption of III-V, approximately 10k for highly-doped active material [36–42].

A.3.2 Scattering

Scattering is most significant from the rough etched waveguide sidewalls. Scattering is reduced in the lasers presented in this thesis by guiding the mode with a very shallow etch in silicon, as seen in the cross-section of the waveguide (figures 4.1 and 5.1). The shallow etch results in very little sidewall and, therefore, little scattering [51; 52]. Similarly, the waveguide is designed to be $2\,\mu\text{m}$ wide to make the mode weak at the sidewall, also reducing scattering.

Silicon dioxide is easily grown from silicon, providing one further way to reduce scattering. Thin layers of thermal oxide ($\sim$25 nm) are grown on the etched silicon

chips used to make the lasers from this thesis. Scattering is reduced because the thermal oxide physically smooths rough surfaces and reduces the index contrast between the rough silicon waveguide and its cladding [55].

Scattering depends on the intensity of the mode at the sidewall, so it may depend on $\Gamma_{\text{III-V}}$. Under the replacement transformation, the shape of the mode doesn't change. Under the modal engineering transformation, the mode concentrates in the silicon waveguide, but the etched sidewalls are far from the most intense region of the mode. For this reason, Q_{sc} is assumed to be independent of $\Gamma_{\text{III-V}}$.

A.3.3 Radiation

The biggest potential problem with using a shallow-etch rib waveguide is that the guided mode may easily couple to radiation modes in the adjacent silicon slab, losing stored energy [103]. The strength of the coupling can be found by finding the longitudinal mode profile in the resonator and transforming it into k-space. Waves with small values of k along the propagation direction are not guided by the waveguide, so an integral of the k values which lie across the light line yields the coupling to leaky modes [98].

It is clear that coupling to radiation modes will be minimized by having a very narrow distribution of k values. This is the primary advantage of the 1D modegap-type resonator discussed at the beginning of the section: it is easy to tailor the envelope of the mode along the propagation direction by deterministically modulating the valence bandedge. By designing a quadratic photonic well, the field envelope is Gaussian in both real space and k space. A broad, shallow photonic well thus has a very tight distribution of k values, minimizing the potential coupling to leaky modes.

The quadratic well can be formed in either the valence band or the conduction band. Continuing the earlier analogy to quantum mechanics, an upward-opening well in the conduction band is a "donor"-type well and a downward-opening well in the valence band is a "acceptor"-type well. Acceptor-type wells are slightly farther from the light line, so they are chosen for these resonators.
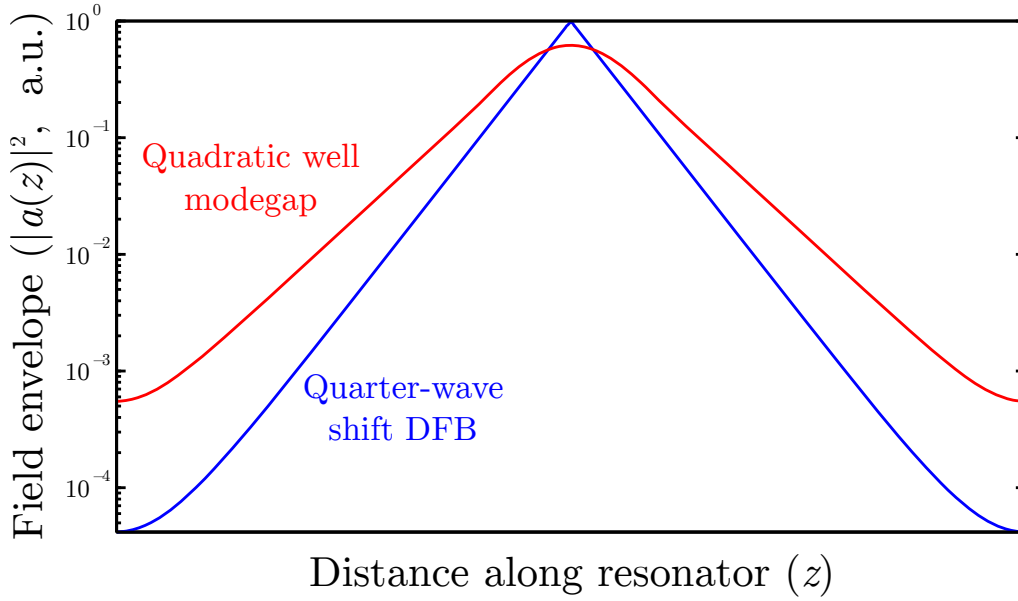
Figure A.4: Mode envelope profiles for a 1D modegap grating resonator and a standard QWS DFB. The QWS DFB has κ the same as in the uniform modegap mirrors. Envelopes have been normalized to have the same area.

Conveniently, the broad field envelope along the resonator also reduces spatial hole burning compared to the field profile of quarter-wave shift (QWS) DFB gratings, which are sharply-peaked at the center of the cavity, as seen in figure A.4. Modegap cavities therefore improve upon QWS DFBs in two ways: (1) the field envelope is smoother, causing a tighter distribution in k-space, reducing coupling to radiation modes, and (2) the field is broader in real space, reducing spatial hole burning.

Radiation loss depends on the longitudinal parameters of the grating, so it is also independent of $\Gamma_{\text{III-V}}$.

A.3.4 External coupling

External coupling is determined by the uniform mirror sections on each end of the quadratic well. The field envelope decays exponentially in the mirrors, such that the number of mirror holes determines the amount of stored energy that couples to the output. External coupling is often considered separately from the other sources of loss because it provides useful output; however, external coupling reduces the number

of photons stored in the cavity just the same as the other sources of loss, thereby increasing phase noise, and should be considered as just another source of loss.

For minimum phase noise, lasers should operate in a regime in which external coupling is minor compared to the dominant source of loss in order to store as many photons as possible. In such a cavity, more photons will leave the cavity and be lost than the number of photons leaving as useful output. The external efficiency describing the fraction of photons leaving the cavity which are useful output is given by [2, p.696]

$$\eta_{\mathrm{ex}} = \frac{Q_{\mathrm{e}}^{-1}}{Q_{\mathrm{e}}^{-1} + Q_{\mathrm{i}}^{-1}}, \tag{A.9}$$

where Q_{e} is the Q for external coupling and Q_{i} is the "intrinsic" Q, accounting for all other sources of loss. The optical output power in steady state can be found by multiplying the external efficiency by the stimulated transition rate into the mode and the energy of a single photon. Therefore, there is a tradeoff between large stored energies in the cavity and high external efficiency.

The field envelope is exponentially decaying in the mirror section, so external coupling decreases exponentially with an increasing number of mirror holes on both sides of the photonic well. External coupling is therefore highly sensitive to deviations in mirror coupling strength, so the devices made for this thesis are fabricated as several different designs, each with a different number of mirror holes.

External coupling can be controlled independently of the other cavity parameters by tuning the number of mirror holes, making Q_{e} a useful parameter to vary in an experiment. It can be made independent of $\Gamma_{\text{III-V}}$ by adjusting the mirror length for designs with different $\Gamma_{\text{III-V}}$.

A.4   Simulation

Numerical calculation is used to find the various properties of the modegap resonators, like the number of resonant modes in the well, their resonant frequencies, external coupling, coupling to radiation modes, and the threshold gain of all modes in the

laser. A specific transverse design is needed in order to calculate the strength of the grating (κ) which links the various parameters used in the design (f_c, f_v, etc.). This section will use the transverse profile from the high-Q hybrid lasers presented in chapter 4.

A.4.1 Frequency bandedges

A modegap grating is designed by choosing values for the photonic valence bandedge (f_v) along the length of the grating. The physical size of the holes (w_x) needed to make the designed values can be found by 3D simulation of a single grating unit cell containing one hole. The simulation will also give the photonic conduction bandedge value (f_c) and, therefore, the coupling strength of the grating unit cell (κ) through equation A.5.

Simulations are performed using Comsol (commercial 3d finite element solver) to find eigenfrequencies of a unit cell. The width of the holes (w_x) is varied to find f_v for each hole width. To save computation memory and time, even symmetry is used to simulate half of a unit cell with an even boundary condition applied to the plane dividing the cell in half. Periodic boundary conditions are applied in the propagation direction and scattering boundary conditions are applied to the boundaries far from the mode. The simulation finds the photonic bandedges (f_v and f_c) for each unit cell. Figure A.5 shows the electric field of the photonic bandedge modes as solved for by Comsol.

The mapping of $f_v \rightarrow w_x$ constitutes a "lookup table," used to translate the designed photonic frequency well into the hole widths needed to fabricate the resonator. Figure A.6 shows an example lookup table.

Figure A.7 shows an example of a photonic well designed using this process. The design starts with the valence bandedge shape ($f_v(z)$) with the parameters given in table A.1. The hole widths (w_x, figure A.8) necessary to make the valence bandedge shape are then found using the lookup table. With the hole sizes fixed, the conduction bandedge (f_c, figure A.7) and the coupling coefficients (κ, figure A.9)

Valence
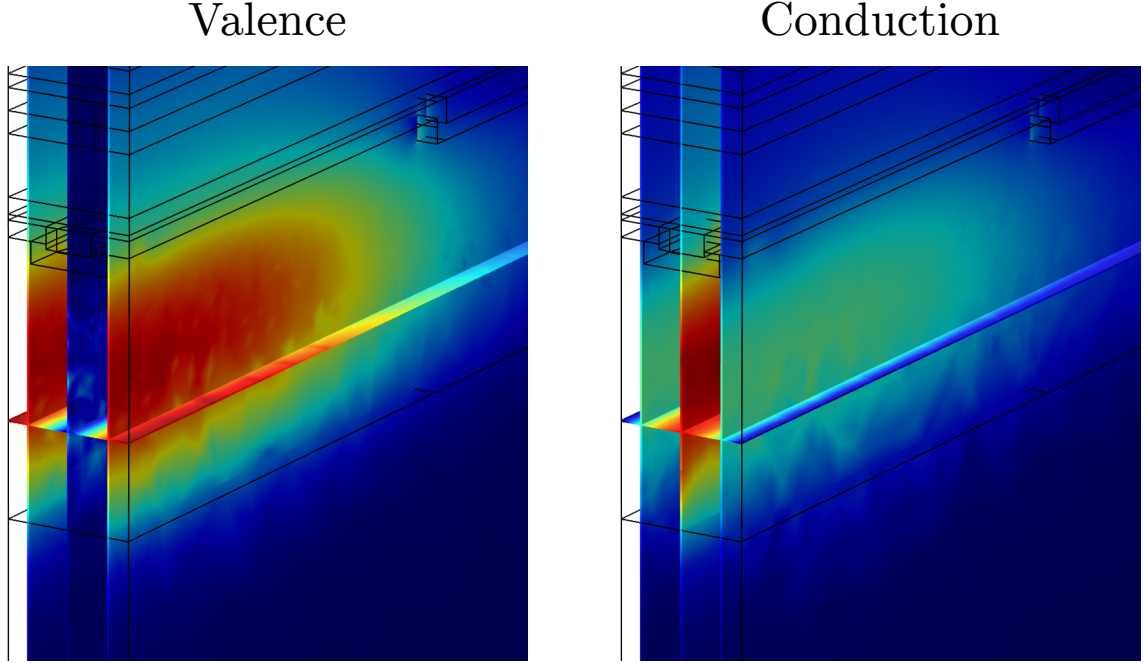
Conduction

Figure A.5: Electric field norm of the photonic bandedge modes as solved for by Comsol. The valence bandedge mode (f_v, with peaks in silicon) is shown on the left, while the conduction bandedge (f_c, with peaks in air) is shown on the right. This simulation was performed using the geometry of a high-Q hybrid laser (chapter 4).
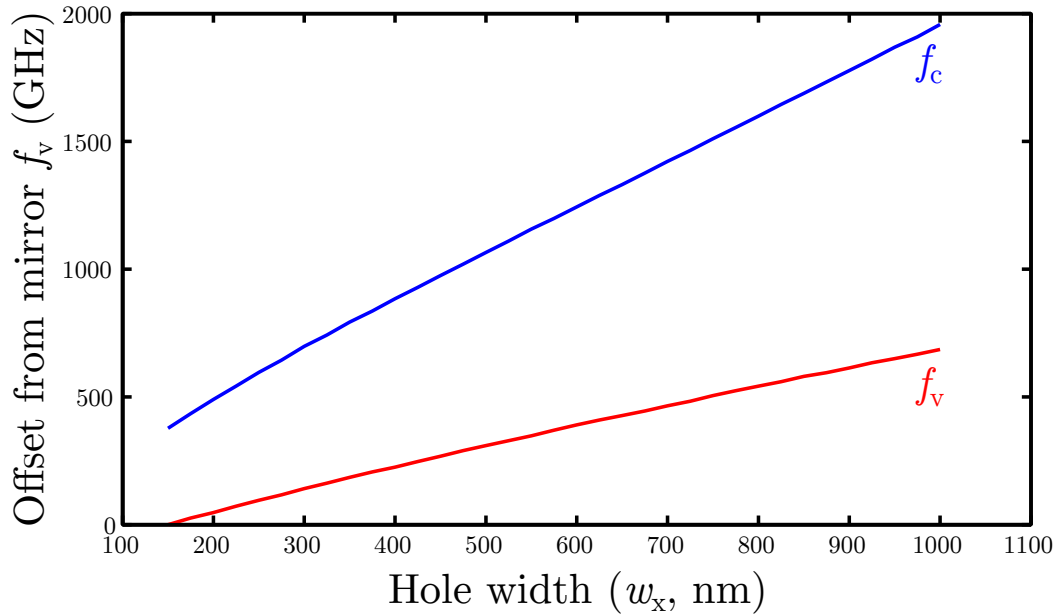
Figure A.6: This example lookup table is used to map the designed photonic well bandedges to the needed hole widths (w_x). This lookup table was made for the transverse geometry of a high-Q hybrid laser with no spacer (chapter 4).

Figure A.7: Example of a designed photonic well, with the valence bandedge (f_v) and conduction bandedge (f_c) labeled.

Parameter	Value
Well depth (V)	100 GHz
Number of well holes (N_w)	801
Number of mirror holes (N_m)	600 per side

Table A.1

Figure A.8: The hole widths needed to realize the photonic well design for the modegap resonator designed in this section.

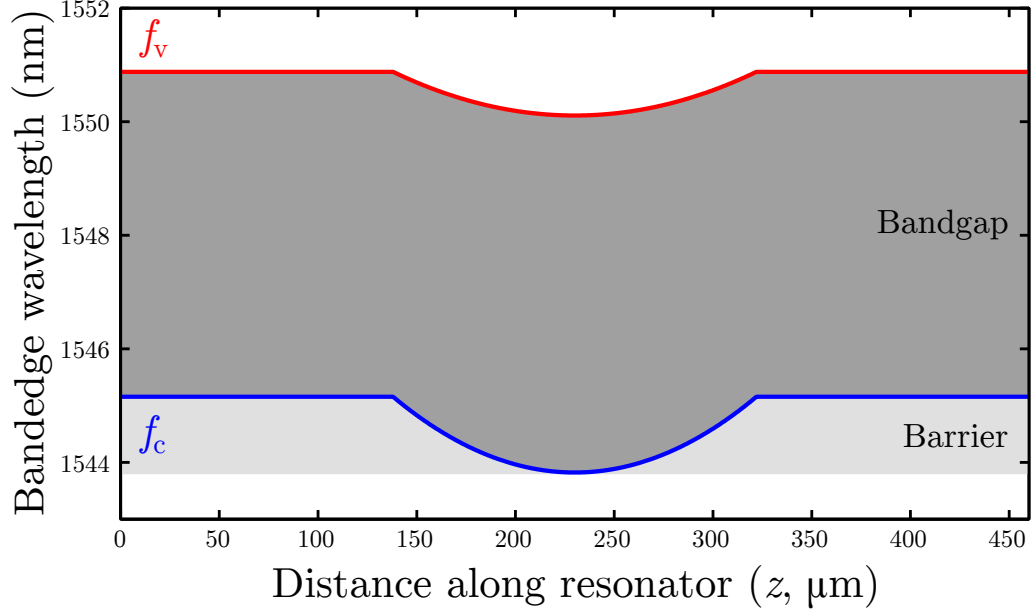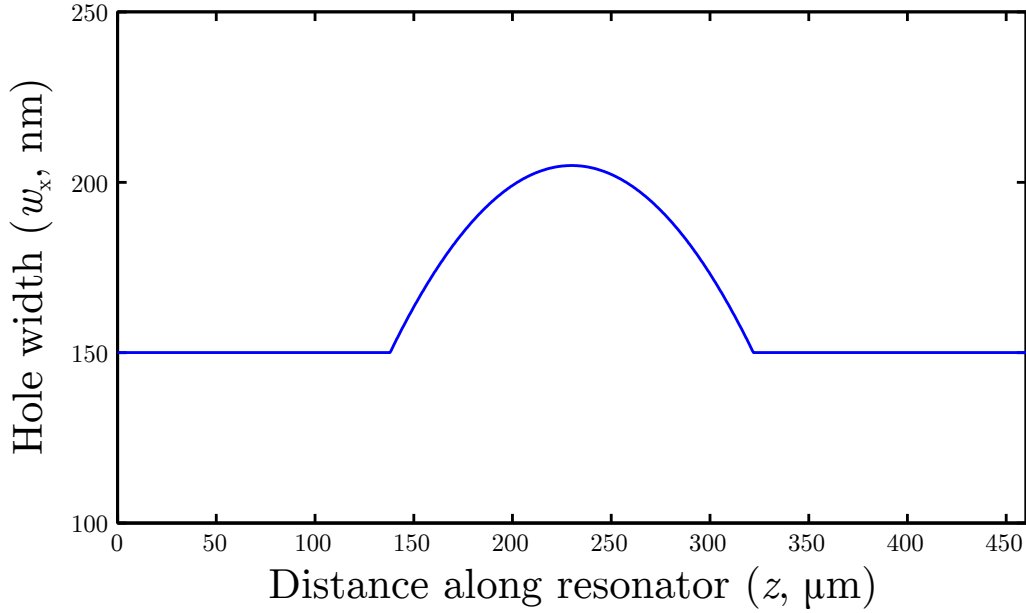can be calculated. It's important to note that the conduction bandedge also has a quadratic-like shape, forming a "barrier" that will partially reflect incident waves at these frequencies.

A.4.2 Passive transmission

The transmission of a passive modegap grating as a function of frequency can be found by evaluating the coupled mode equations (equation A.4) numerically with net gain (γ) set to zero. Figure A.10 shows the simulated transmission of the example modegap resonator. Several features are notable. The high-Q mode is found to be resonant at a wavelength inside the photonic well, near the valence bandedge as expected. Ripples in transmission occur on either side of the bandedge, but the ripples near the conduction bandedge show smaller maximum transmission because they are attenuated by the barrier.

Calculating the simulated transmission is necessary to ensure that only a single mode is hosted by the well.
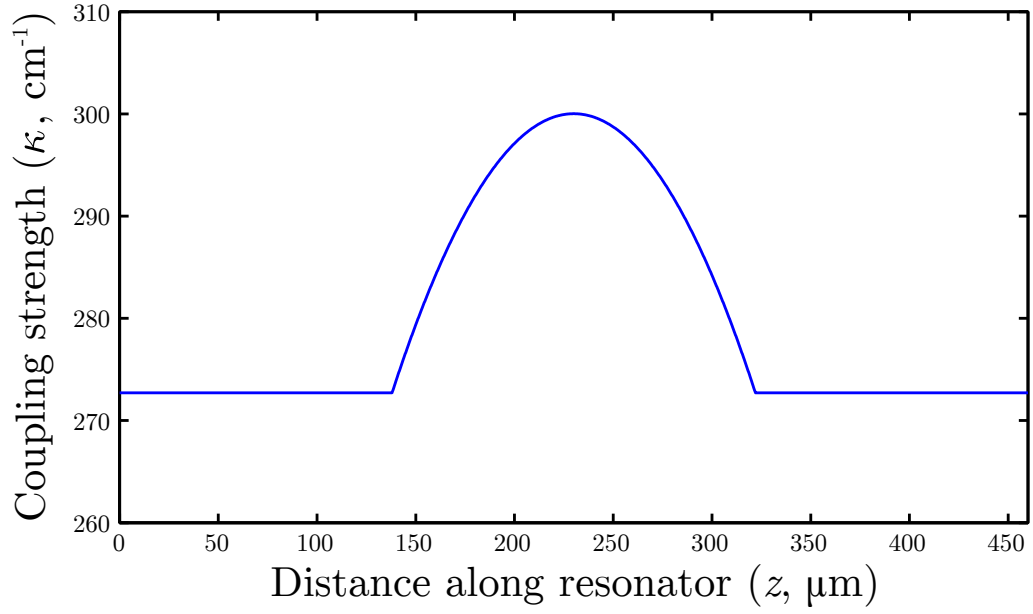
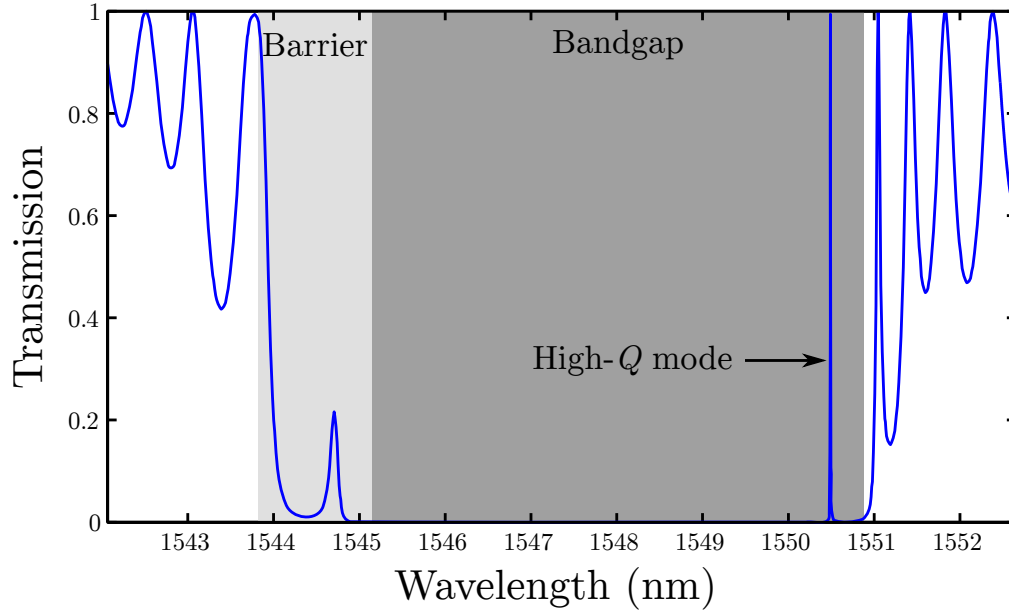Figure A.9: The calculated coupling strength of the example modegap grating designed in this section.

Figure A.10: Simulated transmission of the example modegap resonator designed in this section.

A.4.3   External coupling

The only source of loss in the transmission simulation is external coupling. Therefore, Q_e can be found by fitting the resonance transmission to a Lorentzian,

$$T(f) = \frac{(\Delta f/2)^2}{(f - f_0)^2 + (\Delta f/2)^2}, \tag{A.10}$$

where Δf is the full-width at half maximum, and f_0 is the center frequency of the resonance. The FWHM of the resonance is related to Q_e by

$$Q_e = \frac{f_0}{\Delta f}. \tag{A.11}$$

The example resonator designed in this section has Q_e of 400k.

Calculating the simulated transmission is therefore very useful to determine the number of mirror holes needed to achieve a given value of Q_e.

A.4.4   Longitudinal field envelope

The longitudinal field envelope $(a(z))$ is found by by evaluating the coupled-mode equations (equation A.4) at the resonance frequency.

Figure A.11 shows the longitudinal mode envelope for the high-Q mode designed in this section.

A.4.5   Coupling to radiation modes

Coupling to radiation modes can be estimated by taking the Fourier transform of the fast-oscillating longitudinal field that was found using the coupled mode equations (equations A.1, A.2, and A.4) into k-space. Mirror length is increased until the field near the facets no longer affects the spectrum. In k-space, the field is tightly centered around $\pm\beta$, as seen in figure A.12. The field may couple to radiation modes in the silicon slab if the k-values are equal. The maximum k for the silicon slab (k_{cutoff}) provides a cutoff value above which coupling will not occur. Therefore, integrating
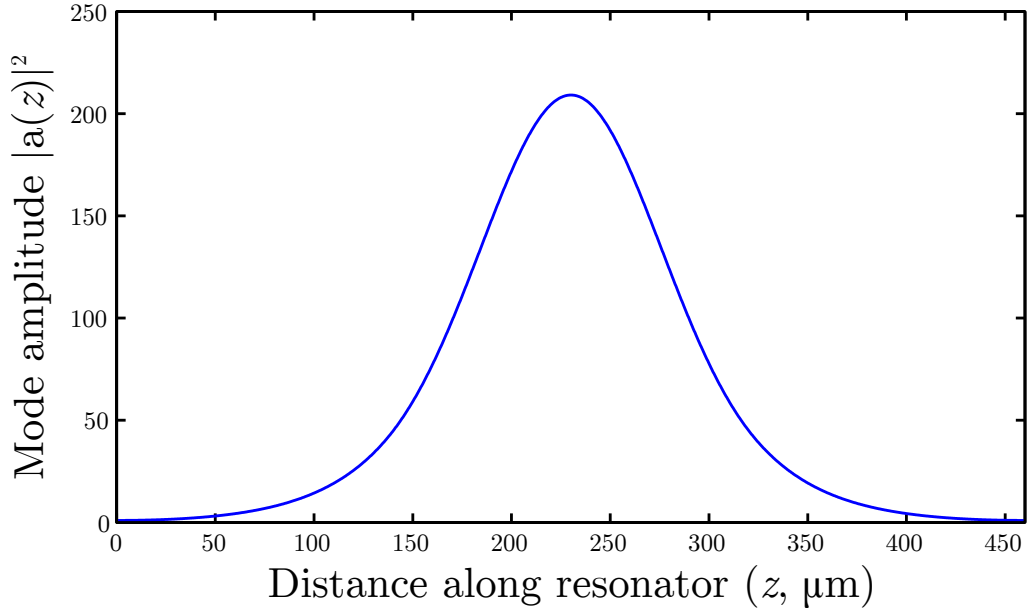
Figure A.11: Longitudinal mode profile for the high-Q mode in the example modegap resonator designed in this section. The mode is normalized to have 1 unit energy at the input and output.
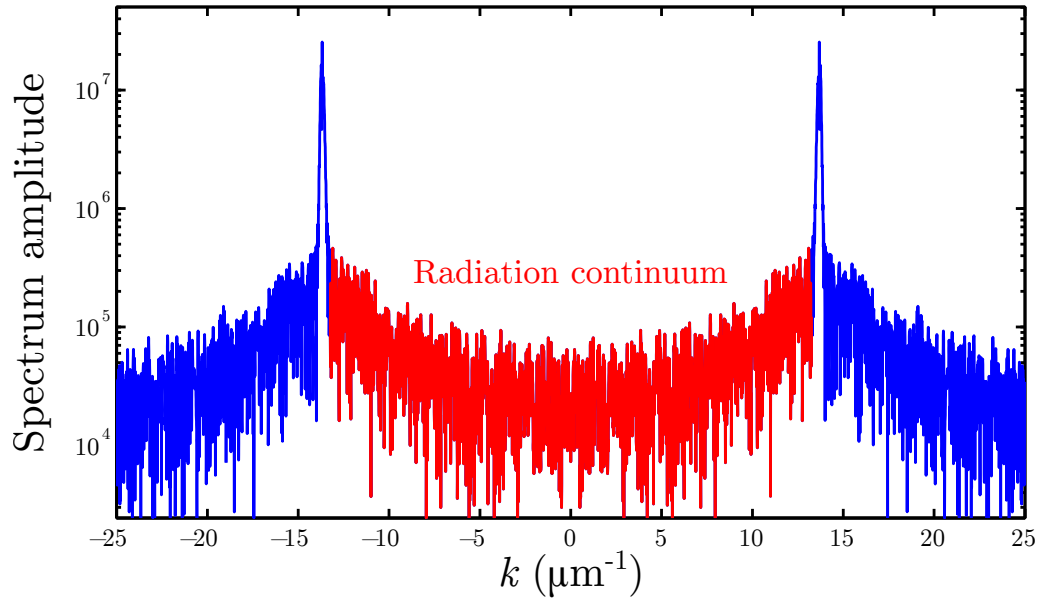

Figure A.12: Spectrum of the longitudinal field in k-space of the example modegap resonator designed in this section. An upper bound on the coupling to radiation modes is calculated by integrating the field with $|k| < k_{\text{cutoff}}$ (shown in red).

over the $k < k_{\text{cutoff}}$ puts an upper bound on the loss due to coupling to radiation modes.

This method of calculating radiation is highly sensitive to the value of k_{cutoff} and only gives a lower bound on Q_{rad}, so it should be used to compare different designs instead of to calculate exact values of Q_{rad}. As expected, the best Q_{rad} values are for modegap resonators with broad Gaussian-like mode envelopes, found in wide, shallow quadratic wells.

A.4.6 Threshold of all modes

The net threshold gain ($\gamma_{\text{th}} = \Gamma_{\text{act}} g_{\text{th}} - \alpha$; modal gain net of distributed losses like absorption and scattering) for each mode can be found using the coupled mode equations. The only source of loss inherent to the coupled mode equations is external coupling, so the net threshold gain must be exactly enough to overcome this loss. From equation 2.14,

$$\gamma_{\text{th}} = \frac{\omega}{v_{\text{g}} Q_{\text{e}}}. \tag{A.12}$$

The net threshold gain for the high-Q mode is therefore easy to calculate. It's also helpful to calculate the net gain required for other modes to lase. The threshold gain for each mode in the design can be found by solving the coupled mode equations (equation A.4) with gain, finding the values of gain for which transmission at a certain frequency goes to infinity. Infinite transmission physically means finite output with no input, which is laser oscillation [2, p.728].

Figure A.13 shows the threshold gain for all modes. As expected, the high-Q mode in the photonic well has the lowest threshold. As an interesting side note, the single transmission peak in the "barrier" region, closest to the conduction bandedge, has split into two distinct lasing modes. This may be due to the photonic barrier causing two coupled modes, one on each side of the barrier, to interact and split into two slightly different resonant frequencies.

Gain should clamp at threshold, so the other sidemodes would never reach threshold in an ideal laser. However, carriers are injected uniformly along the length of the
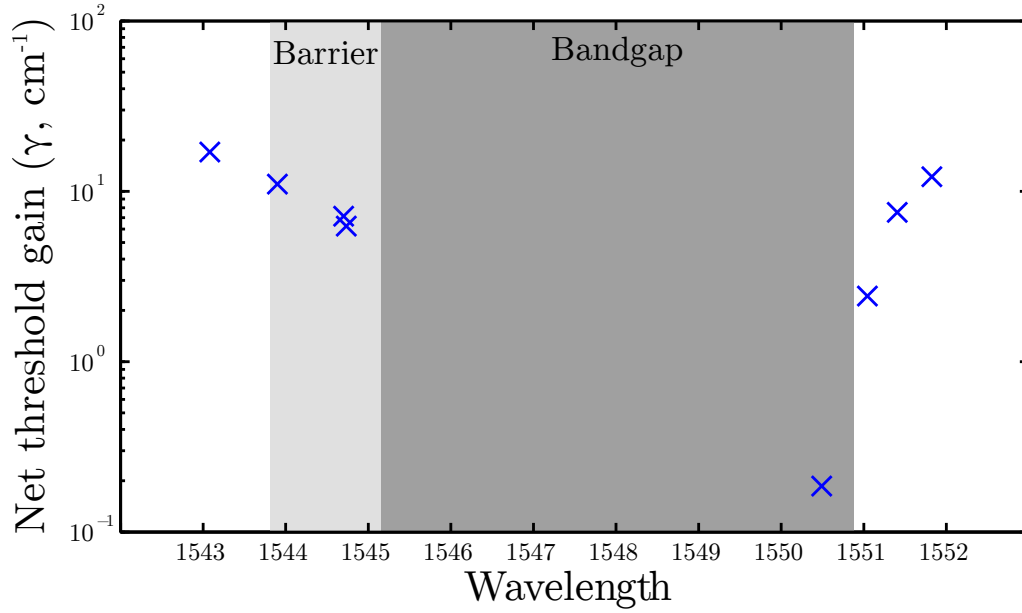
Figure A.13: Net threshold gain for each longitudinal mode in the high-Q hybrid laser. The high-Q mode is located in the bandgap and has the lowest threshold gain. The modes in the barrier region are the main competing sidemodes.

laser and are slow to travel along this dimension. The laser field is peaked near the center of the laser, so stimulated emission causes carriers to recombine fastest in the center of the laser and slower near the facets. This causes the carrier density to increase past the threshold density near the facets, in a phenomenon known as spatial hole burning. Modal gain, therefore, does not fully clamp at threshold everywhere in the laser.

Spatial hole burning causes the sidemodes to reach their threshold gains and lase when pumping far beyond the threshold of the fundamental mode. The photonic barrier encountered for frequencies outside the conduction bandedge (the short-wavelength side of the photonic bandgap) causes these modes to be weaker in the center than they are near the facets. Therefore, these modes are the ones likely to receive the most gain as a result of spatial hole burning and compete with the high-Q mode. In the hybrid Si/III-V lasers presented in this thesis, one blue sidemode will lase simultaneously with the high-Q mode at very high pump currents in some devices.

Spatial hole burning is reduced in lasers with a flat longitudinal field envelope because the stimulated emission rate is more constant along the length of the laser. Conveniently, the Gaussian shape of the longitudinal field envelope in modegap-type resonators is flatter than the decaying exponential of traditional quarter-wave shift DFB resonators. Therefore, spatial hole burning is expected to affect quadratic-well modegap resonators less than conventional quarter-wave shift DFBs.

This simulation of net gain for all modes is important to learn the gain margin for these sidemodes and to choose a design with relatively high gain needed for the sidemodes to lase.

Appendix B

Measurement techniques

This chapter will discuss the measurement techniques used in this thesis. The most important is the frequency noise power spectral density measurement. Some calibration measurements used to validate the frequency noise measurements of the low-noise hybrid Si/III-V lasers are provided.

B.1 Measuring frequency noise with a short-delay interferometer

An interferometer can be used to measure the frequency noise spectral density of the optical field. Consider an optical field with no intensity noise given by

$$E(t) = E_0 \exp[\mathrm{i}(\omega_0 t + \theta(t))].$$
(B.1)

The optical field is sent through a Mach-Zehnder interferometer (MZI) with equal power in each arm and a relative delay between the two arms of T. The output of the MZI is measured with a photodetector, which has a photocurrent proportional to the intensity of the electric field,

$$I_{\mathrm{pd}} \propto E_0^2 \left[\cos(\omega_0 T + \Delta\theta(T)) + 1 \right],$$
(B.2)
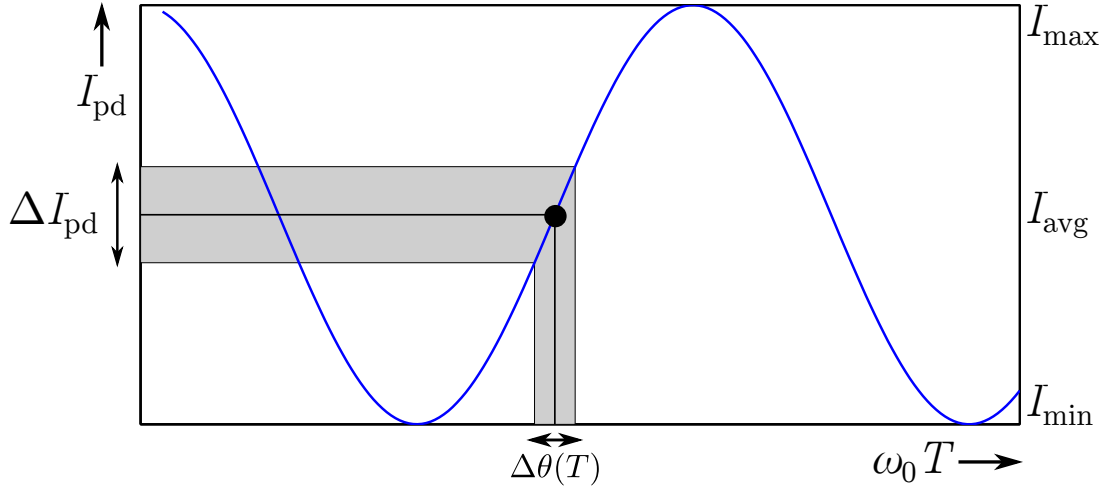
Figure B.1: Response of the MZI in $\omega_0 T$. When the center frequency is set to the quadrature point, phase fluctuations are converted to photocurrent fluctuations linearly, and can be measured by an RF spectrum analyzer.

where I_{pd} is the photocurrent and $\Delta\theta(T) \equiv \theta(t) - \theta(t - T)$ is the phase difference between the two arms. In the case of a very short delay, there is not enough time for a large phase difference to accumulate and $\Delta\theta \ll 1$. The photocurrent is

$$I_{\text{pd}} \propto E_0^2 \left[\cos(\omega_0 T) - \Delta\theta(T)\sin(\omega_0 T) + 1\right]. \tag{B.3}$$

The center frequency of the laser can be tuned to bias the interferometer in quadrature $(\omega_0 T = n\pi + \pi/2$, with n any integer). Then,

$$I_{\text{pd}} \propto E_0^2 \left(\Delta\theta(T) + 1\right). \tag{B.4}$$

The photocurrent contains a DC term plus a fluctuating term containing the statistics of $\Delta\theta$. An intuitive depiction of how an MZI biased to quadrature converts phase fluctuations to photocurrent fluctuations can be found in figure B.1.

The constant of proportionality in equation B.4 can be found experimentally by varying $\omega_0 T$ from its quadrature point to measure the maximum excursion of the photocurrent. Finding the constant this way is convenient because it automatically includes all the different sources of loss in the measurement. The minimum excursion

should be measured too. In practice, it is not zero because the optical splitters are not exactly 50/50, the polarization of the field is not perfectly maintained, etc. Then, the photocurrent is given by

$$I_{\mathrm{pd}} = I_{\mathrm{avg}} + \Delta\theta(T)I_{\mathrm{g}}, \tag{B.5}$$

where I_{avg} is the average current at quadrature and I_{g} is a phase-to-current gain coefficient, both of which can be measured on an oscilloscope. They are

$$I_{\mathrm{avg}} = \frac{I_{\mathrm{max}} + I_{\mathrm{min}}}{2}, \tag{B.6}$$

$$I_{\mathrm{g}} = \frac{I_{\mathrm{max}} - I_{\mathrm{min}}}{2}.$$

Measuring the photocurrent on an RF spectrum analyzer will yield the power spectral density of the photocurrent ($S_{I_{\mathrm{pd}}}$, units W/Hz), which can be converted to the spectral density of the phase variation ($S_{\Delta\theta(T)}$) by

$$S_{I_{\mathrm{pd}}}(f) = I_{\mathrm{g}}^2 R_{\mathrm{L}} S_{\Delta\theta(T)}(f), \tag{B.7}$$

where R_{L} is the load resistance of the spectrum analyzer. The spectral density of the phase variation is in turn related to the frequency noise spectral density by [8, p.217]

$$S_{\Delta\theta(T)}(f) = (2\pi)^2 T^2 S_f(f)\frac{\sin^2(\omega_0 T/2)}{(\omega_0 T/2)^2}. \tag{B.8}$$

The sinc^2 term in this equation causes the rolloff of the MZI, limiting its frequency response to its free spectral range (FSR $\equiv 1/T$). A measurement of the laser's phase noise should be restricted to frequency ranges in which the sinc^2 term is approximately unity. In this regime, the power spectral density of the photocurrent measured on the spectrum analyzer can be converted to the frequency noise spectral density by

$$S_f(f) = \frac{S_{I_{\mathrm{pd}}}(f)}{(2\pi)^2 I_{\mathrm{g}} R_{\mathrm{L}} T^2}. \tag{B.9}$$
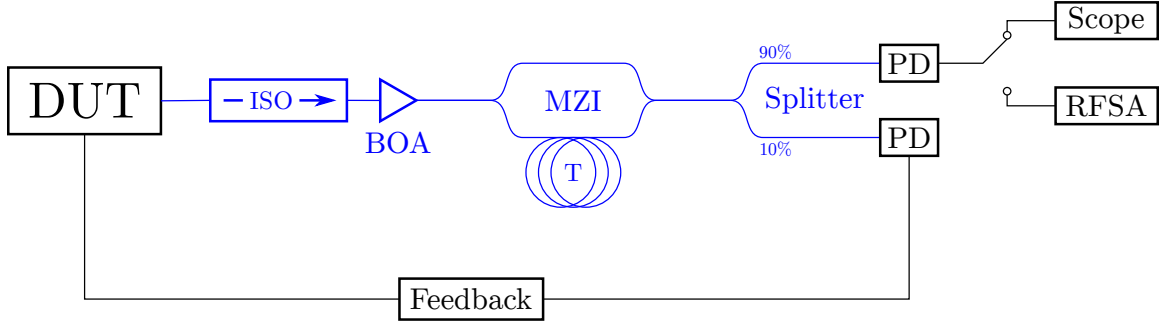
Figure B.2: Setup for measuring frequency noise power spectral density. The device under test (DUT) is shown in the upper-right corner. Black denotes electrical components, while blue denotes the optical path.

The linewidth can then be calculated using equation 2.75. It is important to choose the delay (T) carefully. A shorter delay (larger FSR) increases the useful bandwidth of the measurement, which was restricted by the sinc^2 term, but it also reduces I_g by making the slope in figure B.1 shallower, reducing the signal-to-noise ratio when measuring S_{I_pd}.

The configuration used to measure frequency noise spectral density in this thesis is shown in figure B.2. The output of the MZI is split between two photodetectors (PDs): one to measure the frequency noise spectral density of the photocurrent and one to provide electronic feedback to the laser, locking its frequency to the quadrature point of the MZI through (slow) thermal tuning. The output of the first photodetector is switched between an oscilloscope (scope), which is used to measure I_g, and an RF spectrum analyzer (RFSA), which is used to measure S_{I_pd}. Both instruments have the same input resistance.

Intensity noise was neglected in deriving equation B.4, though the coefficient E_0 multiplied by the DC term hints that strong intensity noise would dwarf the (assumed small) phase noise and should be remembered in this measurement. The intensity noise of the laser can be measured by connecting the laser output directly to the photodetector (without using an MZI) and using a variable optical attenuator to make I_avg the same as for the phase noise case. Then, S_{I_pd} of both cases can be compared to verify that the phase noise measurement is stronger than the intensity noise measurement.

B.2 Measurement calibration and validation

Measuring the frequency noise power spectral density is an absolute measurement and needs to be carefully calibrated in order to trust the results. Measurements are validated using control lasers with known frequency noise PSD, and suspect components (optical amplifier, photodetector, etc.) are investigated.

B.2.1 Control lasers

Two commercially-available lasers are measured as controls: a semiconductor DFB laser (JDS Uniphase, CQF-935/908) and an ultra-low noise fiber laser (NP Photonics, The Rock Module). The frequency noise spectrum of the JDSU laser was also measured at Orbits Lightwave (Pasadena, CA) several years ago using equipment traceable to NIST standards. The measurements of this control laser on the experimental setup used to characterize hybrid Si/III-V lasers are found to be essentially the same as the measurements on the traceable setup, thereby validating the experimental setup.

Figure B.3 shows the measured frequency noise PSD of these control lasers compared to the showcase $150\,\text{nm}$ spacer laser, all with the same I_{avg}. The upper bound on the "spontaneous emission linewidth" of the spacer laser is taken at about $100\,\text{MHz}$ carrier offset. At this offset, the fiber laser is two orders of magnitude less noisy than the spacer laser, so the detection electronics are capable of measuring less noise. Therefore, the measurement of the spacer laser frequency noise PSD is not limited by the detection electronics.

The sharp peak seen in the fiber laser frequency noise spectrum is the relaxation resonance. Incidentally, the fiber laser measurement happens to be mostly intensity noise because phase noise is so small in this laser.
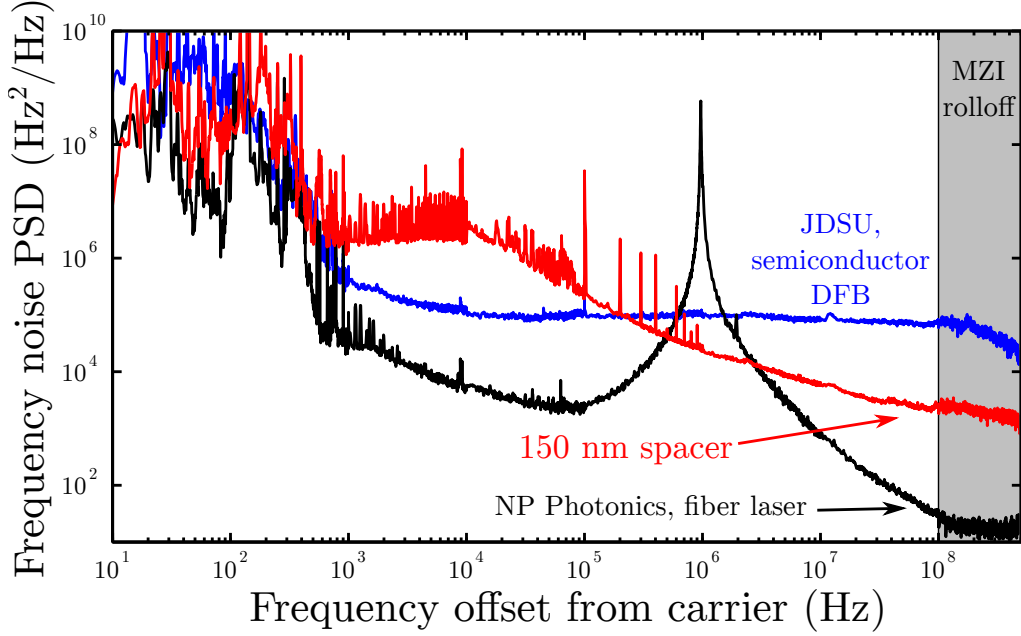
Figure B.3: Frequency noise PSD of the control lasers compared to the showcase 150 nm spacer laser. (JDSU $I = 100\,\mathrm{mA}$, $I - I_{\mathrm{th}} = 77\,\mathrm{mA}$. Spacer device ID Spacer150 B1 S2 D19, $\lambda \approx 1562\,\mathrm{nm}$, $I = 95\,\mathrm{mA}$, $I - I_{\mathrm{th}} = 30\,\mathrm{mA}$.)

B.2.2 Optical amplifier noise

Hybrid Si/III-V lasers are designed to have low external efficiency, so an optical amplifier is used to increase the signal (ThorLabs BOA 1004). The effect of the amplifier on phase noise must be considered as spontaneous emission noise from the amplifier may be stronger than the signal noise. Early experiments investigating optical amplifier noise suggested that the additional noise was significant [104], but more recent experiments suggest much smaller effects [105; 106].

Figure B.4 demonstrates that the frequency noise spectrum of the JDSU laser is not affected by the presence of the optical amplifier. For this measurement, the CW optical power of the JDSU laser at the input to the amplifier was attenuated to the value attained by the hybrid Si/III-V lasers using a static attenuator. Hybrid Si/III-V lasers are about an order of magnitude less noisy than the JDSU control, so the optical amplifier may affect their noise measurements even when the effect is not seen in the JDSU control. In any case, the amplifier will only add noise and the real frequency noise PSD could only be lower than the measured value.
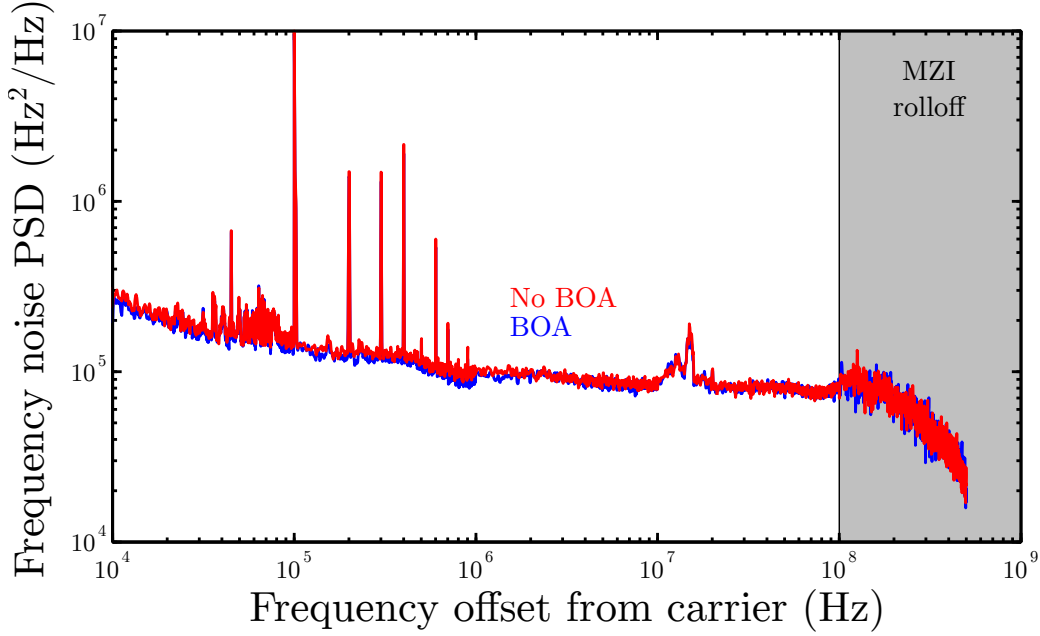
Figure B.4: Frequency noise spectrum of the JDSU control laser with and without the optical amplifier. ($I = 100\,\mathrm{mA}$, $I - I_{\mathrm{th}} = 77\,\mathrm{mA}$)

B.2.3   Photodetector response

Frequency noise measurements are taken with two different photodetectors (HP Lightwave 11982A, New Focus 1544B). Figure B.5 shows that the measurement is substantially the same with the two photodetectors.

B.2.4   RF spectrum analyzer

Frequency noise measurements are taken with two different RF spectrum analyzers (Agilent 4395A, HP 8565E). Figure B.6 compares the two instruments. The HP 8565E consistently measures values about $1\,\mathrm{dB}$ lower than the Agilent 4395A. Also, the HP 8565E shows some discontinuities in measurements that cross significant frequency values (e.g., $3\,\mathrm{GHz}$). Internal electronics, like a mixing oscillator or a filter, are reconfigured at these frequency values. The Agilent RFSA has been more recently calibrated, so it should be trusted.

Figure B.5: Frequency noise PSD measurement taken with two different photodetectors. (Device ID: Spacer150 B1 S2 D19, $\lambda \approx 1562\,\mathrm{nm}$, $I = 95\,\mathrm{mA}$, $I - I_{\mathrm{th}} = 30\,\mathrm{mA}$)
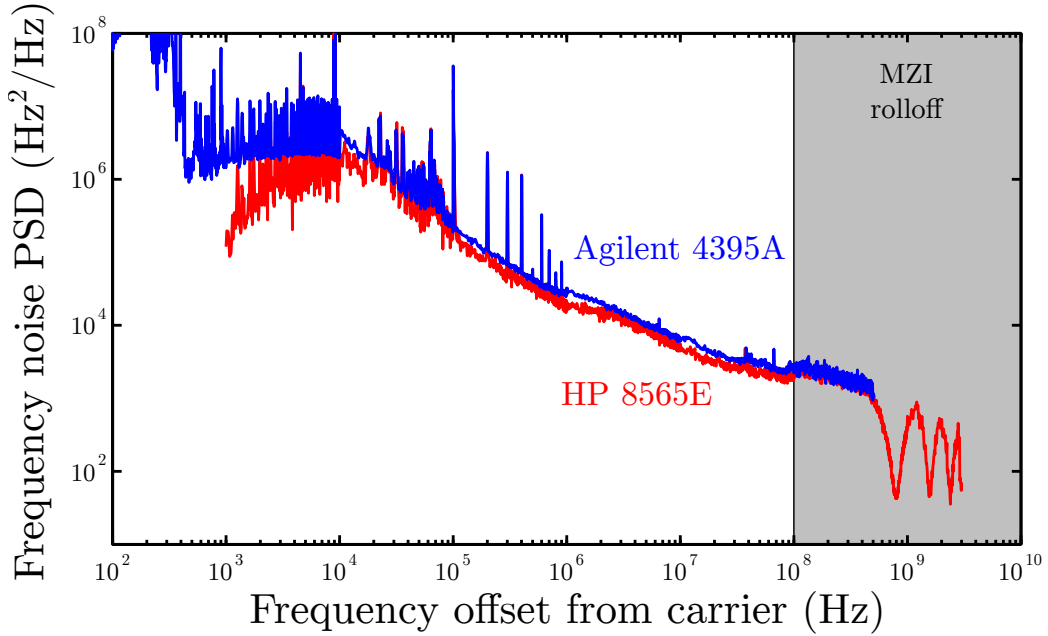
Figure B.6: Frequency noise PSD measurement taken with two different RF spectrum analyzers. (Device ID: Spacer150 B1 S2 D19, $\lambda \approx 1562\,\mathrm{nm}$, $I = 95\,\mathrm{mA}$, $I - I_{\mathrm{th}} = 30\,\mathrm{mA}$)
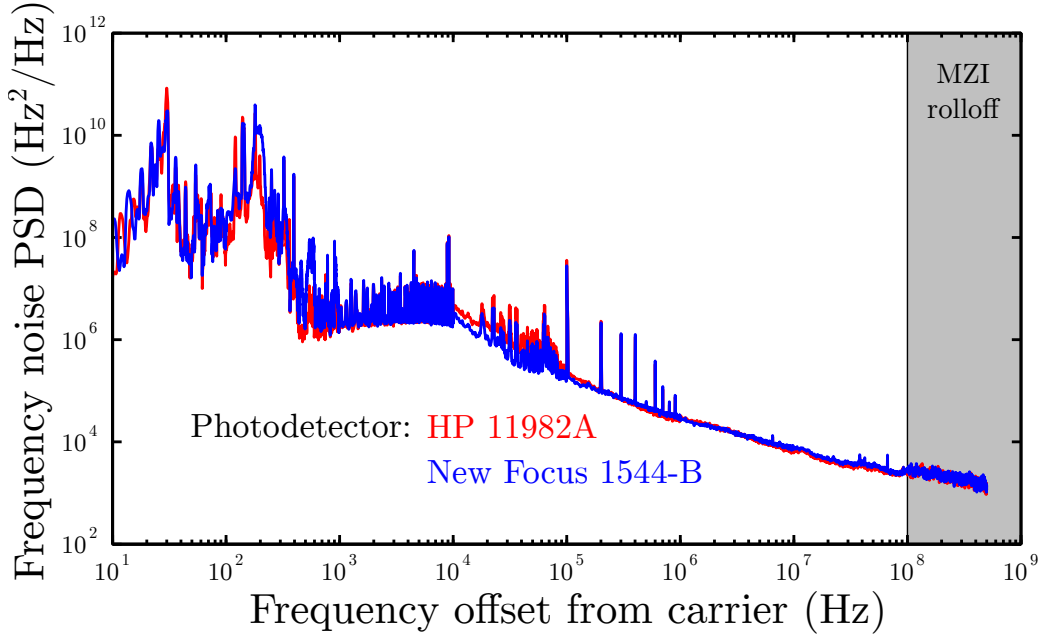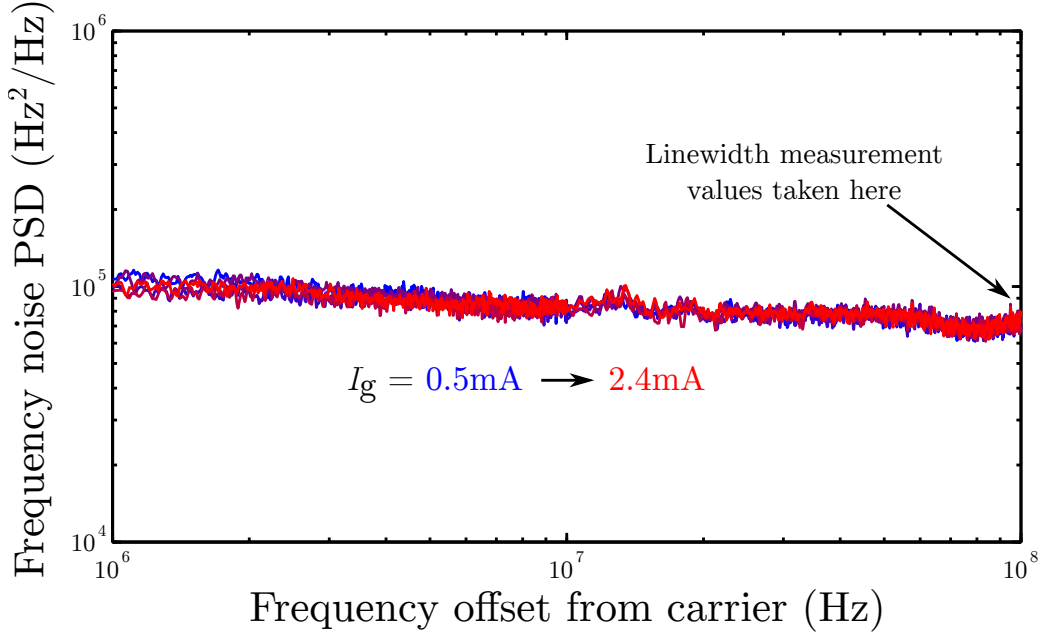
Figure B.7: Frequency noise PSD with variable optical attenuation reducing the optical power incident on the photodetector. Current gain parameters for this measurement are $I_\mathrm{g} = \{0.51\,\mathrm{mA},\ 0.97\,\mathrm{mA},\ 1.5\,\mathrm{mA},\ 1.9\,\mathrm{mA},\ 2.4\,\mathrm{mA}\}$. (JDSU control $I = 100\,\mathrm{mA}$, $I - I_\mathrm{th} = 77\,\mathrm{mA}$)

B.2.5 Optical power

Optical power incident on the photodetector may vary with many different experimental conditions. Coupling from the laser into the lensed fiber is different for each device. Optical fibers are connected and disconnected regularly, allowing for coupling between fibers to change. The frequency noise PSD measurement should be independent of the optical power falling on the photodetector as the current gain parameter (I_g, equation B.9) should account for this.

A variable optical attenuator was used to reduce the optical power incident on the photodetector. Figure B.7 shows the result of this experiment, demonstrating that the current gain parameter behaves as expected and the frequency noise PSD measurement is indeed independent of variable losses in the system.
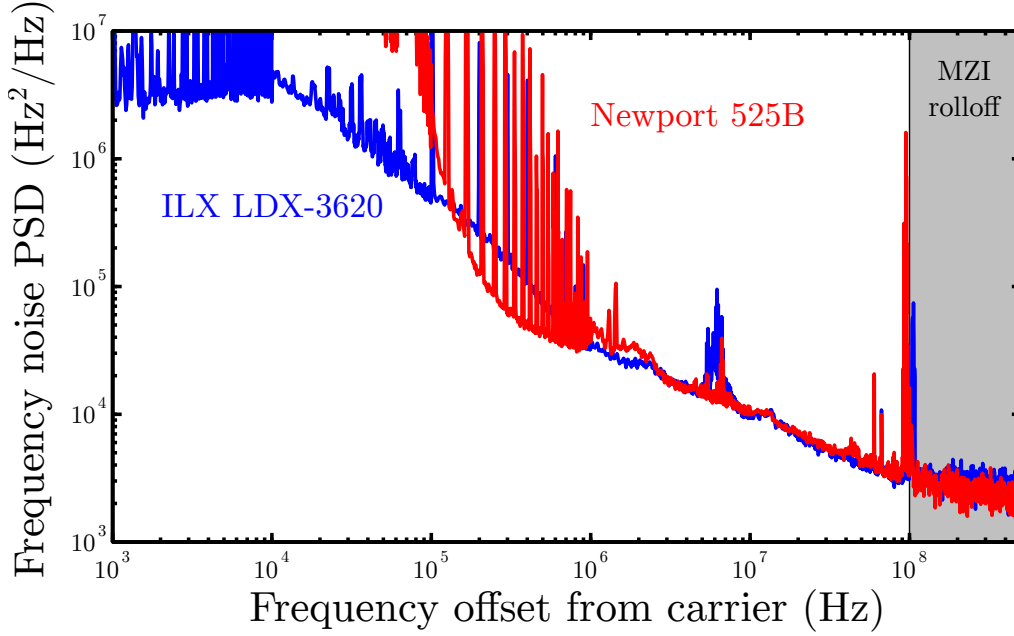
Figure B.8: Frequency noise PSD with two different current sources. The ILX LDX-3620 is a battery-powered ultra-low-noise current source, while the Newport 525B is not specifically designed to be low-noise. (Device ID: Spacer100 B1 S2 D13, $\lambda \approx$ 1563 nm, $I = 80\,\text{mA}$, $I - I_{\text{th}} = 45\,\text{mA}$)

B.2.6 Current source

Noise in the pump current source is expected to transfer to the frequency noise spectrum of the laser [107; 108]. The frequency noise PSD of a spacer laser was tested with a second current source (Newport 525B; Irvine, CA) which was not specifically designed to be low-noise. It runs off of AC power, unlike the battery-powered ILX LDX-3620 used for other measurements.

Figure B.8 shows a comparison of the same laser pumped by the two different current sources. At low offset frequencies, using the low-noise current source results in much lower frequency noise. However, at the high offset frequencies where the upper bound on the "spontaneous emission linewidth" is taken, there is no difference between the two current sources, indicating that the measured spectrum is not noise injected by the current source.
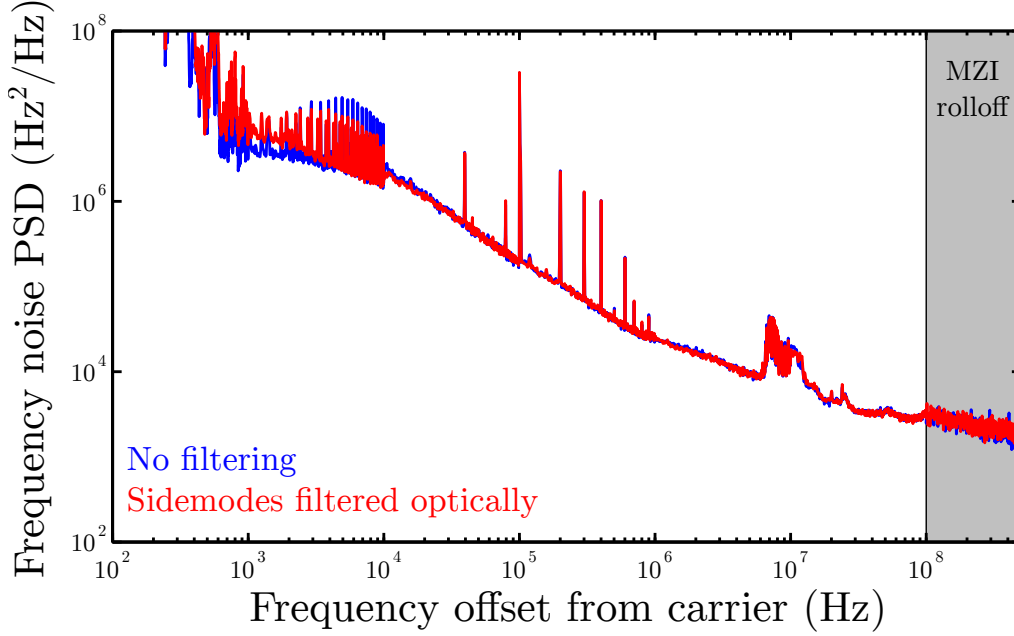
Figure B.9: Frequency noise PSD of a spacer laser both with and without sidemodes optically attenuated. (Device ID: Spacer150 B1 S2 D19, $\lambda \approx 1562\,\text{nm}$, $I = 100\,\text{mA}$, $I - I_{\text{th}} = 35\,\text{mA}$)

B.2.7 Filtering sidemodes

An optical filter was used to attenuate sidemodes and reduce any potential beating between sidemodes and the lasing mode. The optical filter has a $3\,\text{dB}$ bandwidth of $125\,\text{GHz}$ (for comparison, the photonic well in this laser is $120\,\text{GHz}$ deep and the photonic bandgap is $400\,\text{GHz}$). The filter was centered on the lasing mode by using the optical spectrum analyzer for rough alignment followed by maximizing output power. Filtering sidemodes runs the risk of increasing intensity noise (mode partition noise [8, p.163]), though any increase should be minimal in this nearly-single-mode laser.

Figure B.9 shows the frequency noise PSD for a spacer laser both with and without the optical filter. The measurement is identical in both cases.

Figure B.10: Frequency and intensity noise of a $100\,\mathrm{nm}$ spacer laser as measured by the RFSA. (Device ID: Spacer100 B1 S2 D13, $\lambda \approx 1563\,\mathrm{nm}$, $I = 80\,\mathrm{mA}$, $I - I_{\mathrm{th}} = 45\,\mathrm{mA}$)

B.3   Intensity noise

Intensity noise is added to phase noise in the photocurrent, so it must be measured to ensure that its power spectral density is lower than the frequency noise. Figures B.10 and B.11 show the frequency and intensity noise of spacer lasers as measured by the RFSA (i.e., $S_{I_{\mathrm{pd}}}$ for the measurement configurations with and without the MZI).

A variable optical attenuator was used to reduce the CW optical power incident on the photodetector to be the same value as during the corresponding frequency noise measurement.

The intensity noise is mostly well below the frequency noise for both lasers, verifying that the frequency noise measurement is not actually measuring intensity noise. From measurements taken with the HP 8565E RFSA, the relaxation resonance of spacer lasers appears to be higher than $1\,\mathrm{GHz}$, perhaps around $10\,\mathrm{GHz}$ as is common in semiconductor lasers. The data are not presented here as the spectrum analyzer is not calibrated at high frequency offsets.

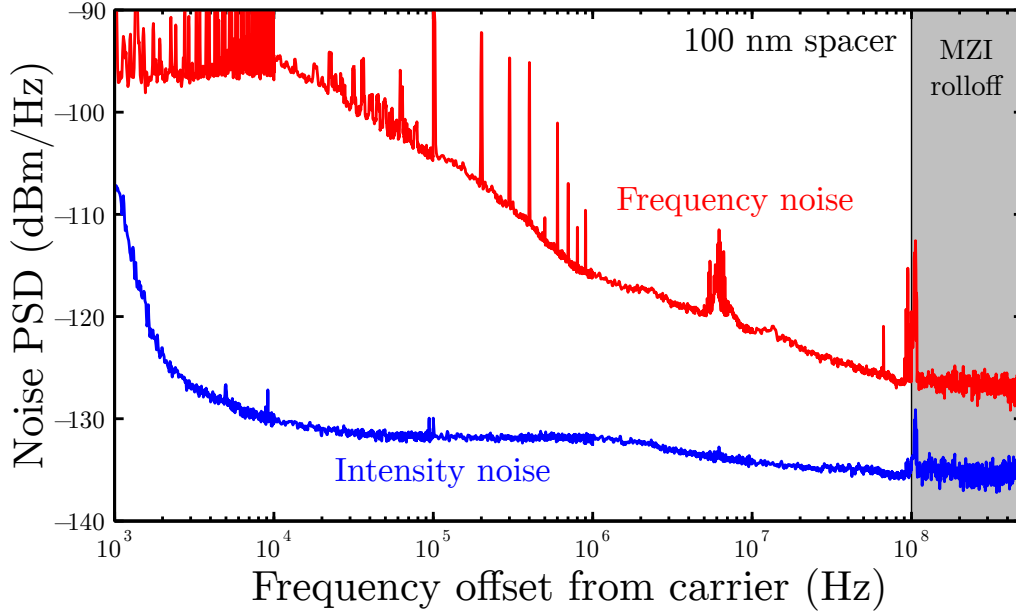The relative intensity noise (RIN) for each spacer laser is about $-135\,\mathrm{dB\,Hz^{-1}}$ at
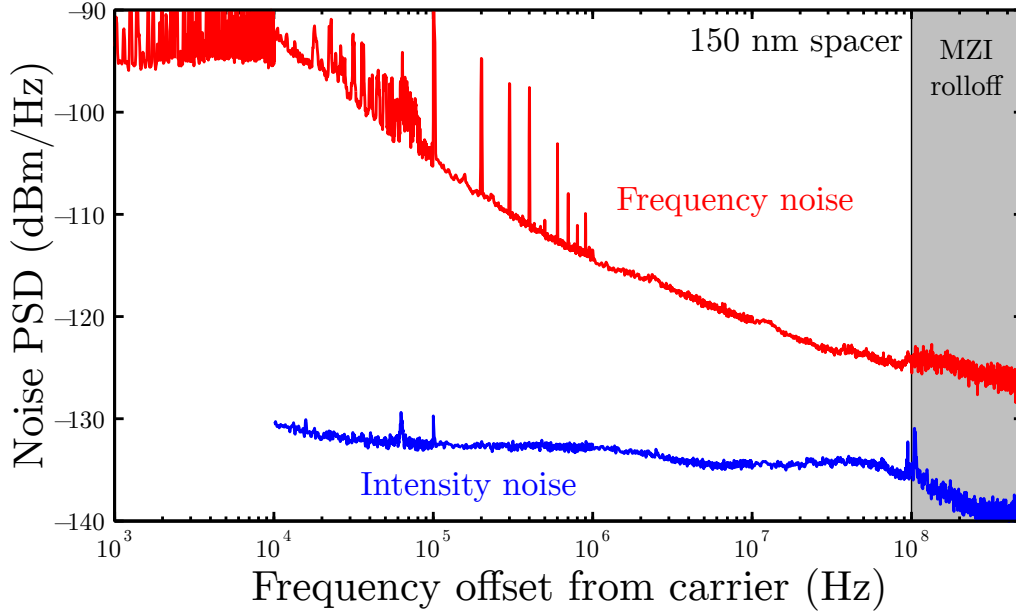
Figure B.11: Frequency and intensity noise of a 150 nm spacer laser as measured by the RFSA. (Device ID: Spacer150 B1 S2 D19, $\lambda \approx 1562\,\text{nm}$, $I = 95\,\text{mA}$, $I - I_{\text{th}} = 30\,\text{mA}$)

the pump currents shown. RIN was measured with the BOA as the signal was too weak to measure without amplification.

B.4   Other measurement tools

The other tools used to characterize the hybrid Si/III-V lasers are listed here by the measurement type.

IV curves: IV curves are characterized by two different instruments: an HP 4145B Semiconductor Parameter Analyzer for currents up to 5 mA and a Newport 525B CW Laser Diode Driver for all currents.

LI curves: Lasers are pumped CW by a Newport 525B CW Laser Diode Driver and output power is collected by an integrating sphere with an InGaAs sensor connected to an ILX 6810B Optical Multimeter.

Optical spectrum: Optical spectra are measured by an HP 70951B Optical Spec-

trum Analyzer. Lasers are pumped by a Newport 525B CW Laser Diode Driver and light is collected at the output facet of the laser by a lensed single-mode fiber.

Frequency noise PSD: Lasers are pumped CW by an ILX Lightwave LDX-3620 Ultra Low Noise Current Source (battery-powered). Light is collected at the output facet of the laser by a lensed single-mode fiber. There are two fiber isolators about 1 m from the laser facet. The signal is amplified by an optical amplifier (ThorLabs BOA 1004) pumped by a custom battery-powered current source made by Arseny Vasilyev (Chipset: Wavelength Electronics LDD400-1P), with a polarization controller before the amplifier tuned for maximum output. The light is passed through a custom fiber Mach-Zehnder interferometer (FSR 847 MHz). The MZI output is split between two photodetectors: an HP 11982A Lightwave Converter Photodetector for the signal and a ThorLabs PDA10CF for feedback. The optical power incident on the HP photodetector (the signal) is attenuated by a variable attenuator (JDS Fitel HA9) such that the maximum power out of the interferometer is just below photodetector saturation. The MZI fringes are measured on an oscilloscope (Tektronix TDS 3032B) to determine the frequency-to-amplitude gain of the interferometer and the quadrature point. The center frequency of the laser is locked in quadrature by locking the PDA10CF photocurrent to an adjustable reference using a custom battery-powered feedback circuit made by Arseny Vasilyev. RF spectra are measured on an Agilent 4395A RF Spectrum Analyzer set to "sample" detection.

Intensity noise PSD: This measurement is identical to the frequency noise PSD measurement, except with the MZI removed. The variable attenuator is used to match the power incident on the photodetector as in the corresponding frequency noise measurement.

Wavelength: Precise wavelength measurement is performed by a Burleigh WA-1100 wavemeter. Lasers are pumped CW with a Newport 525B CW Laser Diode Driver and light is collected at the output facet of the laser by a lensed single-

mode fiber. The temperature controller is allowed to settle before the measurement is taken.

The temperature of the laser is controlled in all measurements by a custom battery-powered temperature controller circuit made by Arseny Vasilyev (Chipset: Wavelength Electronics WTC3243). Hybrid Si/III-V lasers are mounted on a custom copper block with a TEC sinking heat to another copper block below. Lasers are enclosed by a large plastic box to prevent air currents from affecting measurements.

Appendix C

Fabrication

This chapter will give fabrication details for the hybrid Si/III-V lasers described in this thesis.

C.1   Fabrication recipes

Many of the recipes are common to the fabrication workflows used to make high-Q hybrid lasers and spacer lasers. These recipes are given here.

C.1.1   Silicon patterning

The modegap grating resonator is patterned by electron-beam lithography and transferred into the silicon chip and spacer oxide by plasma etching. The process is different for high-Q hybrid lasers and spacer lasers because the spacer oxide layer must exist on top of the silicon before etching. The electron-beam resist adheres poorly to oxide, so a layer of chromium is deposited on the oxide to improve resist adhesion and, conveniently, to reduce charging.

Details for electron-beam patterning of high-Q hybrid lasers (i.e., no-spacer lasers) can be found in Christos Santis's thesis [71]. Table C.1 describes the process for patterning the resonator for spacer lasers.

Step	Parameters
Deposit chromium	Deposit 200 Å at 0.5 Å s^{-1} using the CHA Mark 40 electron-beam evaporator
Pattern e-beam resist	Spin ZEP 520A (Zeon Chemicals) at 5000 RPM for 90 s (nominal 350 nm thickness). Bake directly on a hotplate at 180 °C for 10 min. Expose using a Leica/Vistec EBPG 5000+. Grating holes and the waveguide trench close to the sidewall (the "sleeve") are exposed with a dose of 340 µC cm^{-2}, a beam current of 300 pA, and a beam step size of 2.5 nm. The remainder of the pattern (the "bulk") is exposed with a dose of 270 µC cm^{-2}, a beam current of 10 nA, and a beam step size of 10 nm. The resist is developed in ZED-N50 (Zeon Chemicals) for 1 min.
Etch chromium	Transfer the pattern from the ZEP mask to the chromium using chlorine-based plasma in the Oxford PlasmaLab System 100 ICP380. Parameters: Cl$_2$ at 60 sccm, O$_2$ at 3 sccm; chamber pressure 60 mTorr; ICP power 1000 W, RF power 100 W.
Etch oxide and silicon	Strip the resist mask with oxygen plasma to reduce the aspect ratio of the etch. Transfer the pattern from the chromium mask to the oxide/silicon using C$_4$F$_8$-based plasma in the Oxford 380. Parameters: C$_4$F$_8$ at 35 sccm, O$_2$ at 5 sccm; chamber pressure 7 mTorr; ICP power 2100 W, RF power 200 W.
Strip chromium	Submerge the chip in CR-7S chrome etch (Cyantek) for 45 s.

Table C.1: Steps involved in patterning the modegap grating resonator on SOI.

C.1.2   Thermal oxidation

Oxidation is performed in a Tystar Tytan furnace. Chips are cleaned by repeated cycles of piranha ($H_2SO_4(100\%)$:$H_2O_2(30\%)$, 1:3)) and oxygen plasma to strip all organic contaminants from the surface. Spacer chips are oxidized in dry oxygen at $1000\,°C$ for $30\,min$.

C.1.3   Wafer bonding

Direct wafer bonding is used to attach the silicon and III-V chips. All hybrid Si/III-V lasers described in this thesis have at least some oxide on top of the silicon chip, so the bonded interface is always InP to SiO_2. Oxide thicker than several nanometers is amorphous [109–113] though it may retain some small amount of crystalline order [114–117]. It's probably easier to bond InP to an amorphous material because there will be fewer defects introduced by a lattice constant mismatch, but the recipe given here has been used on bare silicon chips (i.e., with no grown oxide), and it seems to work the same.

There are many different techniques for low-temperature direct wafer bonding [118–124]. Many were investigated throughout the course of making these narrow-linewidth hybrid Si/III-V lasers, with varying degrees of success. The recipe given here derives from my earliest recipe that created hybrid Si/III-V chips that reliably survived the subsequent processing steps.

The basic steps used in this recipe are: (1) oxygen plasma surface cleaning and activation, (2) weak van der Waals and hydrogen bonding between the two chips, and (3) annealing the weak bonds into strong covalent bonds. Figure C.1 depicts this process. The initial oxygen plasma treatment of the surface cleans the surface of residual hydrocarbons from previous solvent cleaning steps that would otherwise form bubbles at the future bonded interface [125]. It is also a highly efficient way to terminate both chip surfaces with hydroxyl (-OH) groups. When the chips are brought into contact with some incidental applied contact pressure, weak van der Waals and hydrogen bonds are formed between the polar hydroxyl groups [118; 122].

1. Separate wafers

2. Spontaneous bonding

3. Covalent bonding

4. Bonded wafers
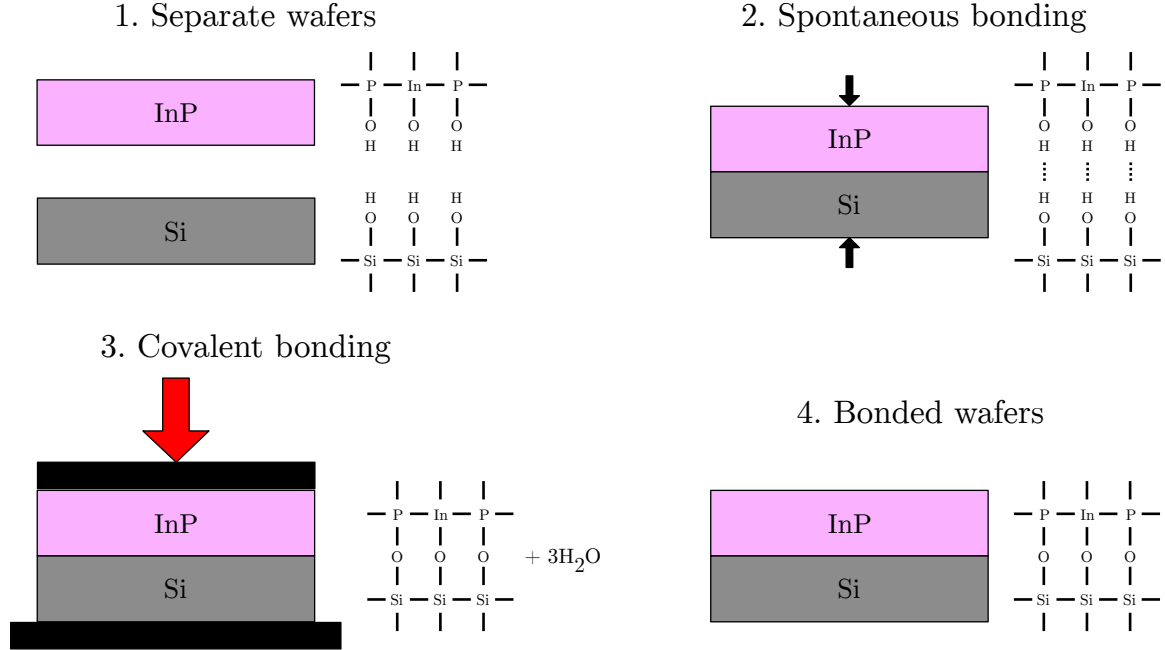
Figure C.1: Cartoon depiction of direct wafer bonding between silicon and InP.

Then, the chips are annealed under higher temperatures and contact pressures to convert the weak bonds to covalent Si-O-III-V bonds. This process produces excess water molecules which must diffuse away from the interface [118]. Therefore, the anneal step may take several hours.

The most important considerations for successful wafer bonding are (in order): (1) the surface roughness and flatness of both chips, (2) the surface chemistry state of each chip, and (3) the anneal process. Practically, I have found that the initial weak bonding step is a critical juncture of the process. I use vacuum tweezers to hold the backside of the III-V chip (face-down) while I bring it into contact with the silicon chip (face-up). After applying light pressure, I try to lift both chips using the vacuum tweezers that are still attached to the backside of the III-V chip only. The weak bonding between the chips should be enough to lift the silicon chip with the III-V chip. If the chips are not weakly attached at this point, no amount of annealing (temperature or contact pressure) will fix it.

Thermal expansion between silicon and InP is very different, so processing temperatures must be kept below $300\,°C$ or so [119; 126]. At these low temperatures,

Step	Parameters
Prior to wafer bonding	Both chips must be perfectly clean. Multiple piranha (H_2SO_4(100%):H_2O_2(30%), 1:3) and oxygen plasma cleans may be required.
Oxygen plasma activation	Oxford ICP 380: 3 min, O_2 flow at 100 sccm, pressure 10 mTorr, RF power 20 W, ICP power 3000 W.
Bonding	Bring the chip faces into contact. Apply light pressure.
Anneal	Suss SB6L: Apply 220 mbar contact pressure to the two chips. Temperature changes in two steps: 150 °C for 1 h followed by 285 °C for 5 h. Ambient air pressure is low-vacuum and is usually less than 1×10^{-4} mbar.
Substrate removal:	Protect edges of the III-V chip by spinning thick PMMA and melting wax along the sides. Scrape the wax from the top of the III-V chip with a razor blade. Remove InP handle in HCl (HCl(38%):H_2O, 3:1). This takes about 1 h.

Table C.2: Steps involved in wafer bonding.

annealing may take many hours or days to fully convert weak bonds to covalent bonds and allow the reaction products to diffuse out of the crystal [122]. We use vertical outgassing channels (VOCs) to create a location for trapped gasses to accumulate, without damaging the interface, from where they may slowly diffuse out of the chip [127]. The VOCs used are squares 5 μm on a side with a center-to-center spacing of 20 μm and are patterned and etched at the same time as the other features.

After annealing, the thick InP handle is removed in hydrochloric acid. The InGaAs p-contact layer serves as an etch stop [128], leaving the epitaxially grown III-V layers attached to the silicon chip and presenting a smooth surface suitable for further fabrication. The sides of the III-V chip are protected with wax during this step in order to prevent the hydrochloric acid from undercutting the etch stop.

Table C.2 details the specific tools used for wafer bonding. Figure C.2 shows the result of a typical chip after wafer bonding.
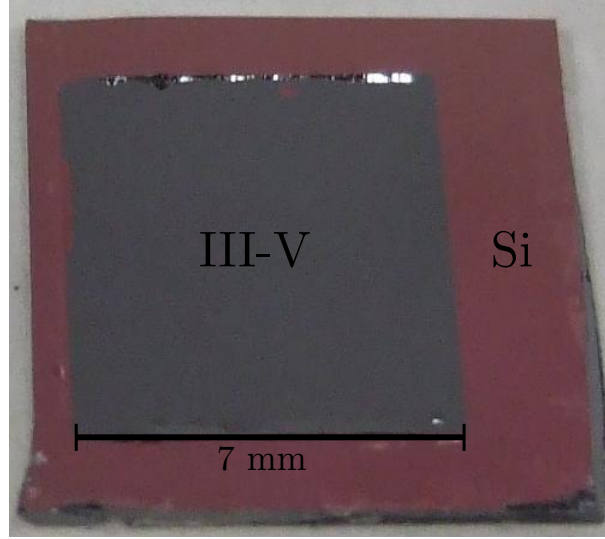
Figure C.2: Typical wafer bonding result.

Step	Parameters
Pattern resist	Spin AZ 5214E (AZ Electronic Materials) at 2000 RPM for 30 s (nominal 2 µm thickness). Bake on a hotplate at 95 °C for 90 s. Expose 9 s on the Suss MA6/BA6 (25 mW cm^{-2} at 405 nm). Mask has an 8 µm dark (non-implanted) region on top of each silicon waveguide. Develop in MF CD-26 (Shipley Microposit) for 30 s. Hard bake directly on a hotplate at 115 °C for 90 s.
Ion implant	Leonard Kroko, Inc.: Hydrogen (H$^+$, proton) at 170 keV, 5×10^{14} cm^{-2}, 7° offset angle.

Table C.3: Steps involved in ion implantation.

C.1.4 Ion implantation

Ion implantation is used to confine electrical current in the III-V to a vertical path above the silicon waveguide. The implant depth must be chosen carefully to allow the current to spread outward to the n-contacts.

Implantation is performed by Leonard Kroko, Inc. (Tustin, CA). The chips are patterned and hard baked before being mailed overnight for the implant. Table C.3 gives the parameters for this process.

After ion implantation, the resist is very gummy and hard to remove. Long solvent
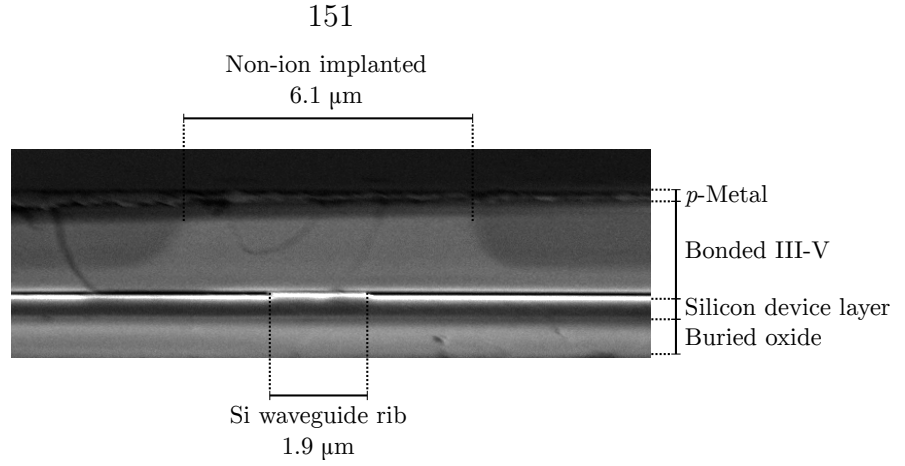
Figure C.3: SEM image of an ion-implated device. The dark region of the III-V has been implanted.

cleans and oxygen plasma are needed to strip the resist.

Figure C.3 shows an SEM image of an ion-implanted device. The image was taken after all processing steps were completed and the bar was cleaved.

C.1.5 Mesa formation

The III-V mesa is formed by wet chemical etching. Three etch steps are needed as acid etches are selective to the various layers in the III-V stack (table C.8). The p-contact layer (p-InGaAs) is removed with piranha, the p-InP cladding is removed in hydrochloric acid, and the undoped InGaAsP quantum wells and strain compensation layers are removed with piranha [128]. Table C.4 shows the steps used to create the mesa.

Freshly mixed piranha will be reactive for about 10 min. It is important to mix new piranha for the final etch step.

C.1.6 Metal contact deposition

Metal contacts are deposited by electron-beam evaporators. The metal stacks are different for the p- and n-side contacts, though lithography is the same. AZ 5214E is image-reversed to make a negative impression of the mask with overhanging sidewalls for easy liftoff. Table C.5 gives the image-reversal photolithography recipe.

Step	Parameters
Pattern resist	Spin AZ 5214E at 2000 RPM for 60 s (nominal 2 μm thickness). Bake directly on a hotplate at 95 °C for 90 s. Expose 9 s on the Suss MA6/BA6 (25 mW cm^{-2} at 405 nm). Mask has a 45 μm protected mesa region on top of each silicon waveguide. Develop in MF CD-26 for 30 s. Hard bake directly on a hotplate at 115 °C for 90 s.
Etch p-InGaAs	Piranha (H$_2$SO$_4$(100%):H$_2$O$_2$(30%):H$_2$O, 5 mL: 15 mL:40 mL), mixed at room temperature, for 7 s.
Pattern resist	Remove previous resist in solvent. Spin AZ 5214 with the same parameters as in the first step. Mask has a 60 μm protected mesa region on top of each silicon waveguide.
Etch p-InP	Hydrochloric acid (38%) at room temperature for 20 s or until bubbles stop forming.
Pattern resist	Strip previous resist in solvent. Spin AZ 5214 with the same parameters. Mask has a 60 μm protected mesa region on top of each silicon waveguide.
Etch InGaAsP	Piranha (same concentration) for 45 s.

Table C.4: Steps involved in wet chemical mesa formation.

Step	Parameters
Spin resist	Spin AZ 5214E at 3000 RPM for 45 s (nominal 1.6 μm thickness). Bake directly on a hotplate at 110 °C for 2 min.
Expose (positive)	Expose 2 s on the Suss MA6/BA6 (25 mW cm^{-2} at 405 nm). Mask has a 30 μm dark (metal) region on top of each silicon waveguide.
Reversal bake	Bake directly on a hotplate at 107 °C for 2 min to crosslink the exposed areas, hardening them against the developer. The temperature of this step is critical.
Expose (all)	Flood expose the entire chip (without a mask) for 16 s (25 mW cm^{-2} at 405 nm) to make the non-crosslinked areas (original mask bright) soluble in developer.
Develop	Develop in MF CD-26 for 30 s.

Table C.5: Steps involved in image-reversal lithography for metal contact deposition.

Metal	Parameters
Ti	Deposit $200\,\text{Å}$ at $1\,\text{Å}\,\text{s}^{-1}$
Pt	Deposit $500\,\text{Å}$ at $1\,\text{Å}\,\text{s}^{-1}$
Au	Deposit $2500\,\text{Å}$ at $2\,\text{Å}\,\text{s}^{-1}$ (only $1500\,\text{Å}$ was deposited on the high-Q hybrid lasers)

Table C.6: Metal p-contact deposition recipe. Titanium contacts the p-InGaAs.

Metal	Parameters
Ge	Deposit $300\,\text{Å}$ at $0.5\,\text{Å}\,\text{s}^{-1}$
Au	Deposit $500\,\text{Å}$ at $1\,\text{Å}\,\text{s}^{-1}$
Ni	Deposit $120\,\text{Å}$ at $1\,\text{Å}\,\text{s}^{-1}$
Au	Deposit $2250\,\text{Å}$ at $2\,\text{Å}\,\text{s}^{-1}$

Table C.7: Metal n-contact deposition recipe. Germanium contacts the n-InP.

The metal contacts themselves are deposited by a CHA Mark 40 or TES Temescal FC-1800 electron-beam evaporation tool. Recipes are found in tables C.6 and C.7.

Contact resistance is surprisingly low even without annealing (see figure 5.13). Annealing is usually required to achieve low contact resistance. Some hybrid SI/III-V devices were annealed in a Jipelec JetFirst-150 rapid thermal annealer at either $325\,°\text{C}$ or $380\,°\text{C}$ for $30\,\text{s}$, but the IV curve did not change after annealing.

C.1.7   Lapping and cleaving

The silicon handle of completed chips is lapped to a final thickness of around $150\,\text{µm}$. Thorough cleaning step at this stage is difficult because any chemicals used must be compatible with all of the various materials on the platform (silicon, III-V, metal, etc.). Lapping is a dirty process, so the chip surface is protected with PMMA to prevent contamination by the alumina slurry used for lapping.

After lapping, chips are scribed with a diamond tool using an machine for alignment. They are cleaved into bars by hand.

C.1.8 Anti-reflection coating

An anti-reflection coating is applied to both facets by mounting the cleaved bars in metal holders. Alumina is deposited on each facet serially using the CHA or TES e-beam evaporator. The thickness is calculated by 3D reflection simulation for each particular geometry. Thicknesses tend to be in the 225 to 250 nm range. In the simulation, the perfect-thickness AR coating would reduce reflections from around 30% to less than 1%, but alumina deposition is difficult and actual thicknesses can be off by 10% or worse.

C.2 Wafers used

C.2.1 SOI wafers

The SOI wafers were provided to us by Prof. John Bowers' research group at the University of California, Santa Barbara. They were originally made by Soitec (Bernin, France).

Prof. Bowers' group oxidized the original wafers, reducing the silicon device layer down to a final thickness of 500 nm. The oxide may be stripped by hydrofluoric acid, leaving a smooth silicon surface compatible with wafer bonding. Conveniently, the existing high-quality thermal oxide on the wafer became the spacer layer in the spacer lasers.

All devices described in this thesis had a buried oxide thickness of 1 μm. The silicon device layer thickness depends on the amount of additional oxide grown on the chips after the pattern is etched. Device layer thicknesses are given in the chapter about each device.

C.2.2 III-V wafers

The III-V wafer is custom grown by Archcom Technology, Inc. (Azusa, CA). Table C.8 shows the design used for the III-V wafers used in this thesis.

Name	Material	Height (nm)	Doping (cm^{-3})	Index
Substrate	InP		n	3.1
Buffer	InP	500	$n = 1 \times 10^{18}$	3.1
p-Contact	In$_{.53}$Ga$_{.47}$As	200	$p > 1 \times 10^{19}$	3.43
Cladding	InP	1500	$p = 1 \times 10^{18}$ $\rightarrow 5 \times 10^{17}$	3.1
SCL	1.15Q InGaAsP	40		3.33
	1.25Q InGaAsP	40		3.3755
QWs ×5 (1% compressive strain)	InGaAsP	7 (per well)		3.53
QW Barriers ×4 (3% tensile strain)	InGaAsP	10 (per barrier)		3.3755
SCL	1.25Q InGaAsP	40		3.3755
	1.15Q InGaAsP	40		3.33
n-Contact	InP	110	$n = 1 \times 10^{18}$	3.1
Superlattice (×2)	In$_{.85}$Ga$_{.15}$As$_{.327}$P$_{.673}$	7.5		3.25
	InP	7.5	$n = 1 \times 10^{18}$	3.1
Bonding Layer	InP	10	$n = 1 \times 10^{18}$	3.1
Silicon	Si			3.471
Buried Oxide	SiO$_2$			1.462

Table C.8: Active III-V wafer design, with the silicon chip included to easily locate the bonded interface. The InP substrate and buffer layers are removed by acid to expose the p-InGaAs surface for processing, noted with a break in the table. The silicon and buried oxide layers are bonded to the InP wafer, and the bonded interface is noted with another break in the table.

Bibliography

[1]   E. Ip et al. "Coherent detection in optical fiber systems." *Optics Express* 16:2, 2008, pp. 753–791. DOI: `10.1364/OE.16.000753`.

[2]   A. Yariv. *Photonics: Optical Electronics in Modern Communications.* 6th ed. New York: Oxford University Press, 2007. ISBN: 0195179463.

[3]   A. Yariv. *Quantum Electronics.* 3rd ed. New York: Wiley, 1989. ISBN: 0471609978.

[4]   L. A. Coldren. *Diode Lasers and Photonic Integrated Circuits.* 2nd ed. Hoboken, N.J: Wiley, 2012. ISBN: 9780470484128.

[5]   E. M. Purcell. "Spontaneous emission probabilities at radio frequencies." *Physical Review* 69, 1946, p. 681. DOI: `10.1103/PhysRev.69.674.2`.

[6]   Y. Arakawa and A. Yariv. "Quantum well lasers – Gain, spectra, dynamics." *IEEE Journal of Quantum Electronics* 22:9, 1986, pp. 1887–1899. DOI: `10.1109/JQE.1986.1073185`.

[7]   S. M. Sze. *Physics of Semiconductor Devices.* 3rd ed. Hoboken, N.J: Wiley-Interscience, 2007. ISBN: 0471143235.

[8]   K. Petermann. *Laser Diode Modulation and Noise.* Dordrecht, The Netherlands: Kluwer, 1988. ISBN: 9027726728.

[9]   A. L. Schawlow and C. H. Townes. "Infrared and optical masers." *Physical Review* 112:6, 1958, pp. 1940–1949. DOI: `10.1103/PhysRev.112.1940`.

[10]   L. Cutler and C. Searle. "Some aspects of the theory and measurement of frequency fluctuations in frequency standards." *Proceedings of the IEEE* 54:2, 1966, pp. 136–154. DOI: `10.1109/PROC.1966.4627`.

[11]   K. Kikuchi and T. Okoshi. "Dependence of semiconductor laser linewidth on measurement time: Evidence of predominance of 1/f noise." *Electronics Letters* 21:22, 1985, pp. 1011–1012. DOI: `10.1049/el:19850717`.

[12]   K. Kikuchi. "Effect of 1/f-type FM noise on semiconductor-laser linewidth residual in high-power limit." *IEEE Journal of Quantum Electronics* 25:4, 1989, pp. 684–688. DOI: `10.1109/3.17331`.

[13]   M. O'Mahony and I. Henning. "Semiconductor laser linewidth broadening due to 1/f carrier noise." *Electronics Letters* 19:23, 1983, pp. 1000–1001. DOI: `10.1049/el:19830679`.

[14] C. Henry. "Theory of the linewidth of semiconductor lasers." *IEEE Journal of Quantum Electronics* 18:2, 1982, pp. 259–264. DOI: `10.1109/JQE.1982.1071522`.

[15] J. Stohs et al. "Gain, refractive index change, and linewidth enhancement factor in broad-area GaAs and InGaAs quantum-well lasers." *IEEE Journal of Quantum Electronics* 37:11, 2001, pp. 1449–1459. DOI: `10.1109/3.958374`.

[16] F. Grillot et al. "Gain compression and above-threshold linewidth enhancement factor in 1.3-µm InAs-GaAs quantum-dot lasers." *IEEE Journal of Quantum Electronics* 44:10, 2008, pp. 946–951. DOI: `10.1109/JQE.2008.2003106`.

[17] C. A. Green, N. K. Dutta, and W. Watson. "Linewidth enhancement factor in InGaAsP/InP multiple quantum well lasers." *Applied Physics Letters* 50:20, 1987, pp. 1409–1410. DOI: `10.1063/1.97836`.

[18] F. Kano et al. "Reduction of linewidth enhancement factor in InGaAsP-InP modulation-doped strained multiple-quantum-well lasers." *IEEE Journal of Quantum Electronics* 29:6, 1993, pp. 1553–1559. DOI: `10.1109/3.234405`.

[19] L. Westbrook and M. Adams. "Explicit approximations for the linewidth-enhancement factor in quantum-well lasers." *Optoelectronics, IEE Proceedings J* 135:3, 1988, pp. 223–225. DOI: `10.1049/ip-j:19880044`.

[20] B. Zhao, T. Chen, and A. Yariv. "A comparison of amplitude-phase coupling and linewidth enhancement in semiconductor quantum-well and bulk lasers." *IEEE Journal of Quantum Electronics* 29:4, 1993, pp. 1027–1030. DOI: `10.1109/3.214485`.

[21] Y. Arakawa and A. Yariv. "Theory of gain, modulation response, and spectral linewidth in AlGaAs quantum well lasers." *IEEE Journal of Quantum Electronics* 21:10, 1985, pp. 1666–1674. DOI: `10.1109/JQE.1985.1072555`.

[22] S. Takano et al. "Sub-MHz spectral linewidth in 1.5 µm separate-confinement-heterostructure (SCH) quantum-well DFB LDs." *Electronics Letters* 25:5, 1989, pp. 356–357. DOI: `10.1049/el:19890247`.

[23] S. Takano et al. "Spectral linewidth reduction in metalorganic vapor phase epitaxy grown 1.5 µm separate-confinement-heterostructure quantum well distributed feedback laser diodes." *Applied Physics Letters* 53:21, 1988, pp. 2019–2020. DOI: `10.1063/1.100307`.

[24] C.-S. Chang et al. "Amplified spontaneous emission spectroscopy in strained quantum-well lasers." *IEEE Journal of Selected Topics in Quantum Electronics* 1:4, 1995, pp. 1100–1107. DOI: `10.1109/2944.488687`.

[25] K. Kikuchi et al. "Measurement of differential gain and linewidth enhancement factor of 1.5-µm strained quantum-well active layers." *IEEE Journal of Quantum Electronics* 30:2, 1994, pp. 571–577. DOI: `10.1109/3.283805`.

[26]   T. Yamanaka et al. "Theoretical study on enhanced differential gain and extremely reduced linewidth enhancement factor in quantum-well lasers." *IEEE Journal of Quantum Electronics* 29:6, 1993, pp. 1609–1616. DOI: `10.1109/3.234412`.

[27]   Y. Arakawa, K. J. Vahala, and A. Yariv. "Quantum noise and dynamics in quantum well and quantum wire lasers." *Applied Physics Letters* 45:9, 1984, pp. 950–952. DOI: `10.1063/1.95453`.

[28]   P. J. A. Thijs et al. "High-performance 1.5 µm wavelength InGaAs-InGaAsP strained quantum well lasers and amplifiers." *IEEE Journal of Quantum Electronics* 27:6, 1991, pp. 1426–1439. DOI: `10.1109/3.89960`.

[29]   T. Ohtoshi and N. Chinone. "Linewidth enhancement factor in strained quantum well lasers." *IEEE Photonics Technology Letters* 1:6, 1989, pp. 117–119. DOI: `10.1109/68.36007`.

[30]   N. K. Dutta et al. "Linewidth enhancement factor in strained quantum well lasers." *Applied Physics Letters* 56:23, 1990, pp. 2293–2294. DOI: `doi:10.1063/1.102944`.

[31]   S. Banerjee, A. K. Srivastava, and N. Chand. "Reduction in linewidth enhancement factor for In0.2Ga0.8As/ GaAs/Al0.5Ga0.5As strained quantum well lasers." *Applied Physics Letters* 58:20, 1991, pp. 2198–2199. DOI: `10.1063/1.104925`.

[32]   M. Osinski and J. Buus. "Linewidth broadening factor in semiconductor lasers – An overview." *IEEE Journal of Quantum Electronics* 23:1, 1987, pp. 9–29. DOI: `10.1109/JQE.1987.1073204`.

[33]   C. Ciminelli et al. "High performance InP ring resonator for new generation monolithically integrated optical gyroscopes." *Optics Express* 21:1, 2013, pp. 556–564. DOI: `10.1364/OE.21.000556`.

[34]   S.-J. Choi et al. "Laterally coupled buried heterostructure high-Q ring resonators." *IEEE Photonics Technology Letters* 16:10, 2004, pp. 2266–2268. DOI: `10.1109/LPT.2004.834518`.

[35]   S.-J. Choi et al. "A high-Q wavelength filter based on buried heterostructure ring resonators integrated with a semiconductor optical amplifier." *IEEE Photonics Technology Letters* 17:10, 2005, pp. 2101–2103. DOI: `10.1109/LPT.2005.856372`.

[36]   J. Piprek, P. Abraham, and J. E. Bowers. "Cavity length effects on internal loss and quantum efficiency of multiquantum-well lasers." *IEEE Journal of Selected Topics in Quantum Electronics* 5:3, 1999, pp. 643–647. DOI: `10.1109/2944.788430`.

[37]   J. W. Leem and J. S. Yu. "Device characteristics and metal–dielectric high reflectivity coating analysis of $\lambda \sim 1.3$ µm InGaAsP/InGaAsP MQW PBH lasers." *Physica Status Solidi A* 207:1, 2010, pp. 217–223. DOI: `10.1002/pssa.200925166`.

[38] M. Jain and C. Ironside. "Internal optical loss measurements in InGaAs-InAlGaAs quantum-well lasers operating around 1550 nm." *IEEE Photonics Technology Letters* 15:5, 2003, pp. 631–633. DOI: 10.1109/LPT.2003.809984.

[39] J. Whiteaway et al. "Logarithmic gain/current-density characteristic of In-GaAs/InGaAlAs/InP multi-quantum-well separate-confinement-heterostructure lasers." *Electronics Letters* 27:4, 1991, pp. 340–342. DOI: 10.1049/el:19910215.

[40] T. Keating et al. "Optical gain measurements based on fundamental properties and comparison with many-body theory." *Journal of Applied Physics* 86:6, 1999, pp. 2945–2952. DOI: 10.1063/1.371153.

[41] S. Sayid et al. "Thermal characteristics of 1.55-μm InGaAlAs quantum well buried heterostructure lasers." *IEEE Journal of Quantum Electronics* 46:5, 2010, pp. 700–705. DOI: 10.1109/JQE.2009.2039117.

[42] M. Rosenzweig et al. "Threshold-current analysis of InGaAs-InGaAsP multi-quantum well separate-confinement lasers." *IEEE Journal of Quantum Electronics* 27:6, 1991, pp. 1804–1811. DOI: 10.1109/3.90008.

[43] J. Plant et al. "1.5-μm InGaAsP-InP slab-coupled optical waveguide lasers." *IEEE Photonics Technology Letters* 17:4, 2005, pp. 735–737. DOI: 10.1109/LPT.2005.843930.

[44] W. T. Tsang. "Extremely low threshold (AlGa)As graded-index waveguide separate-confinement heterostructure lasers grown by molecular beam epitaxy." *Applied Physics Letters* 40:3, 1982, pp. 217–219. DOI: 10.1063/1.93046.

[45] M. Okai et al. "Corrugation-pitch-modulated distributed feedback lasers with ultranarrow spectral linewidth." *Japanese Journal of Applied Physics* 33:Part 1, No. 5A, 1994, pp. 2563–2570. DOI: 10.1143/JJAP.33.2563.

[46] P. W. Juodawlkis et al. "High-power ultralow-noise semiconductor external cavity lasers based on low-confinement optical waveguide gain media." In: *Proceedings of SPIE*. Ed. by A. A. Belyanin and P. M. Smowton. 2010, p. 76160X. DOI: 10.1117/12.846662.

[47] L. Hou et al. "Narrow linewidth laterally coupled 1.55 μm AlGaInAs/InP distributed feedback lasers integrated with a curved tapered semiconductor optical amplifier." *Optics Letters* 37:21, 2012, pp. 4525–4527. DOI: 10.1364/OL.37.004525.

[48] H. Ishii, K. Kasaya, and H. Oohashi. "Narrow spectral linewidth operation ($\ll$ 160 kHz) in widely tunable distributed feedback laser array." *Electronics Letters* 46:10, 2010, pp. 714–715. DOI: 10.1049/el.2010.0802.

[49] M. Faugeron et al. "High-power tunable dilute mode DFB laser with low RIN and narrow linewidth." *IEEE Photonics Technology Letters* 25:1, 2013, pp. 7–10. DOI: 10.1109/LPT.2012.2225419.

[50] T. Asano, B.-S. Song, and S. Noda. "Analysis of the experimental Q factors ($\sim$ 1 million) of photonic crystal nanocavities." *Optics Express* 14:5, 2006, pp. 1996–2002. DOI: `10.1364/OE.14.001996`.

[51] P. Dong et al. "Low loss shallow-ridge silicon waveguides." *Optics Express* 18:14, 2010, pp. 14474–14479. DOI: `10.1364/OE.18.014474`.

[52] M. A. Webster et al. "Low-loss quasi-planar ridge waveguides formed on thin silicon-on-insulator." *Applied Physics Letters* 87:23, 2005, p. 231108. DOI: `10.1063/1.2139836`.

[53] J. Cardenas et al. "Low loss etchless silicon photonic waveguides." *Optics Express* 17:6, 2009, pp. 4752–4757. DOI: `10.1364/OE.17.004752`.

[54] R. Pafchek et al. "Low-loss silicon-on-insulator shallow-ridge TE and TM waveguides formed using thermal oxidation." *Applied Optics* 48:5, 2009, pp. 958–963. DOI: `10.1364/AO.48.000958`.

[55] K. K. Lee et al. "Fabrication of ultralow-loss Si/SiO_2 waveguides by roughness reduction." *Optics Letters* 26:23, 2001, pp. 1888–1890. DOI: `10.1364/OL.26.001888`.

[56] L. K. Rowe et al. "CMOS-compatible optical rib waveguides defined by local oxidation of silicon." *Electronics Letters* 43:7, 2007, pp. 392–393. DOI: `10.1049/el:20073680`.

[57] H. Hagino et al. "Effects of fluctuation in air hole radii and positions on optical characteristics in photonic crystal heterostructure nanocavities." *Physical Review B* 79:8, 2009, p. 085112. DOI: `10.1103/PhysRevB.79.085112`.

[58] H. Sekoguchi et al. "Photonic crystal nanocavity with a Q-factor of $\sim$9 million." *Optics Express* 22:1, 2014, pp. 916–924. DOI: `10.1364/OE.22.000916`.

[59] A. W. Fang et al. "Electrically pumped hybrid AlGaInAs-silicon evanescent laser." *Optics Express* 14:20, 2006, pp. 9203–9210. DOI: `10.1364/OE.14.009203`.

[60] T. Maruyama et al. "GaInAsP/InP membrane BH-DFB lasers directly bonded on SOI substrate." *Optics Express* 14:18, 2006, pp. 8184–8188. DOI: `10.1364/OE.14.008184`.

[61] J. Van Campenhout et al. "Electrically pumped InP-based microdisk lasers integrated with a nanophotonic silicon-on-insulator waveguide circuit." *Optics Express* 15:11, 2007, pp. 6744–6749. DOI: `10.1364/OE.15.006744`.

[62] S. Palit et al. "Low-threshold thin-film III-V lasers bonded to silicon with front and back side defined features." *Optics Letters* 34:18, 2009, pp. 2802–2804. DOI: `10.1364/OL.34.002802`.

[63] X. Sun et al. "Electrically pumped hybrid evanescent Si/InGaAsP lasers." *Optics Letters* 34:9, 2009, pp. 1345–1347. DOI: `10.1364/OL.34.001345`.

[64]   K. Tanabe et al. "Room temperature continuous wave operation of InAs/GaAs quantum dot photonic crystal nanocavity laser on silicon substrate." *Optics Express* 17:9, 2009, pp. 7036–7042. DOI: 10.1364/OE.17.007036.

[65]   A. Yariv. *Optical Electronics in Modern Communications.* 5th ed. New York: Oxford University Press, 1997. ISBN: 0195106261.

[66]   A. Yariv and X. Sun. "Supermode Si/III-V hybrid lasers, optical amplifiers and modulators: A proposal and analysis." *Optics Express* 15:15, 2007, pp. 9147–9151. DOI: 10.1364/OE.15.009147.

[67]   X. Sun and A. Yariv. "Engineering supermode silicon/III-V hybrid waveguides for laser oscillation." *Journal of the Optical Society of America B* 25:6, 2008, pp. 923–926. DOI: 10.1364/JOSAB.25.000923.

[68]   X. Sun, H.-C. Liu, and A. Yariv. "Adiabaticity criterion and the shortest adiabatic mode transformer in a coupled-waveguide system." *Optics letters* 34:3, 2009, pp. 280–282. DOI: 10.1364/OL.34.000280.

[69]   X. Sun et al. "Electrically pumped supermode Si/InGaAsP hybrid lasers." In: *Lasers and Electro-Optics (CLEO) and Quantum Electronics and Laser Science Conference (QELS), 2010 Conference on.* 2010.

[70]   X. Sun. "Supermode Si/III-V lasers and circular Bragg lasers." PhD thesis. California Institute of Technology, 2010.

[71]   C. Santis. "High-coherence hybrid Si/III-V semiconductor lasers." PhD thesis. California Institute of Technology, 2013.

[72]   J. Yeom et al. "Maximum achievable aspect ratio in deep reactive ion etching of silicon due to aspect ratio dependent transport and the microloading effect." *Journal of Vacuum Science & Technology B* 23:6, 2005, pp. 2319–2329. DOI: 10.1116/1.2101678.

[73]   R. A. Gottscho, C. W. Jurgensen, and D. J. Vitkavage. "Microscopic uniformity in plasma etching." *Journal of Vacuum Science & Technology B* 10:5, 1992, pp. 2133–2147. DOI: 10.1116/1.586180.

[74]   J. W. Coburn and H. F. Winters. "Conductance considerations in the reactive ion etching of high aspect ratio features." *Applied Physics Letters* 55:26, 1989, pp. 2730–2732. DOI: 10.1063/1.101937.

[75]   F. N. Hooge. "1/f noise sources." *IEEE Transactions on Electron Devices* 41:11, 1994, pp. 1926–1935. DOI: 10.1109/16.333808.

[76]   K. Takaki et al. "Reduced linewidth re-broadening by suppressing longitudinal spatial hole burning in high-power 1.55-µm continuous-wave distributed-feedback (CW-DFB) laser diodes." *IEEE Journal of Quantum Electronics* 39:9, 2003, pp. 1060–1065. DOI: 10.1109/JQE.2003.816102.

[77]   X. Pan, H. Olesen, and B. Tromborg. "Spectral linewidth of DFB lasers including the effects of spatial holeburning and nonuniform current injection." *IEEE Photonics Technology Letters* 2:5, 1990, pp. 312–315. DOI: 10.1109/68.54690.

[78] B. Tromborg, H. Olesen, and X. Pan. "Theory of linewidth for multielectrode laser diodes with spatially distributed noise sources." *IEEE Journal of Quantum Electronics* 27:2, 1991, pp. 178–192. DOI: `10.1109/3.78219`.

[79] F. Girardin, G.-H. Duan, and P. Gallion. "Linewidth rebroadening due to nonlinear gain and index induced by carrier heating in strained quantum-well lasers." *IEEE Photonics Technology Letters* 8:3, 1996, pp. 334–336. DOI: `10.1109/68.481108`.

[80] R. J. Lang, K. Vahala, and A. Yariv. "The effect of spatially dependent temperature and carrier fluctuations on noise in semiconductor lasers." *IEEE Journal of Quantum Electronics* 21:5, 1985, pp. 443–451. DOI: `10.1109/JQE.1985.1072677`.

[81] J. Zoz and U. Barabas. "Linewidth enhancement in laser diodes caused by temperature fluctuations." *Optoelectronics, IEE Proceedings J* 141:3, 1994, pp. 191–194. DOI: `10.1049/ip-opt:19941084`.

[82] K. Tanabe, K. Watanabe, and Y. Arakawa. "III-V/Si hybrid photonic devices by direct fusion bonding." *Scientific Reports* 2, 2012. DOI: `10.1038/srep00349`.

[83] M.-C. Tien et al. "Silicon ring isolators with bonded nonreciprocal magneto-optic garnets." *Optics Express* 19:12, 2011, pp. 11740–11745. DOI: `10.1364/OE.19.011740`.

[84] S. Ghosh et al. "Ce:YIG/Silicon-on-Insulator waveguide optical isolator realized by adhesive bonding." *Optics Express* 20:2, 2012, pp. 1839–1848. DOI: `10.1364/OE.20.001839`.

[85] Y. Shoji et al. "MZI optical isolator with Si-wire waveguides by surface-activated direct bonding." *Optics Express* 20:16, 2012, pp. 18440–18448. DOI: `10.1364/OE.20.018440`.

[86] Y. S. Lee et al. "Hybrid Si-LiNbO3 microring electro-optically tunable resonators for active photonic devices." *Optics Letters* 36:7, 2011, pp. 1119–1121. DOI: `10.1364/OL.36.001119`.

[87] P. Rabiei et al. "Heterogeneous lithium niobate photonics on silicon substrates." *Optics Express* 21:21, 2013, pp. 25573–25581. DOI: `10.1364/OE.21.025573`.

[88] L. Chen, M. G. Wood, and R. M. Reano. "12.5 pm/V hybrid silicon and lithium niobate optical microring resonator with integrated electrodes." *Optics Express* 21:22, 2013, pp. 27003–27010. DOI: `10.1364/OE.21.027003`.

[89] R. W. P. Drever et al. "Laser phase and frequency stabilization using an optical resonator." *Applied Physics B* 31:2, 1983, pp. 97–105. DOI: `10.1007/BF00702605`.

[90] N. Satyan, W. Liang, and A. Yariv. "Coherence cloning using semiconductor laser optical phase-lock loops." *IEEE Journal of Quantum Electronics* 45:7, 2009, pp. 755–761. DOI: `10.1109/JQE.2009.2013120`.

[91] P. T. Rakich et al. "Giant enhancement of stimulated Brillouin scattering in the subwavelength limit." *Physical Review X* 2:1, 2012. DOI: `10.1103/PhysRevX.2.011008`.

[92] D. Pan et al. "All-optical spectral linewidth reduction of lasers for coherent optical communication." *Optics Letters* 38:24, 2013, pp. 5220–5223. DOI: `10.1364/OL.38.005220`.

[93] J. Li, H. Lee, and K. J. Vahala. "Low-noise Brillouin laser on a chip at 1064 nm." *Optics Letters* 39:2, 2014, pp. 287–290. DOI: `10.1364/OL.39.000287`.

[94] S. Knappe et al. "A chip-scale atomic clock based on ^{87}Rb with improved frequency stability." *Optics Express* 13:4, 2005, pp. 1249–1253. DOI: `10.1364/OPEX.13.001249`.

[95] R. Lutwak. "The Chip-Scale Atomic Clock – Recent developments." In: *Frequency Control Symposium, 2009 Joint with the 22nd European Frequency and Time forum. IEEE International.* 2009, pp. 573–577. DOI: `10.1109/FREQ.2009.5168247`.

[96] C. T. Santis et al. "High-coherence semiconductor lasers based on integral high-Q resonators in hybrid Si/III-V platforms." *Proceedings of the National Academy of Sciences* 111:8, 2014, pp. 2879–2884. DOI: `10.1073/pnas.1400184111`.

[97] J. Chan et al. "Optical and mechanical design of a "zipper" photonic crystal optomechanical cavity." *Optics Express* 17:5, 2009, pp. 3802–3817. DOI: `10.1364/OE.17.003802`.

[98] M. Notomi, E. Kuramochi, and H. Taniyama. "Ultrahigh-Q nanocavity with 1D photonic gap." *Optics Express* 16:15, 2008, pp. 11095–11102. DOI: `10.1364/OE.16.011095`.

[99] E. Kuramochi et al. "Ultrahigh-Q one-dimensional photonic crystal nanocavities with modulated mode-gap barriers on SiO_2 claddings and on air claddings." *Optics Express* 18:15, 2010, pp. 15859–15869. DOI: `10.1364/OE.18.015859`.

[100] B.-H. Ahn et al. "One-dimensional parabolic-beam photonic crystal laser." *Optics Express* 18:6, 2010, pp. 5654–5660. DOI: `10.1364/OE.18.005654`.

[101] Y. Zhang et al. "Photonic crystal nanobeam lasers." *Applied Physics Letters* 97:5, 2010, p. 051104. DOI: `10.1063/1.3475397`.

[102] S. Kim et al. "Nanobeam photonic bandedge lasers." *Optics Express* 19:24, 2011, pp. 24055–24060. DOI: `10.1364/OE.19.024055`.

[103] K. Srinivasan and O. Painter. "Momentum space design of high-Q photonic crystal optical cavities." *Optics Express* 10:15, 2002, pp. 670–684. DOI: `10.1364/OE.10.000670`.

[104] G. Cowle et al. "Spectral broadening due to fibre amplifier phase noise." *Electronics Letters* 26:7, 1990, pp. 424–425. DOI: `10.1049/el:19900276`.

[105] L. Moller. "Novel aspects of spectral broadening due to fiber amplifier phase noise." *IEEE Journal of Quantum Electronics* 34:9, 1998, pp. 1554–1558. DOI: `10.1109/3.709570`.

[106] E. Rochat and R. Dandliker. "New investigations on the effect of fiber amplifier phase noise." *IEEE Journal of Selected Topics in Quantum Electronics* 7:1, 2001, pp. 49–54. DOI: `10.1109/2944.924009`.

[107] G. P. Agrawal and R. Roy. "Effect of injection-current fluctuations on the spectral linewidth of semiconductor lasers." *Physical Review A* 37:7, 1988, pp. 2495–2501. DOI: `10.1103/PhysRevA.37.2495`.

[108] W. H. Burkett, B. Lu, and M. Xiao. "Influence of injection-current noise on the spectral characteristics of semiconductor lasers." *IEEE Journal of Quantum Electronics* 33:11, 1997, pp. 2111–2118. DOI: `10.1109/3.641327`.

[109] E.-C. Cho et al. "Evidence for crystalline silicon oxide growth on thin silicon." In: *2002 Conference on Optoelectronic and Microelectronic Materials and Devices.* 2002, pp. 421–424. DOI: `10.1109/COMMAD.2002.1237280`.

[110] N. Tanaka et al. "First observation of SiO_2/Si(100) interfaces by spherical aberration-corrected high-resolution transmission electron microscopy." *Journal of Electron Microscopy* 52:1, 2003, pp. 69–73. DOI: `10.1093/jmicro/52.1.69`.

[111] N. Ikarashi, K. Watanabe, and Y. Miyamoto. "High-resolution transmission electron microscopy of an atomic structure at a Si(001) oxidation front." *Physical Review B* 62:23, 2000, pp. 15989–15995. DOI: `10.1103/PhysRevB.62.15989`.

[112] K. Kimoto et al. "Metastable ultrathin crystal in thermally grown SiO_2 film on Si substrate." *AIP Advances* 2:4, 2012, p. 042144. DOI: `10.1063/1.4768269`.

[113] A. Ourmazd et al. "Si->SiO_2 transformation: Interfacial structure and mechanism." *Physical Review Letters* 59:2, 1987, pp. 213–216. DOI: `10.1103/PhysRevLett.59.213`.

[114] N. Awaji et al. "In situ observation of epitaxial microcrystals in thermally grown SiO_2 on Si(100)." *Applied Physics Letters* 74:18, 1999, pp. 2669–2671. DOI: `doi:10.1063/1.123953`.

[115] A. Munkholm et al. "Observation of a distributed epitaxial oxide in thermally grown SiO_2 on Si(001)." *Physical Review Letters* 75:23, 1995, pp. 4254–4257. DOI: `10.1103/PhysRevLett.75.4254`.

[116] K. Tatsumura et al. "Residual order within thermally grown amorphous SiO_2 on crystalline silicon." *Physical Review B* 69:8, 2004, p. 085212. DOI: `10.1103/PhysRevB.69.085212`.

[117] I. Takahashi, T. Shimura, and J. Harada. "X-ray diffraction evidence for epitaxial microcrystallinity in thermally oxidized SiO_2 thin films on the Si(001) surface." *Journal of Physics: Condensed Matter* 5:36, 1993, p. 6525. DOI: `10.1088/0953-8984/5/36/007`.

[118] D. Pasquariello and K. Hjort. "Plasma-assisted InP-to-Si low temperature wafer bonding." *IEEE Journal of Selected Topics in Quantum Electronics* 8:1, 2002, pp. 118–131. DOI: `10.1109/2944.991407`.

[119] A. Fang. "Silicon evanescent lasers." PhD thesis. University of California, Santa Barbara, 2008.

[120] Y.-L. Chao et al. "Ammonium hydroxide effect on low-temperature wafer bonding energy enhancement." *Electrochemical and Solid-State Letters* 8:3, 2005, G74. DOI: `10.1149/1.1857671`.

[121] Q.-Y. Tong et al. "Low temperature InP layer transfer." *Electronics Letters* 35:4, 1999, pp. 341–342. DOI: `10.1049/el:19990226`.

[122] X. X. Zhang and J.-P. Raskin. "Low-temperature wafer bonding: A study of void formation and influence on bonding strength." *Journal of Microelectromechanical Systems* 14:2, 2005, pp. 368–382. DOI: `10.1109/JMEMS.2004.839027`.

[123] A. Fontcuberta i Morral et al. "InGaAs/InP double heterostructures on InP/Si templates fabricated by wafer bonding and hydrogen-induced exfoliation." *Applied Physics Letters* 83:26, 2003, p. 5413. DOI: `10.1063/1.1637429`.

[124] Q.-Y. Tong et al. "Low temperature wafer direct bonding." *Journal of Microelectromechanical Systems* 3:1, 1994, pp. 29–35. DOI: `10.1109/84.285720`.

[125] K. Mitani et al. "Causes and prevention of temperature-dependent bubbles in silicon wafer bonding." *Japanese Journal of Applied Physics* 30:Part 1, No. 4, 1991, pp. 615–622. DOI: `10.1143/JJAP.30.615`.

[126] A. W. Fang et al. "Hybrid silicon evanescent devices." *Materials Today* 10:7, 2007, pp. 28–35. DOI: `10.1016/S1369-7021(07)70177-3`.

[127] D. Liang and J. E. Bowers. "Highly efficient vertical outgassing channels for low-temperature InP-to-silicon direct wafer bonding on the silicon-on-insulator substrate." *Journal of Vacuum Science & Technology B: Microelectronics and Nanometer Structures* 26:4, 2008, p. 1560. DOI: `10.1116/1.2943667`.

[128] A. R. Clawson. "Guide to references on III–V semiconductor chemical etching." *Materials Science and Engineering: R: Reports* 31:1, 2001, pp. 1–438. DOI: `10.1016/S0927-796X(00)00027-9`.